Interaction between liquid aluminium and solid iron. Al-rich intermetallics formation

THÈSE N^{O} 6044 (2013)

PRÉSENTÉE LE 19 DÉCEMBRE 2013
À LA FACULTÉ DES SCIENCES ET TECHNIQUES DE L'INGÉNIEUR
CENTRE INTERDISCIPLINAIRE DE MICROSCOPIE ÉLECTRONIQUE
PROGRAMME DOCTORAL EN SCIENCE ET GÉNIE DES MATÉRIAUX

ÉCOLE POLYTECHNIQUE FÉDÉRALE DE LAUSANNE

POUR L'OBTENTION DU GRADE DE DOCTEUR ÈS SCIENCES

PAR

Guillaume PASCHE

acceptée sur proposition du jury:

Dr Ph. Spätig, président du jury
Dr A. Hessler-Wyser, Prof. C. Hébert, directrices de thèse
Prof. D. Balloy, rapporteur
Dr D. Mari, rapporteur
Prof. Ph. Maugis, rapporteur

ÉCOLE POLYTECHNIQUE
FÉDÉRALE DE LAUSANNE

Suisse
2013

À mes petites femmes, Julie & Adèle

Acknowledgements

Funding	Swiss commission for technology and innovation (CTI, project n^{o}: 10215.2)
Supervision	Dr. Aïcha Hessler-Wyser (director), Prof. Cécile Hébert. (co-director), Dr. Robin Schäublin
Jury	Dr. Philippe Spätig (EPFL), Prof. David Balloy (Polytech Lille), Prof. Philippe Maugis (Université Aix-Marseille) and Dr. Daniele Mari (EPFL)
Industry	Allper AG in Düdingen, Switzerland, Atela SA in Neuchâtel, Switzerland Castool Tooling system, Uxbridge, Canada
in particular	Jacques Osowiecki (Atela), André Müller, Daniel Schafer, Natalya Pieri and Gani Murselaj (Allper), Paul Robbins, Mike Rushton and Kitty Tai (Castool)
Special thanks	Prof. Michel Rappaz and Dr. Léa Deillon (LSMX)
CRPP	Frédéric Dolizy, Robert Bertizzolo, Jean-Michel Mayor, Pierre Lavanchy and Pierre-François Isoz
ESRF	Beamline ID15 and especially Dr. Mario Scheel,
***in situ* observation**	Dr. Pierre Burdet, Quentin Jeangros, Dr. Guillaume Lucas (CIME), Dr. Jonas Valloton (LSMX)
Students	Maxime Cattin, Marc Demierre, Arnaud Houriet, Emmanuelle Rol, Gaëtan Villard
ATMX	Pierre-André Despont, Werner Bronnimann, Adrien Grisendi, Yves Ruschetta
Collaborators	The CIME and LSMX staff
in particular	Arthur Brian Aebersold, Grégoire Baroz, Amélie Bazzoni, Dr. Marco Cantoni, Dr. Alexandre Durussel, Annick Evequoz, Dr. Christian Monachon, Emad Oveisi, Dr. Joseph Andreas Schuler, Prof. Pierre Stadelmann, Danièle Laub, Colette Valloton, Dr. Jonas Vannod, Jean-Daniel Wagnière
Personal	Julie & Adèle Burdet, Marinette & Bernard Pasche, Astrid Berglund, Antoine Pasche & mini-them, Annabelle Souriau & Caillou, Keziah Burdet

Lausanne, December 19th, 2013 G. P.

Abstract

Intermetallic phases formation is one of the phenomena, which when coupled to thermal and mechanical strains leads to the premature wear of aluminium die casting tools made out of steel.

This work focuses on two aspects of this wear problem. The first and major part investigates a simplified chemical system Fe(s)–Al(l) at 700 °C in order to study the formation of the intermetallic compounds. The second part focuses on the limitations of the tool wear by testing different coatings on the steel currently used for die casting.

Experiments are performed on two sample types, differentiated by their interface orientation between the two initial phases (vertical and horizontal). Observation are also of two types. *Post mortem* observations are performed by light microscopy and both scanning and transmission electron microscopy. *In situ* observation are performed by X-ray tomography, that allows to follow the evolution of the intermetallic layer with time.

In the Fe(s)–Al(l) system, one main phase, namely Fe_2Al_5 , forms with a particular morphology called *tongue-like* feature in the iron matrix. Tongue tips are generally single crystals. It is also observed that these exhibit a periodical contrast at the nanometre scale. This contrast is found to be due to a slight chemical variation within the existence domain of Fe_2Al_5. This splitting is linked to the spinodal decomposition of the phase observed at higher temperature.

At the interface between tongues and the iron matrix, a layer of about hundred nanometres that surrounds the tongues is observed. It corresponds to the α_2 FeAl phase. Iron matrix, due to the tongue growth, suffers a plastic deformation that is observed by recrystallisation of the direct tongue surrounding. The induced strain field also leads to porosity formation at the interface between the tongues and the matrix. Pores are then trapped in the Fe_2Al_5 phase and partially disappear near from the liquid interface. At this interface, a layer of the order of 10 µm of Fe_4Al_{13} is observed. The thickness of this layer is stable in the explored time range of 0-4 h. However, intermetallic blocks that detach from the layer are observed in the liquid. This is interpreted as mainly due to the dissolution of the formed layer in the bath to achieve its saturation in Fe.

Intermetallic thicknesses and tongue density measurements as functions of time allow to highlight the presence of three main growth regimes. The first at the beginning of the contact corresponds to rapid emergence of the tongues in the matrix. The second is linked to their progressive slow down while they start to thicken. Both thickening and tip growth are in competition from the beginning of this regime. A third regime is however defined and corresponds to a more stable growth during which thickening and tip growth still act in parallel is but their effect is less visible as they vary with the square root of time.

The tongue growth observed at the beginning of the reaction is explained by a growth front destabilisation, similarly to the destabilisation of a planar front that leads to dendritic solidification described by Mullins and Sekerka. A calculation based on their model is proposed and confirms the effect of the law aluminium diffusion in iron but is limited by assumptions made for its development.

Technological investigation proceeds by modification of the studied system and comparison with the fundamental one. Two ferrous materials and one aluminium alloy are studied. In addition, different coatings deposited by electroless plating on one of the ferrous substrates are tested. A quality coefficient is proposed in order to compare the result of the contact between coating and liquid aluminium. One Co-based coating is revealed as the most promising material that allows to limit the wear of the ferrous part by liquid aluminium.

key-words: iron, liquid aluminium, intermetallic phases, 700 °C, SEM, TEM, X-ray tomography, growth, tongue, destabilisation, Mullins-Sekerka, die casting, coating,

Résumé

La formation de phases intermétalliques est l'un des phénomènes qui, couplé à des contraintes thermiques et mécaniques, mène à l'usure précoce de l'outillage en acier de la coulée sous pression d'alliages aluminium.

Ce travail se concentre sur deux aspects de la problématique. Dans un premier temps, la majeure partie de la recherche est effectuée sur un système chimique simplifié Fe(s)–Al(l) à 700 °C pour étudier la formation des phases intermétalliques. Dans un second temps, une recherche technologique se concentre sur la minimisation de l'usure par le test de différents revêtements déposés sur l'acier.

Les expériences sont menées sur deux types d'échantillons, différenciés par l'orientation de l'interface entre les deux phases initiales (verticale et horizontale). Les observations sont également de deux types. Les observations *post mortem* sont effectuées par microscopie optique et par microscopie électronique, à balayage et à transmission. Les observations *in situ* sont effectuées par tomographie de rayons-X qui permettent de suivre l'évolution de l'interface avec le temps.

Dans le système Fe(s)–Al(l), une phase principale, le Fe_2Al_5, se forme avec une morphologie particulière dite en *langue* et croît dans la matrice de fer. Les pointes des langues sont formées généralement d'un unique grain. Il est également observé que ceux-ci présentent un contraste périodique à l'échelle nanométrique révélant une variation chimique locale dans le domaine d'existence de la phase Fe_2Al_5. Cette séparation est également mise en lien avec la décomposition spinodale de la phase à plus haute température.

À l'interface entre les langues et la matrice de Fe, on observe la croissance d'une couche de l'ordre de la centaine de nanomètres de phase FeAl qui correspond à la phase ordonnée α_2. La matrice de Fe, sous l'effet de la croissance des langues, subit une déformation plastique observable par une recristallisation dans l'entourage immédiat des langues. Le champ de contraintes développé par la croissance des langues a également pour effet l'apparition de porosité à l'interface entre les langues et la matrice qui se retrouve par la suite piégée dans la phase Fe_2Al_5 et se résorbe partiellement proche de l'interface avec le liquide. À cette interface, la présence d'une couche de quelques dizaines de microns de Fe_4Al_{13} est observée. L'épaisseur de celle-ci est stable pendant la durée d'observation. Néanmoins, on observe le décrochement de blocs dans le liquide, signe de l'action de la dissolution de la couche formée dans le bain afin de saturer le bain.

La mesure de l'épaisseur d'intermétallique formé, ainsi que celle de la densité de langues en fonction du temps, permettent de mettre en évidence la présence de trois régimes de croissance. Un premier au début du contact correspond à la croissance rapide des langues dans la matrice. Le second correspond à leur ralentissement progressif alors qu'elles commencent à s'épaissir. Les deux effets se trouvent en compétition depuis le début de ce régime. Un troisième régime est défini et correspond à une croissance plus stable pendant laquelle l'épaississement et la croissance des langues se font en parallèle mais leur effet est moins visible.

La croissance sous forme de langues observée en début de réaction est expliquée par la déstabilisation du front de croissance, de manière similaire à la déstabilisation d'un front plan en solidification menant à la solidification dendritique décrite par Mullins et Sekerka. Leur modèle est adapté et appliqué au système étudié et confirme l'effet de la faible diffusion de l'aluminium dans le fer mais est limité par certaines hypothèses.

La recherche technologique procède par modification du système étudié et par comparaison avec le système fondamental. Deux types de matériaux ferreux ainsi qu'un alliage d'aluminium sont étudiés. De plus, différents revêtements déposés par la méthode basée sur le nickelage chimique sont testés. Un coefficient de qualité est mis en place pour pouvoir comparer les résultats avec l'aluminium liquide. Il ressort qu'un revêtement à base de cobalt permet de limiter au mieux l'attaque de l'acier par l'aluminium liquide.

mots-clés : fer, aluminium liquide, phases intermétalliques, 700 °C, SEM, TEM, tomographie de rayons-X, croissance, langues, destabilisation, Mullins-Sekerka, coulée sous pression, revêtements,

Contents

Acknowledgements **v**

Abstract / Résumé **vii**

1 Introduction **1**
1.1 Motivation 1
1.2 Objective 5
1.3 Thesis structure 5

2 Literature review **7**
2.1 Diffusion 8
2.1.1 Generalities 8
2.1.2 Tracer diffusion coefficient 10
2.1.3 Interdiffusion coefficient 11
2.1.4 Intrinsic diffusion coefficient 12
2.1.5 Melt saturation 12
2.2 Intermetallic compound 14
2.2.1 Definition 14
2.2.2 Intermetallics growth 14
2.3 Porosity 18
2.3.1 Kirkendall effect 18
2.3.2 Induced by phase transformation 18
2.4 Front destabilisation 20
2.4.1 Fluid flow 20
2.4.2 Dendritic growth 21
2.5 Aluminium-Iron system 25
2.5.1 Thermodynamic data 25
2.5.2 Crystallographic data 28
2.5.3 Published experiments 30
2.5.4 Morphology 30
2.5.5 Kinetics 33
2.5.6 Diffusion coefficients 35
2.5.7 Intermetallics dissolution 38

3 Investigation methods **39**
3.1 Materials . . . 40
3.1.1 Materials used for fundamental investigations . . . 40
3.1.2 Materials used for technological investigations . . . 40
3.2 Sample testing . . . 41
3.2.1 Liquid Metal Immersion Facility . . . 41
3.2.2 Sample with vertical interface (dipping test) . . . 42
3.2.3 Samples with horizontal interface . . . 43
3.3 *Post mortem* observations . . . 44
3.3.1 Sample preparation . . . 44
3.3.2 Light Microscopy . . . 45
3.3.3 Scanning Electron Microscopy . . . 45
3.3.4 Transmission Electron Microscopy . . . 47
3.4 *In situ* observations with X ray tomography . . . 48
3.4.1 X-ray tomography . . . 48
3.4.2 Data acquisition . . . 49
3.4.3 Samples . . . 49
3.5 Quantification . . . 50
3.5.1 Image treatment . . . 50
3.5.2 Equivalent thickness . . . 51
3.5.3 Area fraction . . . 51
3.5.4 Tongue thickening . . . 52
3.5.5 Saturation . . . 53
3.5.6 Quality coefficient . . . 54
3.6 Numerical modelling . . . 55
3.6.1 Hypothesis . . . 55
3.6.2 Thermodynamic parameters . . . 56
3.6.3 Discretisation . . . 56
3.6.4 Conditions . . . 58
3.6.5 Flux and interface velocity . . . 58
3.6.6 Densities . . . 60

4 Intermetallic compounds **61**
4.1 Main intermetallic phase Fe_2Al_5 . . . 62
4.1.1 Phase morphology . . . 62
4.1.2 Phase structure . . . 64
4.2 Interface with solid Fe . . . 68
4.2.1 Transition layer . . . 68
4.2.2 $FeAl_2$ phase . . . 70
4.2.3 Iron matrix deformation . . . 72
4.2.4 Porosity formation . . . 74
4.3 Interface with liquid Al . . . 76

4.3.1 Fe_4Al_{13} phase . . . 76
4.3.2 Dissolution . . . 77
4.4 Summary . . . 79

5 Intermetallics evolution 81
5.1 Beginning of reaction . . . 83
5.2 Intermetallic thickness evolution . . . 84
5.3 Measurement variation according to test configuration . . . 85
5.3.1 Bath saturation . . . 85
5.3.2 Cylindrical geometry . . . 89
5.4 Growth regimes . . . 91
5.5 Tongue thickening . . . 94
5.6 Interface position . . . 98
5.7 Summary . . . 99

6 Interface destabilisation 101
6.1 System description . . . 102
6.2 Steady state regime . . . 102
6.2.1 Concentration profile in Fe . . . 102
6.2.2 Solute balance at the interface . . . 103
6.3 Destabilisation . . . 105
6.3.1 Concentration profile in Fe . . . 105
6.3.2 Curvature calculation . . . 106
6.3.3 Parameter a . . . 107
6.3.4 Stability criterion . . . 107
6.4 Criterion application . . . 108
6.5 Summary . . . 112

7 Technological Results 115
7.1 Species addition in Fe – Al system . . . 116
7.1.1 Melt composition . . . 116
7.1.2 Alloying elements . . . 116
7.1.3 Microstructure . . . 116
7.2 SEM observations . . . 117
7.2.1 Ferrous alloys . . . 117
7.2.2 Aluminium alloy . . . 118
7.2.3 Protective coatings . . . 119
7.3 Quantification . . . 121

8 Conclusions 125
8.1 Synthesis . . . 125
8.1.1 Fundametal investigation . . . 125
8.1.2 Technological investigation . . . 129

8.2 Perspectives 129

Bibliography **131**

Symbols **139**

Appendix **143**

Curriculum Vitae **145**

1 Introduction

1.1 Motivation

Aluminium alloys are very attractive for automotive industry as they allow reducing the weight of cars and thus their consumption, a requisite imposed by the European Union. Low density and high tensile strength are required properties for such applications. However, the high cost of aluminium relative to steel and the difficulty to manufacture it in modern large-scale production hindered its development and made it quite rare as car constituent until twenty years ago [1]. Thanks to technological progresses and under the pressure of new ecological directives, automotive manufactures started progressively to replace steel parts by aluminium. In 2000, the firsts cars with a full aluminium body such as the Audi A2 started to be produced routinely [1]. Nowadays, this trend is increasing. Small pieces like door handles or large ones like engine motors of more than 35 kg can be produced in aluminium alloys by die casting. Fig. 1.1 presents schematically a die casting device with the main steps of the production cycle.

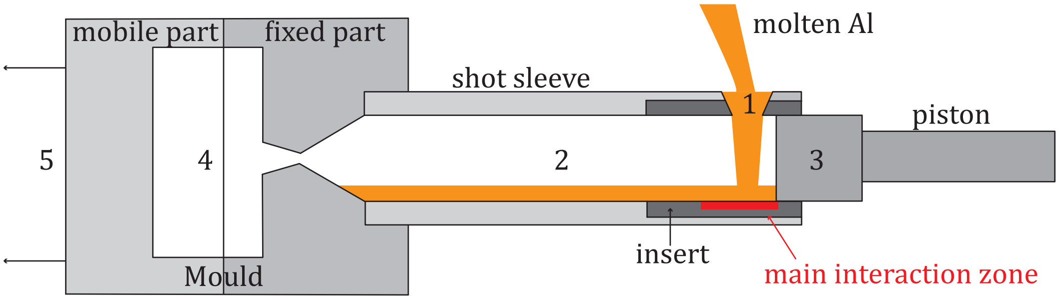

Figure 1.1: Die casting device with production steps: (1) Molten aluminium is poured in the shot sleeve (2). After a stabilisation time, it is injected by the piston (3) into the mould (4) where solidification occurs. Once cooled down, the mobile part of the mould is removed (5) and the product is extracted.

One production cycle consists in the following steps:

0. A lubricant is sprayed in the injection cylinder, also *called shot sleeve*.
1. A determined portion of molten aluminium is poured in the shot sleeve.
2. Stabilisation of the melt lasts between few seconds to 1 min, depending on the size of the device.
3. The melt is then injected into the mould by means of the piston.
4. Pressure is maintained until solidification occurs.
5. The mould is open and the piece is removed.
6. The piston is retracted and the cycle starts again.

One cycle lasts approximately 90 s, depending on the size of the facility. At industrial pace, hundreds of pieces are produced per day. Thus the shot sleeve inner wall undergoes a high temperature, slightly above the melting point of the aluminium alloy, and mechanical stress through the flow of liquid metal and friction with the piston during the injection. This occurs particularly in the main interaction zone marked in Fig. 1.1, just below the pour hole.

Shot sleeves reveal after few thousand cycles an important wear with dimples several millimetres deep, especially underneath the pour area. Fig. 1.2 (a) presents the shot sleeve viewed

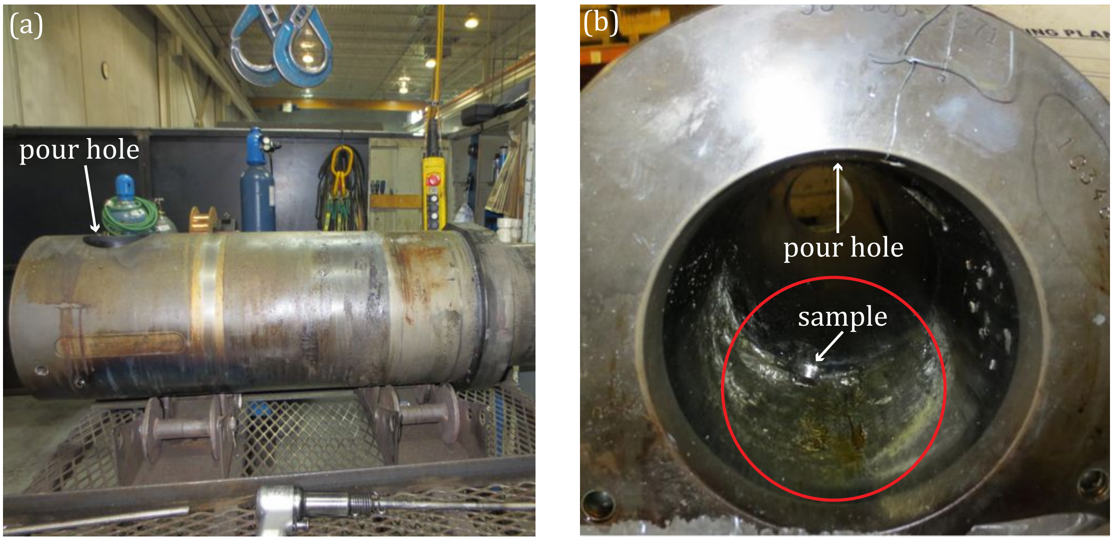

Figure 1.2: Shot sleeve after use: (a) side view of the cylinder. (b) Inside of the cylinder with the pouring zone in front, exhibiting irregularities due to the wear suffered during the use. Pictures from Castool

from the side. It is 500 mm in diameter and about 1500 mm in length. The inside of the shot sleeve with the main interaction zone in red circle is presented in Fig. 1.2 (b).

One can observe that the inner surface of this shot sleeve is irregular with holes in the steel and with some remaining material sticking to the inner wall. This wear causes different problems, especially during injection. Indeed, the piston movement can be disturbed or even seized up. Aluminium leak can also happen. Thus, the shot sleeve must be changed frequently, which involves stopping of the production for about one week. In order to limit this production down time, some solutions were found, such as the positioning of a consumable insert underneath the pour hole (Fig. 1.1). This allows substantial cost reduction as only part of the cylinder is changed. This insert is generally made out of the same material than the shot sleeve. Nevertheless, the insert does not solve the wear problem. Lubrication of the tool and preheating of the shot sleeve partially limits the wear but the problem generally persists.

If one extracts a sample from the shot sleeve presented in Fig. 1.2 in the region underneath the pour zone marked by the arrow and observes it with a scanning electron microscopy (section 3.3.3), the microstructure looks like the one presented in Fig. 1.3 (a) and (b). Micrography (a) shows that some aluminium on the left of the image in darker grey remains at the surface of the shot sleeve, which is on the right of this image. One also remarks lines at the surface with about 45° from bottom left to right up image corners that correspond to the passage of the piston during injection. This shows that aluminium was present at least during the last injection and that it is stuck to the steel surface. At higher magnification as in Fig. 1.3 (b), one can remark that an intermediate layer is present at the limit between the aluminium

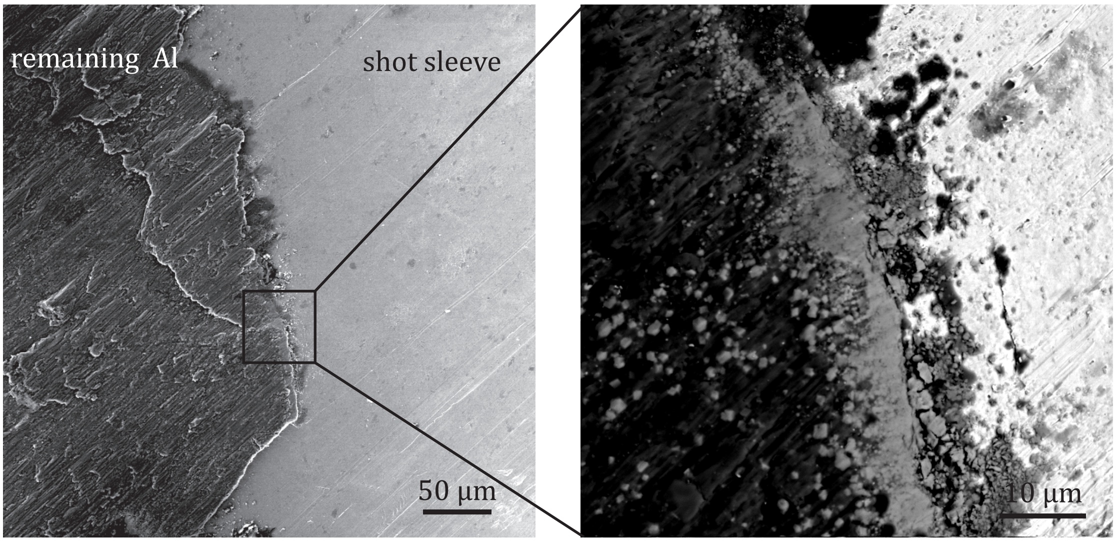

(a)
(b)

Figure 1.3: Inner wall of the shot sleeve after use, viewed from top: SEM micrography (a) SE contrast of a region with remaining Al. (b) BSE contrast at higher magnification of the limit between Al and the shot sleeve.

and the steel. It can be shown by chemical analysis (X-ray EDS section 3.3.3) that this layer corresponds to an Al-rich Al-Fe compound. The Fe-Al phase diagram presented in section 2.5.1 shows that such Al-rich compounds have a rather fixed stoichiometry. They are called *intermetallics* (section 2.2).

Thus, during operation, aluminium coming from the melt and iron of the shot sleeve interact, leading to the formation of intermetallic phases. Intermetallic compounds are usually more brittle than alloys. One remarks in Fig. 1.3 (b) the presence of small intermetallic particles in the solidified aluminium. Thus, when the piston passes intermetallics breaks. This point is part of the mechanism that is assumed to be responsible for the shot sleeve degradation. It is schematically represented in Fig. 1.4 with two other phenomena, which, when coupled, lead to the premature degradation of the shot sleeve.

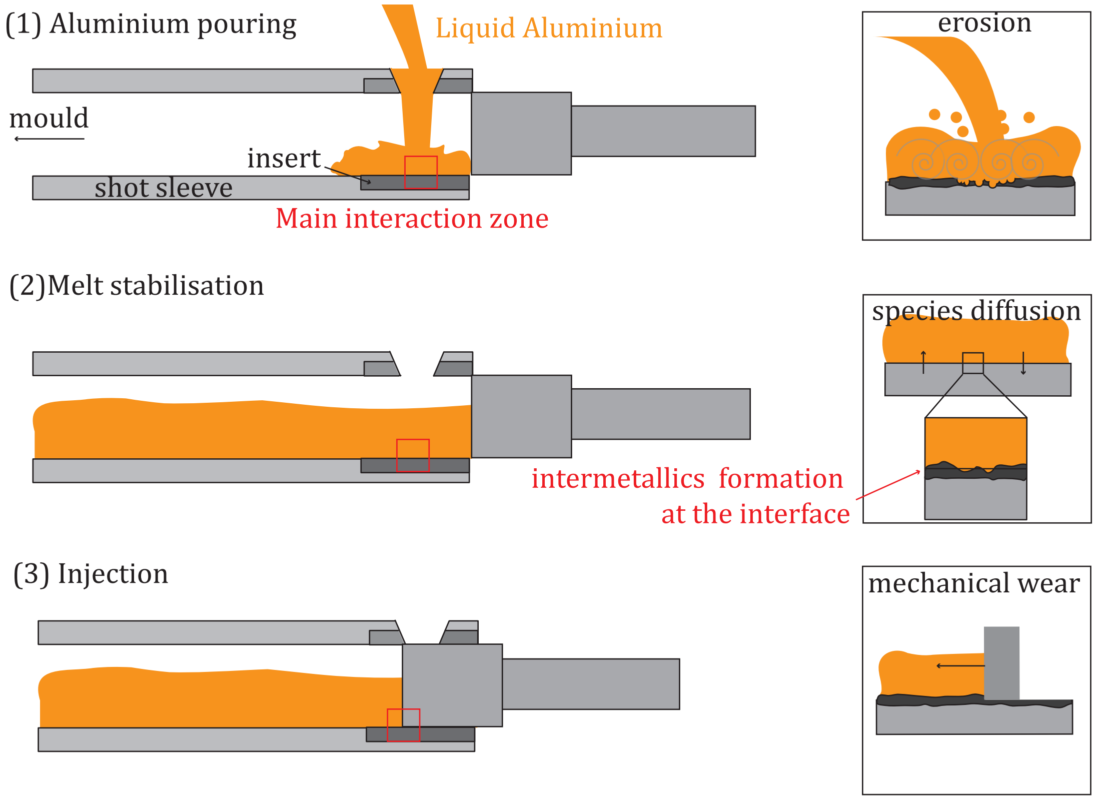
(1) Aluminium pouring
Liquid Aluminium
mould
insert
shot sleeve
Main interaction zone
erosion
(2)Melt stabilisation
species diffusion
intermetallics formation at the interface
(3) Injection
mechanical wear

Figure 1.4: Shot sleeve wear: Phenomena occurring during die casting cycle, which coupled lead to the precocious degradation of the shot sleeve: (1) Erosion during the pouring, (2) diffusion during the stabilisation, (3) mechanical wear during the injection.

After Al pouring (1), the melt stabilises (2), a step during which species diffusion occurs, with aluminium penetrating the steel and iron dissolving in the melt. This leads to the formation of a brittle intermetallic layer at the interface. This interaction can be assimilated to a diffusion couple (section 2.1). Intermetallic compounds are then partially removed by passage of the piston during the injection (3). When the next production cycle starts, the shot sleeve surface exhibits irregularities. Some erosion can also occur during the pouring and thus interacts with the worn surface. Irregularities are progressively amplified during service and after a certain time, the shot sleeve surface is totally worn out as seen in Fig. 1.2.

Limiting this wear implies thus impeding these three phenomena. Erosion is already minimized by adding a special funnel that slows down the aluminium on the shot sleeve surface but the mechanical wear due to the piston cannot be avoided. It appears that limiting the formation of intermetallic compounds is the key for shot sleeve wear limitation and lifetime extension. Understanding the mechanisms that lead to the formation of these phases is thus of great interest.

1.2 Objective

The present work has two distinct objectives. On the one hand, assuming that Al-rich intermetallics formation is the central phenomenon that leads to the shot sleeve wear, a fundamental investigation focuses on the description and modelling of their formation. In this aim, the system is simplified to a binary Fe – Al interaction at a constant temperature of 700 °C. The interface resulting from this interaction is investigated, in terms of microstructure and of growth kinetics. Particular attention is paid on the irregular *tongue–like* shape of the main intermetallic compound Fe_2Al_5. Fundamental investigation represents the major part of the present study.

On the other hand, a technological solution to reduce shot sleeve's wear is investigated by means of laboratory testing of coatings in partnership with Allper AG, Düdingen, a die casting facility producer and Atela SA, Neuchâtel, a chemical nickel plating company.

1.3 Thesis structure

The present document is divided into eight chapters. State-of-the-art and theoretical concepts necessary to the understanding of the intermetallics formation are presented in chapter 2. More precisely a general description of diffusive system is first exposed (2.1). Then, particular cases in diffusion process as intermetallics formation (2.2), porosity formation (2.3) and front destabilisation (2.4) are presented. The binary Fe – Al system is also presented in this chapter in terms of thermodynamic, crystallographic, morphology and kinetics properties (2.5).

Chapter 3 presents the investigation methods used for the present research. The different materials are described (3.1) together with the experimental facilities (3.2) and the observation methods (3.3 and 3.4). Image treatment techniques (3.5) and numerical model description (3.6) complete this chapter.

Chapter 4 focuses on the microstructure description of the reacted interface. Thus, three different regions are distinguished: the intermetallic layer (4.1), its interface with the iron matrix (4.2) and the one with liquid aluminium (4.3).

Chapter 5 presents the system's time-evolution, including the intermetallic layer thickness measurement (5.2). It allows among others highlighting measurement variations implied by sample production methods (5.3). Then, growth regimes are described (5.4) and compared with the thickening of the structure (5.5), showing the impact of the tongues on the layer's kinetics.

Chapter 6 presents a mathematical model inspired by the Mullins-Sekerka theory of dendritic growth (section 2.4) and tries to explain the mechanisms behind the tongue formation described in the previous chapters. A simplified one-dimensional system of an intermetallic phase growing in between two initial phases is first studied in a steady state regime (6.2). Then one interface is destabilised in a second direction and the system is again analysed, allowing to define a stability criteria.

Chapter 7 presents the technological investigation. A brief review of the effect of alloying elements in the Fe – Al system is given in section 7.1. SEM observations of the different systems are presented in section 7.2. These systems correspond to the fundamental system with the modification of:

- the ferrous substrate, with pure iron that is replaced by a ferritic steel or a cast iron.
- the melt, with pure aluminium that is replaced by an Al-Si alloy.
- the initial ferrous surface, upon which a coating is deposited.

Section 7.3 presents the results of the wear by the mean of a quality coefficient proposed in section 3.5.6.

Finally, chapter 8 brings together the different informations obtained along the previous chapters, presents the intermetallics growth as a succession of growth regimes with their own particularities (8.1.1) and proposes different ways to go further in the understanding of the system.

2 Literature review

This chapter presents theoretical elements allowing to understand the mechanisms involved in the formation and growth of intermetallic compounds. Section 2.1 is dedicated to the basic mathematical description of diffusive systems and defines among other things the different diffusion coefficients. Then section 2.2 focuses on intermetallic compounds. Their definition and published studies on their growth are presented. The two next sections go further in presenting phenomena that occur during the growth, such as porosity apparition (2.3) and front destabilisation (2.4). Finally, section 2.5 focuses on the Fe-Al system, presenting its thermodynamic, crystallography, morphology and kinetics properties.

2.1 Diffusion

2.1.1 Generalities

As mentioned by Porter and Easterling [2], one of the most fundamental processes controlling the rate of phase transformation, which occurs to decrease Gibbs free energy, is the diffusion of atom species. The two common mechanisms by which atoms can diffuse through a crystalline solid are respectively the interstitial and the substitutional one, depending on the type of sites occupied by the solute in the lattice of the solvent. When the size of the solvent and the solute atoms are similar, which is the case with iron and aluminium with respectively 126 and 143 pm [3], solute atoms occupy substitutional sites. The mechanism of substitutional diffusion involves vacancy diffusion, as described in the following. A perfect solid solution of two different elements A and B, whose free energy curve is presented in Fig. 2.1, is considered. Let's put together two blocks of this alloy with respective atomic fraction X_1 and X_2 ($X_1 < X_2$).

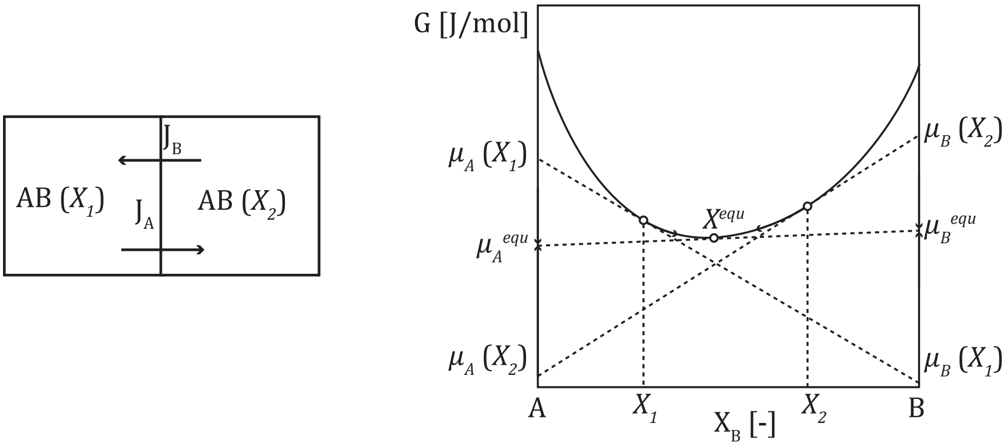

(a) (b)

Figure 2.1: (a) Schema of two blocks of an AB alloy with respective atomic fraction X_1 and X_2 and species flux directions. (b) Free energy curve of this perfect solution with respective chemical potential.

The equilibrium composition X^{equ} is given by the minimum of the free energy curve. To achieve this minimum, the two blocks will tend to change their composition by means of atomic diffusion. The way the free energy will evolve with regards to B for example is evaluated by the *chemical potential*, which is defined as the variation of the Gibbs free energy G when a small amount of B, ∂n_B, is added to the phase at constant temperature T, pressure p, and number of atoms in A n_A.

$$\mu_B = \left(\frac{\partial G}{\partial n_B}\right)_{T,p,n_A} \quad [\mathrm{J \cdot mol^{-1}}] \quad (T, p, n_A \text{ constant}) \tag{2.1}$$

To reach equilibrium, the chemical potential as a function of n_B will decrease from $\mu_B(X_2)$ to

μ_B^{equ}. The flux of atoms B, J_B at the interface is proportional to its gradient in the phase. It is presented for a one dimensional system in Equ. 2.2.

$$J_B = -M_B c_B \frac{\partial \mu_B}{\partial x} \qquad [\mathrm{mol} \cdot \mathrm{m}^{-2} \cdot \mathrm{s}^{-1}] \tag{2.2}$$

with M_B the atomic mobility in mol · s· kg^{-1} and c$_B$ the volume concentration of B in mol·m^{-3}. However, in presence of a chemical gradient, it is more common to express the flux as function of this gradient, considering that atoms are diffusing in the direction of the decreasing gradient. Fick's first law then estimates the flux:

$$J_B = -D_B \frac{\partial c_B}{\partial x} \qquad [\mathrm{mol} \cdot \mathrm{m}^{-2} \cdot \mathrm{s}^{-1}] \tag{2.3}$$

D_B is the *diffusion coefficient* or diffusivity of element B in m^2·s^{-1}. Fick's law fixes its definition as the proportionality factor between the species flux and the chemical gradient. Furthermore, in a non-steady state, the species balance gives:

$$\frac{\partial J_B}{\partial x} = -\frac{\partial c_B}{\partial t} \tag{2.4}$$

Combining Equs. 2.3 and 2.4 and supposing D_B independent of the concentration and constant, one obtains the second Fick's law, predicting the evolution of the concentration profile with time:

$$\frac{\partial c_B}{\partial t} = D_B \frac{\partial^2 c_B}{\partial x^2} \tag{2.5}$$

The relation between the atomic mobility (Equ. 2.2) and the diffusion coefficient (Equ. 2.3) is given by:

$$D_B = M_B RT \left(1 + \frac{\mathrm{d} ln \gamma_B}{\mathrm{d} ln X_B}\right) \tag{2.6}$$

with R the gas constant, X_B the atomic fraction of element B and γ_B the activity coefficient, defined as:

$$\gamma_B = \frac{a_B}{X_B} \quad [-] \tag{2.7}$$

a_B being the activity of element B, which is equivalent to the concentration for real solutions. For regular solutions, the activity is linked to the enthalpy of mixing Ω:

$$\ln\left(\frac{a_B}{X_B}\right) = \frac{\Omega}{RT}(1 - X_B)^2 \tag{2.8}$$

Thus, the diffusion coefficient can be expressed as a function of the mixing enthalpy ΔH_{mix}:

$$\begin{aligned} D_B =& M_B RT \left(1 + \frac{\Omega}{RT} \frac{\mathrm{d}(1-X_B)^2}{\mathrm{d}lnX_B}\right) \\ =& M_B RT \left(1 + \frac{\Omega}{RT} X_A X_B\right) \\ =& M_B RT \left(1 + \frac{2\Delta H_{\mathrm{mix}}}{RT}\right) \end{aligned} \tag{2.9}$$

As diffusion is a thermally activated process, the diffusion coefficient D_B can also be expressed as an Arrhenius law:

$$D_B(T) = D_{B,0} \exp\left(-\frac{Q_B}{RT}\right) \tag{2.10}$$

with $D_{B,0}$ the pre exponential factor in $\mathrm{m}^2 \cdot \mathrm{s}^{-1}$ and Q_B in the activation energy $\mathrm{J} \cdot \mathrm{mol}^{-1}$ for the diffusion of element B.

As already mentioned, the substitutional diffusion mechanism involves vacancies. In addition, crystallographic defects in the solvent such as grain boundaries and dislocations will favour diffusion, especially at temperatures lower than its melting point, generally between 0.75 to 0.8 T_m. Below this limit, diffusion will therefore preferentially occur along those defects [4]. Thus, a smaller grain size or a high density of dislocations promotes diffusion and thus the diffusion coefficient is not only dependent on the temperature but also on the microstructure. Additionally to the mesoscopic scale dependence, the atomic structure also influences the diffusion coefficient. Diffusion in a direction whose atomic occupancy is different from 1 can be higher than in others. The vacancy concentration being higher, probability of movement along this direction is increased. This particular case occurs in one intermetallic phase of the Fe - Al system, as described in section 2.5.2.

In the case of substitutional diffusion, two main measurement methods are available, giving each a diffusion coefficient of different nature as explained in the following.

2.1.2 Tracer diffusion coefficient

Diffusion in homogeneous systems are described by Fick's first law (Equ. 2.3). This is the case for tracer diffusion, requiring small amounts of solute species and thus conserving a homogeneous global concentration. The diffusion of the tracer species relative to the solvent lattice is characterized by the *tracer diffusion coefficient* D^* [3]. Tracers are of different types. Radioactive, stable isotopes or elements with properties close to the one of the diffusive element, e.g. In or Zn for aluminium [5] or Re for iron [3] are used. Another way to determine D^* is to simulate the behaviour of the material at the atomic scale with e.g. density-functional theory calculations (DFT) [6]. One follows the atoms position in time to deduce the diffusion coefficient with the Einstein equation:

$$D^* = \frac{R^2(t+\Delta t) - R^2(t)}{6\Delta t} \tag{2.11}$$

where $R(t)$ corresponds to the mean atomic movement and is defined as:

$$R^2(t) = \frac{1}{N}\sum_{i=1}^{N}(r_i(t) - r_i(t_0))^2 \tag{2.12}$$

with r_i the position of atom i, N the number of atoms and t_0 initial time.

2.1.3 Interdiffusion coefficient

Measurement of diffusion in a chemical gradient, such as the interdiffusion of two adjacent metal blocks, cannot be described directly as for tracer diffusion, as two diffusion coefficients are required, one for each species. However, these are equal as concentration's gradient and species flux are equal and opposite. Fick's first law describes the diffusion process with a single D that refers to the diffusion rate of either species relative to a fixed referential. It is called the *interdiffusion coefficient* $\tilde{D}$ [3].

$$J_A = -\tilde{D}\frac{\partial c_A}{\partial x} \qquad \text{and} \qquad J_B = -\tilde{D}\frac{\partial c_B}{\partial x} \tag{2.13}$$

$\tilde{D}$ can be expressed as follow [7]:

$$\tilde{D} = \frac{X_A X_B(v_A - v_B)}{\partial X_B/\partial x} \quad = \quad \frac{V_m(X_B J_A - X_A J_B)}{\partial X_B/\partial x} \tag{2.14}$$

taking into account the mean velocities v_i of species i, and the molar volume V_m assumed to be constant. Wagner *et al.* [8] developed the concept by defining an integrated interdiffusion coefficient for the phase v in a diffusion couple:

$$\tilde{D}^{v}_{int} = \int_{X_i}^{X_j} \tilde{D}^{v}\mathrm{d}X \tag{2.15}$$

where X_i and X_j are the atomic fraction that define the existence domain of the phase v. In the particular case of the growth of one intermetallic compound (defined in section 2.2) with a narrow existence domain between two pure elements, Equ. 2.15 can be simplified and integrated, giving an interdiffusion coefficient from the measured coefficient K [9]

$$\tilde{D} = \frac{1}{2}X_A X_B K^2 \tag{2.16}$$

with X_A the atomic fraction of A and X_B the one of B ($X_B = 1 - X_A$). K is defined as the parabolic growth constant of a purely diffusive system. It corresponds to the proportionality coefficient between the thickness W of a formed intermetallics at time t and the square root of time:

$$W = K\sqrt{t} \qquad [\mathrm{m}] \tag{2.17}$$

Equ. 2.16 implies that the interdiffusion coefficient is constant in the existence domain and that this domain is narrow with regard to the composition. Equ. 2.17 implies that the growth of the intermetallic layer is fully described by diffusion. Thus, other processes taking place at the interface, namely wetting, nucleation of the phase and chemical reaction between the metals, are assumed to take only a negligible portion of the interaction time [10].

2.1.4 Intrinsic diffusion coefficient

To provide a more complete description of binary substitutional diffusion, such as the rates of diffusion of the two species relative to the local lattice planes, *intrinsic* or *partial diffusion coefficients* D_A and D_B can be introduced [3]:

$$\tilde{D} = X_A D_B + X_B D_A \tag{2.18}$$

Except at very low concentrations of B, D_B and D_B^* differ fundamentally because the presence of the chemical concentration gradient under which D_B is measured imposes a bias on the otherwise random motion of atoms, which makes atoms jump preferentially in one direction along the gradient. The relation between these two coefficients is given by [3]:

$$D_B = D_B^* \left(1 + \frac{\partial \ln \gamma_B}{\partial \ln X_B}\right) \tag{2.19}$$

and in the particular case of a concentration tending to zero, the bracket term is the same for both species:

$$\frac{D_A}{D_A^*} = \frac{D_B}{D_B^*} \tag{2.20}$$

2.1.5 Melt saturation

Principle

The presence of a liquid phase in the system implies species dissolution to saturate the melt. Saturation principle can be understood by solute balance at the interface between two phases. Fig. 2.2 (a) presents a partial phase diagram of a theoretical AB system. For the development, two phases are considered. The α phase initially only composed of A species and a phase at composition c_0 that is liquid at temperature T. Putting into contact these two phases, the chemical profile across the interface at the beginning is given in Fig 2.2 (b). Interface concentrations are given by the solidus and the liquidus at c_1 and c_2 for the solid and the liquid side respectively. Far from the interface, concentrations are the initial ones. Solute balance at

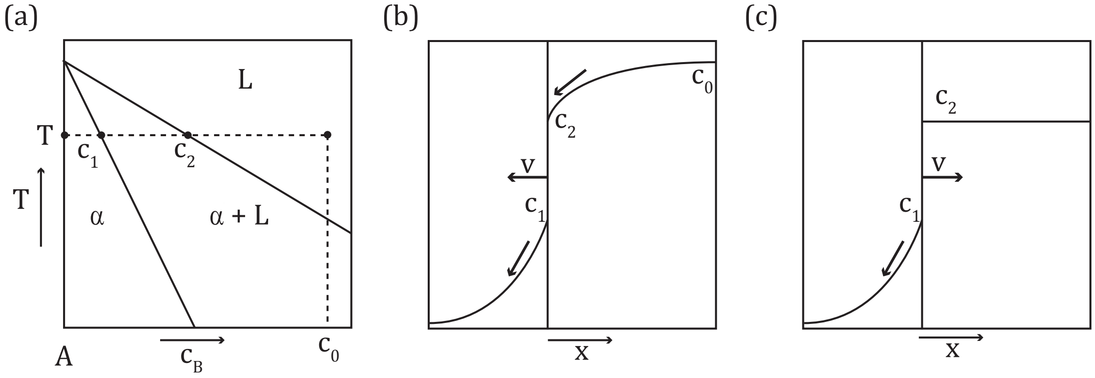

Figure 2.2: Theoretical system AB: (a) A-rich part of the phase diagram (b) Chemical profile at the beginning of the contact. (c) Chemical profile after melt saturation.

the interface is given by:

$$v(c_2 - c_1) = J_2 - J_1 = -D_l \frac{\partial c}{\partial n} + D_s \frac{\partial c}{\partial n} \tag{2.21}$$

with J_1 and J_2 the fluxes at the interface on each side respectively, D_l and D_s diffusion coefficients in the liquid and the solid respectively and n the normal to the surface. The second equality is given by Fick's first law (Equ. 2.3). As c_2 is larger than c_1, the equality implies that interface velocity is negative and thus the interface moves to the left in Fig. 2.2 (b). The liquid is then progressively enriched with species A until the whole melt is at c_2 as presented in Fig. 2.2 (c). At this moment, no gradient subsists in the liquid and J_2 becomes null. The solute balance at the interface (Equ. 2.21) shows that v becomes positive and the interface moves to the right.

Natural convection

The previous description of the melt saturation only considers diffusive phenomenon without taking into account the position of the interface. Nonetheless, the latter can modify the concentration profile in the liquid and thus the saturation rate. Fig. 2.3 presents schematics of two configurations of solid – liquid interaction with A species heavier than B one. The two configurations only differ by the orientation of their interface, horizontal in (a) and vertical in (b). As species A is heavier than species B, the horizontal situation is stable, with the density gradient collinear to the gravity. In the case of a vertical interface, the density gradient induces natural convection as it is perpendicular to the gravity. As it will be seen in section 5.3, natural convection is especially acting for one of the four test configurations for which the melt volume is large enough to never saturate during the experiment. Note that the effect of saturation and thus of the natural convection is not fully described in the present work.

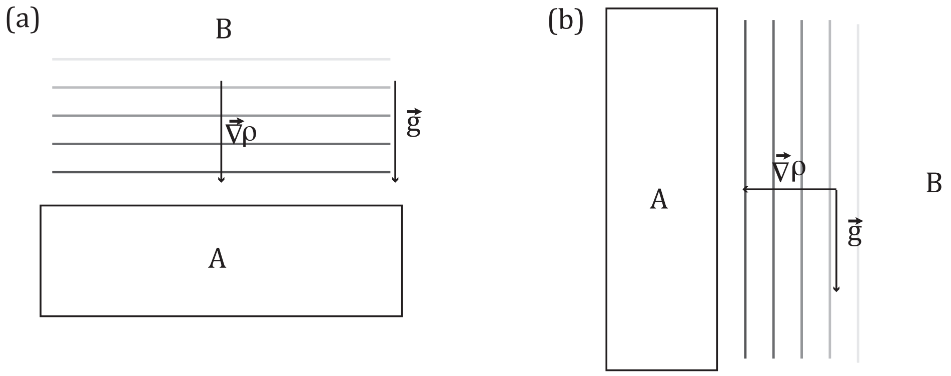

Figure 2.3: Schematics of the concentration profile in a liquid bath when dissolution of a species A heavier than the solvent B occurs. (a) On a horizontal interface the situation is stable. (b) On a vertical interface, the difference between the two species implies a density gradient $\vec{\nabla}\rho$ perpendicular to the gravity $\vec{g}$, leading to the apparition of natural convection.

2.2 Intermetallic compound

2.2.1 Definition

Definitions found for an *intermetallic compound* or an *intermetallics* are multiple. Table 2.1 presents few definitions coming from dictionaries and specialized web sites.

These definitions give indications on the nature of an intermetallic compound, with the difference between an intermetallics and an alloy. One proposal comes from the atomic structure difference. Intermetallic compounds have a crystallographic structure that is different from the structure of the pure elements at their base while alloys are based on the initial structure of one of the elements, adapting its geometry with the increase in solvent content to minimize energy. Thus, in alloys solute atoms are usually randomly replacing solvent atoms on atomic sites. This difference also explains the thin existence domain in terms of concentration for intermetallics. Indeed even a small modification will not be compensated by atoms of the other species since atomic sites are not exchangeable.

2.2.2 Intermetallics growth

From the different definitions of 2.1, intermetallic compound can be obtained by *diffusion couple experiments*. Let's put into contact two semi-infinite samples of pure elements A, phase α and B, phase β, respectively and let's consider the theoretical case presented in Fig. 2.4. Fig. 2.4(a) presents a partial binary phase diagram AB with two initial phases α and β and an intermetallic phase η in between with a stoichiometric composition c_η. Solubility limits of B in α and A in β at temperature T are denoted respectively by c_α^* and c_β^*. If the diffusion couple AB is annealed at temperature T for an appropriate time t, the phase η will form a layer along

Table 2.1: Intermetallic compound (or Intermetallics) definition found in universal dictionaries and technical journals.

Larousse (translation)	Adj. In alloys, compound with strong metallic character, which at ordered state is stable in a well defined concentration area.
Collins	Adj. (chemistry) (of a chemical compound) formed from two or more metallic elements.
Intermetallics Journal (Elsevier)	Ordered chemical compounds between two or more metals
Merriam-Webster (Encyclopaedia Britannica)	Composed of two or more metals or of a metal and a non-metal especially : being an alloy having a characteristic crystal structure and usually a definite composition.
dictionary.com (US web dictionary)	Any of a class of substances composed of definite proportions of two or more elemental metals, rather than continuously variable proportions (as in solid solutions). The crystal structures and the properties of intermetallic compounds often differ markedly from those of their constituents. In addition to the normal valences of their components, the relative sizes of the atoms and the ratio of the total number of valence electrons to the total number of atoms have important effects on the composition of intermetallic compounds.
usinenouvelle.com (french magazine) (translation)	Alloy of well determined and very precise composition, resulting from rapid cooling of a mixing of two metals or one metal and one metalloid or from diffusion of atoms in an atomic crystalline structure of different kind.

the interface between $\alpha-\beta$ phases [11]. A schematic of the concentration and the chemical potential profiles after this time t is presented in Fig. 2.4(b) respectively with dashed and continuous lines. The chemical potential profile is deduced from the tangents common to the free energy curves of each phase that gives values at the different interfaces. Concentrations at the interfaces are extracted from the binary phase diagram in Fig. 2.4. Looking closer at the interface between α and η, if a unitary surface ($S = 1$) of this interface moves by dx to the left, the volume of α with concentration c_α^*, which is converted into η at concentration c_η, is equal to $1 \cdot \mathrm{d}x$. Then, the number of atoms B present in this volume is given by:

$$(c_\eta - c_\alpha^*)\mathrm{d}x \qquad [-] \tag{2.22}$$

In the other hand, flux of B atoms arriving at the interface is given by Equ. 2.2, which allows to write:

$$J_B^{in} = -M_B^\eta c_B^\eta \frac{\partial \mu_B}{\partial x} \qquad [\mathrm{m}^2 \cdot \mathrm{s}^{-1}] \tag{2.23}$$

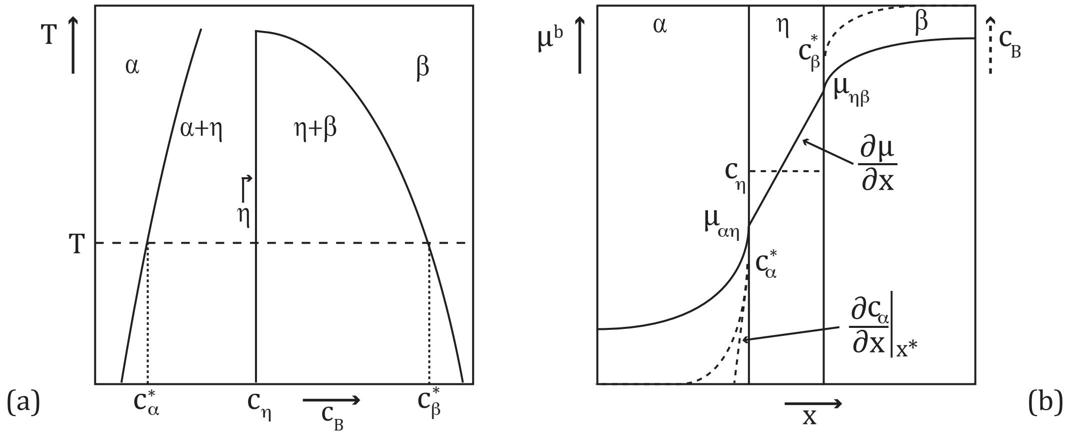

Figure 2.4: (a) Theoretical phase diagram of elements A and B with two primary phases α and β and an intermetallic phase η. (b) Concentration (dashed) and chemical potential (continuous) profiles through the system at time t of contact of the two initial semi infinite samples.

and flux of B atoms leaving the interface in the direction of α is defined by Equ. 2.3:

$$J_B^{out} = -D_B^{\alpha} \left.\frac{\partial c_B^{\alpha}}{dx}\right|_{\text{interface}} \qquad [\mathrm{m}^2 \cdot \mathrm{s}^{-1}] \tag{2.24}$$

During a period $\mathrm{d}t$, the quantity of B atoms in the interface is then:

$$(J_B^{in} - J_B^{out})dt \qquad [-] \tag{2.25}$$

Combining this result with 2.22, one obtains that the interface velocity $v_{\alpha\eta}$ is equal to the difference of the flux divided by the concentration step at the interface.

$$v_{\alpha\eta} = \frac{dx_{\alpha\eta}}{dt} = \frac{(J_B^{in} - J_B^{out})}{c_\eta - c_\alpha^*} \qquad [\mathrm{m} \cdot s^{-1}] \tag{2.26}$$

Equ. 2.26 describes the movement of an interface for a purely diffusive system [12]. In a multiple phases system, such a balance can be done at each interface to get its position with time. It is the basis allowing to mathematically model the growth of the phases as a function of material properties and experiment parameters.

Kajihara *et al.* [12] proposed a mathematical model based on Equ. 2.26 for a model considering one intermetallics in between two initially pure elements. In contrast to the previous development, the defined intermetallic is not stoichiometric and thus presents an existence domain. It then implies that J_B^{in} in Equ. 2.23 is expressed as a function of the interdiffusion coefficient instead of the atomic mobility. They showed the relationship between the parabolic growth constant K presented in Equ. 2.17 and the nine parameters of the system, namely the four concentrations at the interfaces, the two concentrations in the initial phases far from the interfaces and the three interdiffusion coefficients. They concluded that the interdiffusion coefficient and the solubility limits are the main parameters of the intermetallic growth. Thus, for the intermetallic compound with a narrow solubility range and a small interdiffusion coefficient, experiments require a long time to reach an observable thickness and obtain workable data.

Svoboda *et al.* proposed a numerical model for binary [13] and ternary [14] systems with several intermetallics forming at the interfaces. The general formulation of the model can be described as follow. Let's assume a multi-component system with k components (here k=A,B) forming n stable stoichiometric phases with fixed mole fraction of A element X^{ν} ($\nu = 1,...,n$) with respective molar Gibbs free energy g^{ν} and molar volume V_m^{ν}. It is assumed that during a negligible time interval nuclei of all phases are formed at the interface and that they grow into a sequence of layers. It is also assumed that every new-formed phase has neither vacancies nor sink sources. Then the total free energy of the system is given by

$$\Delta G = \sum_{\nu=1}^{n} \frac{g^{\nu}}{V_m^{\nu}} \Delta x_{\nu} \tag{2.27}$$

The velocity of the interface between two adjacent phases is then determined. Let u_{ν} be the interface velocity between phase ν and $\nu+1$ relative to the lattice of phase ν and v_{ν} the velocity of the same interface relative to the phase $\nu+1$. The mass conservation given in Equ. 2.26 allows to determine those velocities. For two components A and B, it gives:

$$u_{\nu} = \frac{V_m^{\nu}}{X^{\nu} - X^{\nu+1}} \left((J_A^{\nu} - J_A^{\nu+1})(1 - X^{\nu+1}) - (J_B^{\nu} - J_B^{\nu+1}) X^{\nu+1} \right) \tag{2.28}$$

and

$$v_{\nu} = \frac{V^{\nu+1}}{X^{\nu} - X^{\nu+1}} \left((J_A^{\nu} - J_A^{\nu+1})(1 - X^{\nu}) - (J_B^{\nu} - J_B^{\nu+1}) X^{\nu} \right) \tag{2.29}$$

The boundary conditions for a binary system are the following

$$J_A^1 = 0, \qquad J_B^1 = 0, \qquad J_A^n = 0, \qquad J_B^n = 0, \qquad v_1 = 0 \quad \text{and} \qquad u_n = 0 \tag{2.30}$$

The variation of free energy with time is given by the derivative of Equ. 2.27, which gives:

$$\dot{G} = \sum_{\nu=1}^{n} \frac{g^{\nu}}{V_m^{\nu}} (u_{\nu} - v_{\nu}) \tag{2.31}$$

For species flux determination, the authors based their development on thermodynamic considerations and on Onsager's work [15] concerning the maximum energy dissipation rate in a diffusive process. A set of linear equations for species fluxes is obtained and put in a matrix form, which can be solved as it is diagonal.

$$J_A^{\nu} = F_A^{\nu} \frac{X^{\nu} D_A^{\nu}}{RT V_m^{\nu} \Delta x^{\nu}} \qquad \text{and} \qquad J_B^{\nu} = F_B^{\nu} \frac{(1 - X^{\nu}) D_B^{\nu}}{RT V_m^{\nu} \Delta x^{\nu}} \tag{2.32}$$

With D_A^ν and D_B^ν the diffusion coefficient of species A and B, respectively, in the phase ν. F_A^ν and F_B^ν are the driving forces for diffusion and can be obtained by the derivative of the free energy variation with respect to the fluxes:

$$-F_A^\nu = \frac{\partial \dot{G}}{\partial J_A^\nu} \qquad \text{and} \qquad -F_B^\nu = \frac{\partial \dot{G}}{\partial J_B^\nu} \tag{2.33}$$

The model can then predict the time evolution of the interfaces position. Léa Deillon [16], studying Au-In and In-Ni systems, developed a one-dimension numerical model with finite differences based on this mathematical development. In the present work, the model was applied to the Fe-Al system to simulate the formation of one ($\nu = 1$) intermetallic compound at the interface between solid iron and liquid aluminium.

2.3 Porosity

During growth, porosity can appear in the formed phases or at the interface with the initial phases. This section presents two phenomena that can act in its formation.

2.3.1 Kirkendall effect

Consider the theoretical system presented in Fig. 2.1. Let's assume that diffusion is controlled by substitutional mechanism and that the diffusion rate of A is larger than the one of B ($|\vec{J_A}| > |\vec{J_B}|$). A diffusional couple is created by welding the two blocks, with inert markers placed at the weld junction. As the diffusion fluxes are different, there will be a net flow of matter through the inert markers. The whole specimen thus translates as illustrated in Fig. 2.5 [2]. In order to compensate this net matter flow, there will be a vacancies flow J_V in the opposite direction, given by:

$$\vec{J_A} = -\vec{J_B} - \vec{J_V} \tag{2.34}$$

The vacancies condense then to form pores. Recent work of Fan *et al.* [17] working on the formation of Al coating on hot stamped steel showed that porosity formation occurs in such system after heat treatment, as presented in Fig. 2.6. A characteristic porosity line is appearing here in the intermediate phase. They however did not observe such formation in as coated samples (Fig. 2.6 (a)).

2.3.2 Induced by phase transformation

A well known phase transformation inducing stress is the martensitic transformation. Martensite, due to the increase of carbon in solute solution is slightly less dense than the initial austenite. In an hypothetical case without any thermal induced stress, if a region undergoes the transformation, increasing its volume, as austenite is much more ductile, a neighbour-

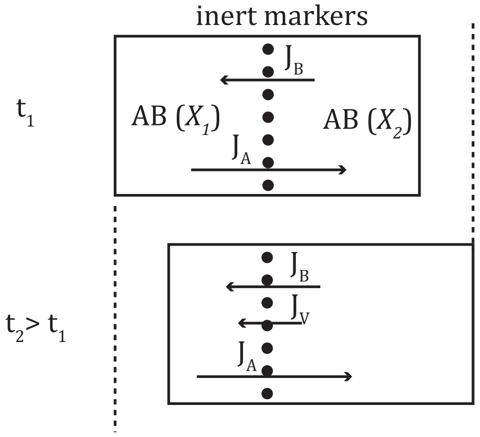

Figure 2.5: Representation of the Kirkendall effect. Schematics of a diffusion couple with respective B atomic fractions X_1 and X_2 ($X_1 > X_2$). Inert markers were deposited at the initial interface. After a certain time, due to species flux difference, one observes a specimen translation. To compensate matter flow, a vacancy flux J_V is created in the opposite direction.

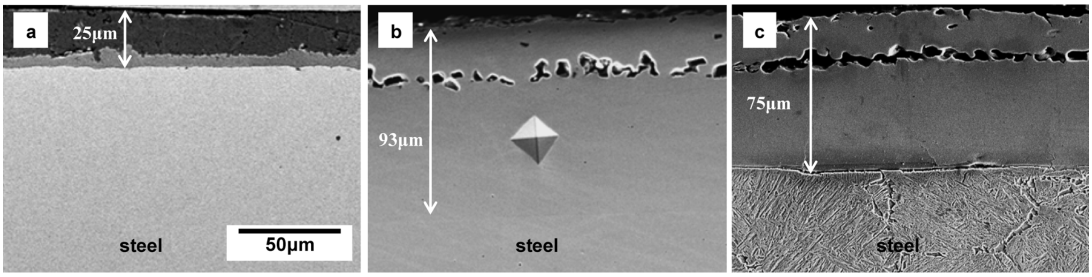

Figure 2.6: from [17]:FE-SEM micrographies of the cross section of the 22MnB5 steel coated with thick Al–10wt%Si coating (a) as hot dipped, (b) heat treated at 1050°C for 30min and (c) heat treated at 1050°C for 30min and 30% strained at 700 °C.

ing region that has not transformed yet will deform to compensate the shift induced by the transformation. In the particular case of the Fe-Al system, intermetallics growth could also imply mechanical stress in iron due to differences in the physical properties of the different phases. Gedevanishvili *et al.* [18] worked on sintering of Fe and Al powders and showed that the formation of the Fe_2Al_5 intermetallic phase produces an important swelling of the particles and a large amount of porosity. The latter decreases with an increasing amount of Si in Al. Furthermore, Kang *et al.* [19] working on the Fe_3Al powder fabrication from Fe_2Al_5 showed that the latter produced from pure Fe and pure Al powders exhibits a brittle and porous sponge-like microstructure (Fig. 2.7). They thus associated this porous structure to the swelling demonstrated by Gedevanishvili *et al.* [18]. Although those informations were obtained with powder sintering experiments, whose conditions differ from the one of the present study, the Fe_2Al_5 formation implies an important swelling of the system and can be

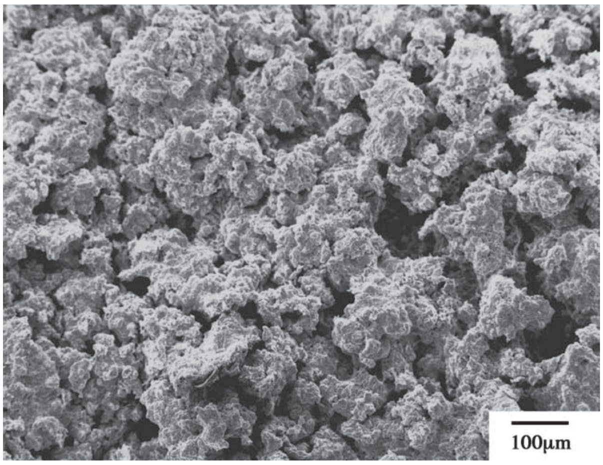

Figure 2.7: from [19]: The 650 °C for 1 h sintered Fe–71.5 Al compact displays a porous and sponge-like microstructure.

considered as the cause of the stress induced at the interface. Furthermore, as for martensitic transformation, the intermetallic formation consists in the growth of a hard phase, here the Fe_2Al_5 phase, in a much more ductile one, here iron and thus, iron deforms. As grain interfaces are regions with lower mechanical resistance than bulk materials, larger deformation should be observed there, that can lead to porosity formation localised along the interface.

2.4 Front destabilisation

Intermetallics may not grow homogeneously and then interfaces are no more flat but present instabilities. Although front destabilisation is well known in fluid flow or during solidification process, this phenomenon is unusual in the case of growth in solid phase as it is the case for Fe – Al system. No information can be found in the literature. This section presents basic theories for both fluid flow and dendritic solidification that will be used as tools to model the intermetallic growth destabilisation.

2.4.1 Fluid flow

In the 50's Saffman and Taylor [20] studied the development of instabilities of the interface between two immiscible fluids in a porous media. It can be approached in two dimensions by a Hele-Shaw cell that consists in two glass plates separated by a thin gap in regards of the two other dimensions. Injecting the less viscous fluid, which displaces the more viscous one, so-called *Saffman-Taylor instabilities* or *viscous fingering* appears at the interface. This kind of pattern is also denominated *tongue-like structure*. Fig. 2.8 presents one result of Maes [21] working on the the viscous fingering of to miscible fluids. The characterisation of the stability can be approached for fluids by two dimensionless parameters: Θ the logarithmic ratio of the

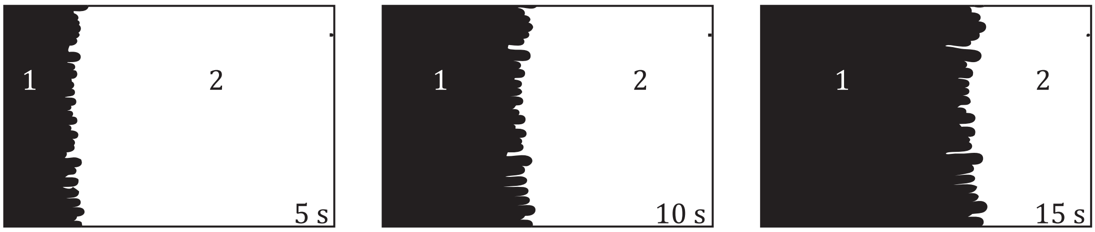

Figure 2.8: Finger instabilities appearing during an experiment in Hele-Shaw cell: Interface evolution between tinted water (1, black) and a solution containing 70% of glycerol (2, white). Logarithmic ratio of viscosities $\Theta = 1.35$. The observed area is 10 cm in width, 14 cm in length and the thickness between the two horizontal glass plates is 0.25 mm. Injection speed is $5\,\mathrm{mm}\cdot\mathrm{s}^{-1}$ [21].

dynamic viscosities ξ and *Pe* the *Peclet* number given in Equ. 2.35. ξ letter is used here for viscosities instead of the usual μ, which represents chemical potential. Peclet number *Pe* is the ratio between convection and diffusion phenomena in the system. In the case of miscible system, it is defined as follow:

$$\Theta = ln\left(\frac{\xi_1}{\xi_2}\right) \qquad \text{and} \qquad Pe = \frac{Rv}{2D} \tag{2.35}$$

with ξ_1 the viscosity of the injected fluid, ξ_2 the one of the moved fluid, R a characteristic dimension of the system, here the gap between the two glass plates, v the mean speed of the flux and D the diffusion coefficient in fluid 2. Finger instability appears as soon as $\Theta > 0$ and the system is more unstable as this ratio increases. Let's consider now a metallic system with one of the phase in solid state. The viscosity of a crystal structure has no physical meaning. *Pe* however can be considered and is a good indicator of the interface stability. In the present case of miscible media, fingering will be compensated by species diffusion, which acts as a stabiliser. Thus the higher the *Pe*, the more unstable the interface is [21].

2.4.2 Dendritic growth

A binary metal with the phase diagram presented in Fig. 2.9, solidifies at an initial concentration c_0 in the form of a paraboloid dendrite with a tip of radius R and growing at velocity v. The liquid composition c_l^* at the interface with the tip is given by the liquidus line of the phase diagram. Isoconcentration lines are represented by dashed lines going from c_l^* to c_0 in Fig. 2.9 [22].

The flux balance at the interface can be expressed as:

$$vc_l^*(1-k) \approx D_l \frac{c_l^* - c_0}{R/2} \tag{2.36}$$

With k the partition coefficient and D_l the diffusion coefficient in the liquid. Rearranging

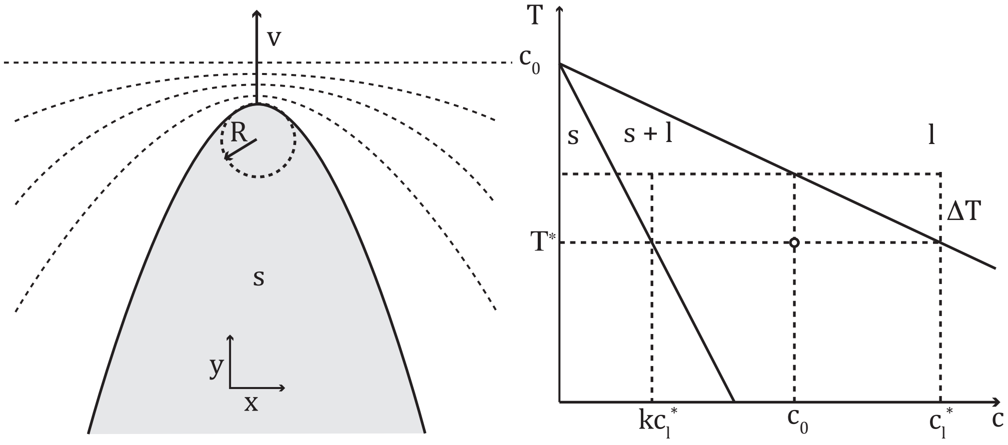

Figure 2.9: (a) Schematics of a dendrite growing with initial composition c_0. (b) Theoretical phase diagram of the alloy solidifying.

terms, one can extract the supersaturation term Ω and the dimensionless Peclet number *Pe*.

$$\underbrace{\frac{c_l^* - c_0}{c_l^*(1-k)}}_{\Omega} = \underbrace{\frac{Rv}{2D_l}}_{Pe} \tag{2.37}$$

Invantsov in 1936 made the exact solution of the flux balance taking into account the parametric description of the paraboloid. It was shown that this solution is well described by a fit of type:

$$\Omega = 1.5Pe^{0.8} \tag{2.38}$$

Then, fixing the temperature, the two remaining parameters are the tip radius R and the tip velocity v, implying that the slimmer the tip the faster its growth and inversely. However, the "extremum criterion", which considers that the tip grows at the maximum velocity for a given undercooling with account of the curvature undercooling, is not verified by experiments, as presented in Fig. 2.10. Indeed, the experimental data are situated in the rectangle on the graphic Log R – log v always showing a shift with respect to the maximum of the curve that should be the growth regime. Langer and Mueller-Krumbhaar proposed then that the dendrite is growing with a larger tip radius, given by the *marginal stability limit*, described in Equ. 2.39 and also represented in Fig. 2.10 by the $R^2 v$ =cst line.

$$R = \lambda_i \approx 2\pi\sqrt{\frac{\Gamma_{sl}}{mG_c - G}} \tag{2.39}$$

With Γ_{sl} de Gibbs-Thomson coefficient of the solid-liquid interface, m the liquidus slope, G_c the chemical gradient in the liquid and G the thermal gradient in the liquid.

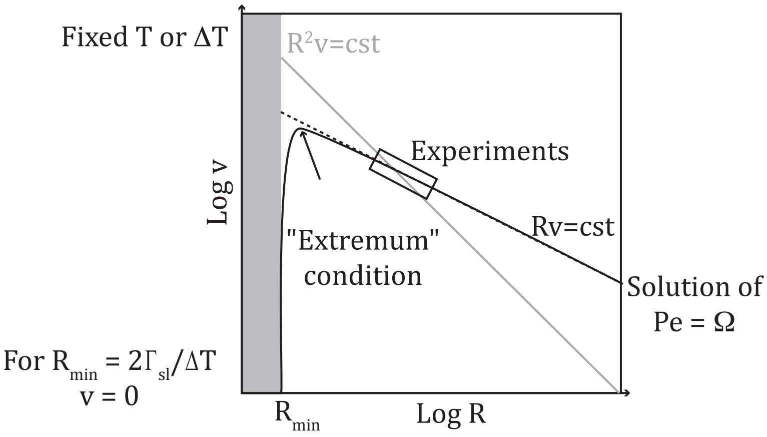

Figure 2.10: Log R – Log v plot showing: the growth limit given by the flux balance in dashed, the solution of $\Omega = Pe$ with the extremum condition in continuous, the region of experimental measurements represented by the rectangle and the marginal stability limit in gray.

Mullins and Sekerka stated that the planar front growth, even though it exists, is by definition an energetically unstable growth regime. Their approach in one dimension consists in determining the concentration profile in front of the growing planar front $c_\alpha(x)$ and destabilizing it along a second direction, with as first approximation a sinusoidal profile. The concentration in front of the destabilized interface is given in its general form by Equ. 2.40.

$$\tilde{c}(x,y) = c_\alpha(x) + a\epsilon\, sin(\omega y)\, exp(-bx) \tag{2.40}$$

with a and b parameters to be determined and ϵ and ω the amplitude and the pulsation of the sinusoidal destabilisation respectively. Applying the second Fick's law and the geometrical definition of the curvature, it is possible to determine a and b for a specific system, as it will be presented in chapter 6. The solute balance on the destabilized interface brings out the ratio $\frac{\dot{\epsilon}}{\epsilon}$ between the amplitude velocity and the amplitude in function of the wavelength of the destabilisation λ. This ratio corresponds to the test value of the destabilisation criterion. Indeed, if both terms have the same direction whether at a tip (both positive) or in a valley (both negative), then the ratio is positive, the absolute value of the amplitude will increase, meaning that the destabilisation is increasing. On the contrary, with opposite signs, the destabilisation will flatten and the planar interface will be stable.

$$\frac{\dot{\epsilon}}{\epsilon}(\lambda) > 0 \qquad \text{unstable interface} \tag{2.41}$$

$$\frac{\dot{\epsilon}}{\epsilon}(\lambda) < 0 \qquad \text{stable interface} \tag{2.42}$$

The ratio should be negative for every wavelength for the growth to be in a planar front mode. As already mentioned, the planar growth is not a stable regime. Therefore, if there is a possibility to grow in an energetically favourable mode, the destabilized one, the system will tend to it. Fig. 2.11 gives the typical $\frac{\dot{\epsilon}}{\epsilon}(\lambda)$ plot for a planar front growth and a destabilized

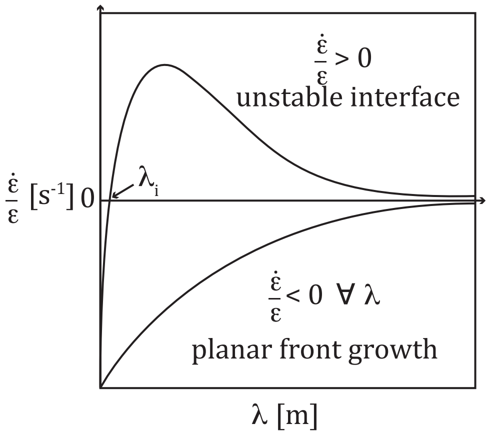

Figure 2.11: Plot of the stability criterion showing two typical behaviours: planar front growth $\frac{\dot{\epsilon}}{\epsilon} < 0 \forall \lambda$ and destabilised interface $\frac{\dot{\epsilon}}{\epsilon} > 0$

interface growth. Concerning the destabilised case, any wavelength λ larger than the solution $\frac{\dot{\epsilon}}{\epsilon} = 0$ will increase and the interface will be irregular. This solution corresponds to the marginal stability limit λ_i defined by Langer and Mueller-Krumbhaar and described in Equ. 2.39.

2.5 Aluminium-Iron system

This section presents the thermodynamic and crystallographic properties of the different phases found in the Fe – Al system. It also reviews the published studies concerning the morphology and the growth kinetics of these phases.

2.5.1 Thermodynamic data

The binary Fe-Al phase diagram is presented in Fig. 2.12 [23]. Above the melting point of Al and up to 912 °C, phases at equilibrium are, from the poorest to the richest in Al content:

$$\text{(Fe) } \alpha \quad \text{FeAl } \alpha_2 \quad \text{FeAl}_2\ \zeta \quad \text{Fe}_2\text{Al}_5\ \eta \quad \text{Fe}_4\text{Al}_{13}\ \theta \quad \text{liquid (Al)}$$

The three intermediate intermetallic compounds, namely Fe_2Al_5, Fe_4Al_{13} and $FeAl_2$, are characterized by a thin existence domain of a few atomic percent and a high melting point, above 1000 °C, in comparison with the aluminium one at 660 °C.

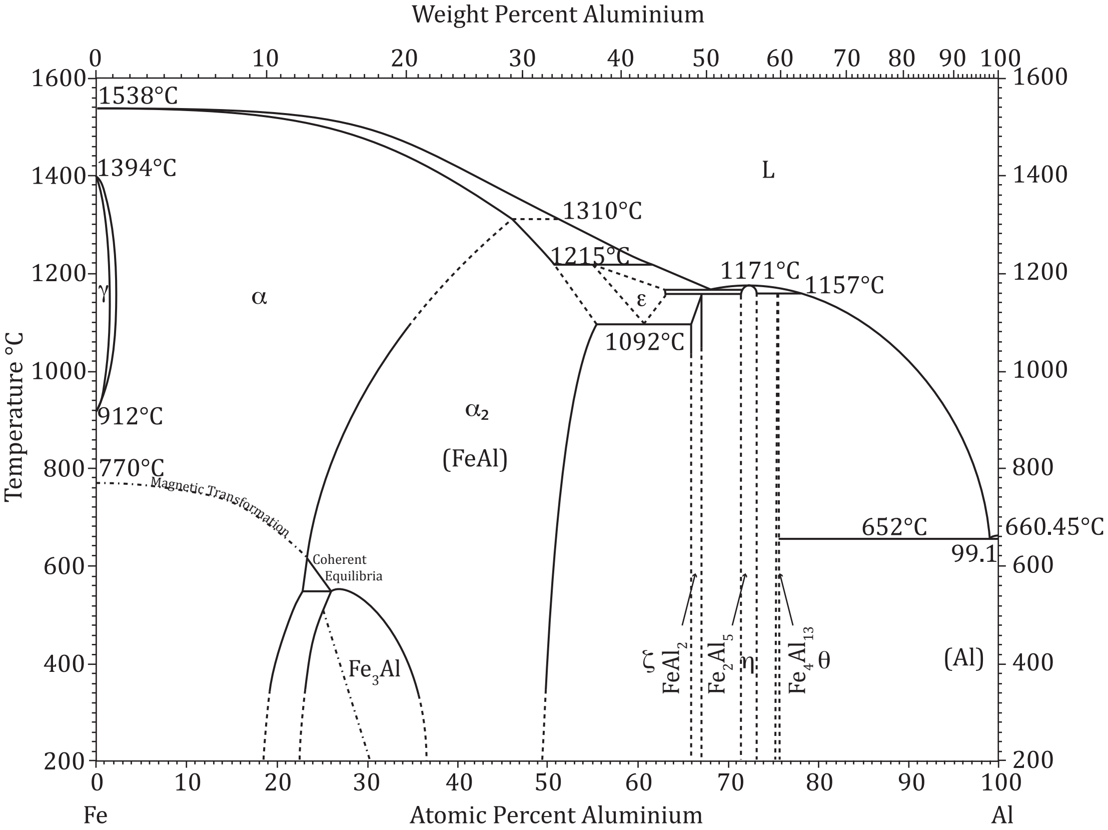

Figure 2.12: Binary Fe-Al phase diagram [23]

Many ternary systems involving iron and aluminium [24–27] were analysed using CALPHAD method (CALculation of PHAses Diagrams [28]) . Pure elements free energies G_i^{Φ}, with i the element and Φ the crystallographic structure, were obtained from the different cited sources together with the thermochemical Database for Light Metal Alloy [29] and are presented in Appendix 8.2. The energy expression as a function of the atomic fraction of each phase is given in table 2.2.

Table 2.2: Expression of the free energy as a function of the atomic fraction X, the temperature T for Fe bcc-α, FeAl ordered-α_2, FeAl, $\mathrm{Fe_2Al_5}$, $\mathrm{Fe_4Al_{13}}$ and liquid Al. L_{Φ}^{i} are the optimised interaction parameters obtained by CALPHAD method and used for this research.

(Fe) bcc-α

$$\begin{aligned}
G_{\mathrm{bcc}} &= (1-X)\,G_{\mathrm{Fe}}^{\mathrm{bcc}} + X\,G_{\mathrm{Al}}^{\mathrm{bcc}} \\
&\quad + RT\left(X\log(X) + (1-X)\log(1-X)\right) + X(1-X)\left(L_{\mathrm{bcc}}^{0} + L_{\mathrm{bcc}}^{1}(2X-1)\right) \\
L_{\mathrm{bcc}}^{0} &= \text{-122960.0} + 31.9888\ \mathrm{T} \\
L_{\mathrm{bcc}}^{1} &= 3089.2
\end{aligned}$$

FeAl ordered-α_2

$$\begin{aligned}
G_{\mathrm{FeAl}} &= X^2 G_{\mathrm{Al}}^{\mathrm{bcc}} + 2X(1-X)\,G_{\mathrm{FeAl}} + (1-X)^2 G_{\mathrm{Fe}}^{\mathrm{bcc}} \\
&\quad + RT\left(X\log(X) + (1-X)\log(1-X)\right) + X(1-X)\left(L_{\mathrm{FeAl}}^{0} + (2X-1)L_{\mathrm{FeAl}}^{1}\right) \\
&\quad + (1-X)X\left(L_{\mathrm{FeAl}}^{2} + (1-2X)L_{\mathrm{FeAl}}^{3}\right) \\
L_{\mathrm{FeAl}}^{0} &= \text{-22485.07} + 7.9772\ \mathrm{T} \\
L_{\mathrm{FeAl}}^{1} &= 368.15 \\
L_{\mathrm{FeAl}}^{2} &= \text{-24694.0} + 7.9772\ \mathrm{T} \\
L_{\mathrm{FeAl}}^{3} &= 368.15
\end{aligned}$$

$\mathbf{FeAl_2}$

$$G_{\mathrm{FeAl_2}} = \tfrac{2}{3}G_{\mathrm{Al}}^{\mathrm{fcc}} + \tfrac{1}{3}G_{\mathrm{Fe}}^{\mathrm{bcc}} - 33175.33 + 6.60T$$

$\mathbf{Fe_2Al_5}$

$$G_{\mathrm{Fe_2Al_5}} = \tfrac{5}{7}G_{\mathrm{Al}}^{\mathrm{fcc}} + \tfrac{2}{7}G_{\mathrm{Fe}}^{\mathrm{bcc}} - 32607 + 6.99T$$

$\mathbf{Fe_4Al_{13}}$

$$G_{\mathrm{Fe_4Al_13}} = 0.765G_{\mathrm{Al}}^{\mathrm{fcc}} + 0.235G_{\mathrm{Fe}}^{\mathrm{bcc}} - 30714 + 7.44T$$

(Al) liquid

$$\begin{aligned}
G_{\mathrm{liq}} &= (1-X)\,G_{\mathrm{Fe}}^{\mathrm{liq}} + X\,G_{\mathrm{Al}}^{\mathrm{liq}} \\
&\quad + RT(X\log(X) + (1-X)\log(1-X)) + X(1-X)\left(L_{\mathrm{liq}}^{0} + L_{\mathrm{liq}}^{1}(2X-1)) + L_{\mathrm{liq}}^{2}(2X-1)^2\right) \\
L_{\mathrm{liq}}^{0} &= \text{-91976.5} + 22.1314\ \mathrm{T} \\
L_{\mathrm{liq}}^{1} &= \text{-5672.58} + 4.8728\ \mathrm{T} \\
L_{\mathrm{liq}}^{2} &= 121.9
\end{aligned}$$

A particular calculation was made for the ordered α_2 structure, taking into account the reference free energy G_{FeAl} from sub-lattices systems $(\mathrm{Al}:\mathrm{Fe})_{0.5}(\mathrm{Al}:\mathrm{Fe})_{0.5}$. However, it is shown in Fig. 2.13, representing the free energy curves for the all stable phases at 700 °C, that this calculation leads to a free energy nearly identical to the one of pure α. This difference in energy between α and α_2 is considered as negligible due to the nature of the transition from one to the other. Indeed, the two phases lattice are nearly identical and the increasing in aluminium content will only lead to the ordering of the atoms. One observes the exact same free energy for $X_{\text{Al}}= 0.5$, a higher energy for FeAl at lower Al content and a lower energy for higher Al content with a maximum amplitude of $300\,\text{J}\cdot\text{mol}^{-1}$, which is negligible in comparison with absolute values.

As intermetallic compounds have a nearly stoichiometric existence domain, the calculation of their free energy is made by a linear combination of the pure element free energies weighted by their composition and corrected by additional optimized interaction parameters. As their existence domains are sharp, their representation in a $G(X)$ graph corresponds to dots, as presented in Fig. 2.13 (a). Fig. 2.13 (b) presents the same plot with common tangents to neighbouring phases. Intersection of the tangent with the vertical axis gives the chemical potential values μ_i of the interfaces in the system. For readability reason, the free energy curve of FeAl is not represented in this plot. In order to develop analytical models, a simplified phase diagram is built, taking into account three phases: α, liquid and the main intermetallic compound η. This phase diagram is limited to temperatures higher than melting point of aluminium as the free energy curve for solid (Al) was not calculated for this research.

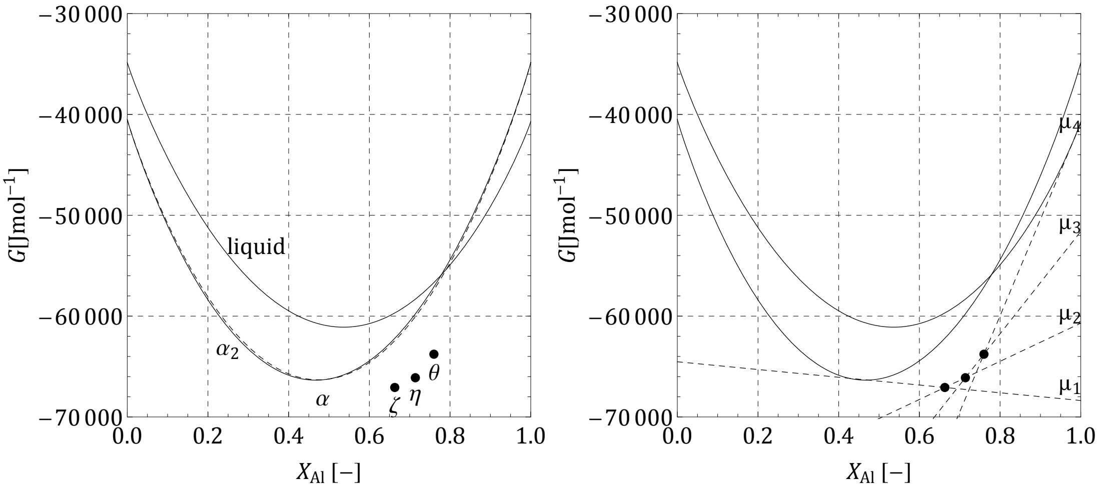

(a) (b)

Figure 2.13: (a): Calculated free energy curves of the different phases in presence at 700 °C (liquid, continuous: α, dashed: α_2 and dots: intermetallics). (b): Graphical determination of the chemical potentials at the interfaces between neighbouring phases for the same temperature (common tangents: dashed lines). Calculation made with values from [29].

2.5.2 Crystallographic data

Table 2.3 gives the crystallographic information of the Fe, the FeAl and the Al phases (in solid state) and table 2.4 the one for the intermetallic compounds. Densities are calculated at room temperature for the Al content given by the chemistry. The schematic representations of the unit cells show Fe atoms in red and Al ones in blue. Red, green and blue axes correspond respectively to a, b and c directions.

Table 2.3: Crystallographic information and theoretical density at room temperature for pure elements and FeAl phase in the Fe-Al

Fe α [30]	
chemistry	(Fe)
Al at.% at 700 °C	0 to 24
Pearson symbol	cI2
space group	Im$\bar{3}$m
cell parameters	a= 2.869 Å, $\alpha = 90°$
Fe atom per unit cell	$1 + 8 \times 1/8 = 2$
Volume per Fe atom	11.8 Å^3
density at RT	7853 kg· m^{-3}

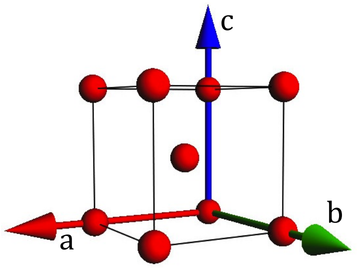

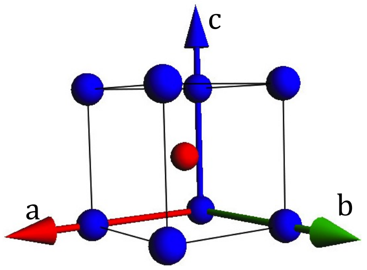

FeAl α_2 [31]	
chemistry	FeAl
Al at.% at 700 °C	24 to 51
Pearson symbol	cP2
space group	Pm$\bar{3}$m
cell parameters	a= 2.909 Å, $\alpha = 90°$
Fe atom per unit cell	$8 \times 1/8 = 1$
Volume per Fe atom	24.6 Å^3
density at RT	5583 kg· m^{-3}

Al [32]	
chemistry	(Al)
Al at.% at 700 °C	96.5 to 100
Pearson symbol	cF4
space group	Fm$\bar{3}$m
cell parameters	a=4.0495 Å, $\alpha = 90°$
Fe atom per unit cell	0
Volume per Fe atom	0 Å^3
density at RT	2698 kg· m^{-3}

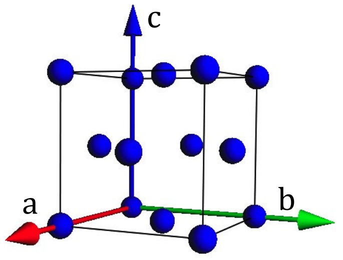

In the Fe_2Al_5 structure, a distinction is made between two types of Al atoms. Blue Al atoms have an occupancy of 1, violet ones have a lower occupancy, at 0.7. As it is mentioned in section 2.5.4, this particular structure is the cause of an anisotropy in diffusion of Al. Indeed, the violet atoms are aligned three by three along the z direction, forming Al atoms lines that are preferential ways for Al diffusion. Furthermore, the lower occupancy of those sites implying

Table 2.4: Crystallographic information and theoretical density at room temperature for intermetallic compounds in the Fe-Al system

	Fe_2Al_5 η [33]	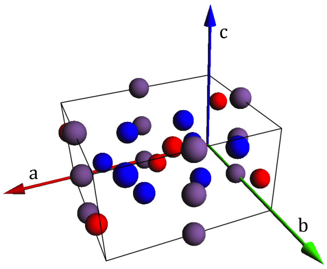
chemistry	Fe_2Al_5	
Al at.% at 700 °C	71 to 73	
Pearson symbol	oS15	
space group	Cmcm	
cell parameters	a= 7.65, b=6.41, c=4.21 Å, $\alpha = \beta = \gamma = 90°$	
Fe atom per unit cell	$2 + 4 \times 1/2 = 4$	
Volume per Fe atom	52.79 Å^3	
density at RT	4130.7 kg· m^{-3}	
	Fe_4Al_{13} θ [34]	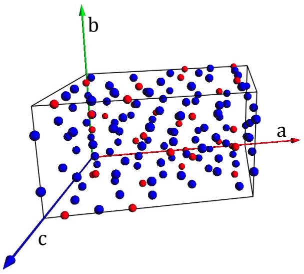
chemistry	Fe_4Al_{13}	
Al at.% at 700 °C	75 to 76	
Pearson symbol	mS102	
space group	C12/m	
cell parameters	a=15.49, b=8.08Å c=12.47Å, β=107.7°	
Fe atom per unit cell	$20 + 6 \times 1/2 + 8 \times 1/4 = 25$	
Volume per Fe atom	59.46 Å^3	
density at RT	3850 kg· m^{-3}	
	$FeAl_2$ ζ [35]	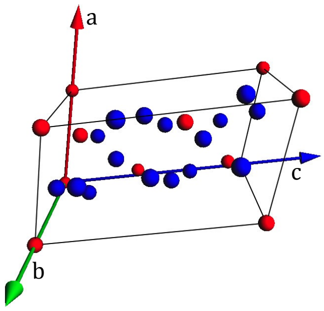
chemistry	$FeAl_2$	
Al at.% at 700 °C	66 to 67	
Pearson symbol	aP18	
space group	P1	
cell parameters	a=4.87, b=6.45 Å c=8.73Å, $\alpha = 87.9$ $\beta = 74.39$, $\gamma = 83.06°$	
Fe atom per unit cell	$4 + 8 \times 1/8 = 5$	
Volume per Fe atom	52.4 Å^3	
density at RT	4330 kg· m^{-3}	

intrinsic vacancy presence, atoms' movement is further facilitated. Diffusion is thus faster along this direction.

With the number of Fe atoms per unit cell and the volume of the latter, it is possible to determine the volume occupied by one Fe atom as presented in Tables 2.3 and 2.4. The comparison of these values allows to have a qualitative information on the stress at the interface as mentioned in section 2.3. For example, an Fe atom occupies five times more volume in Fe_2Al_5 than in pure Fe.

2.5.3 Published experiments

Intermetallics formation was investigated by mainly two types of experiments, depending on the research field. Groups interested in aluminizing proceeded by *reactive diffusion bonding* (RDB) [11, 36–48] while other groups used *dipping-test* method (DT) [10, 49–67]. *Reactive diffusion bonding* consists in a two-steps procedure. The Fe substrate is first covered by aluminium through different methods, e.g. immersion or sputtering, and then heat treated at different temperatures and for different times. Dipping test consists in immersing an iron sample in an aluminium bath at different temperatures and for different times. Sample has usually a cylindrical geometry and can be rotated during experiment. The main differences between these two techniques are the following:

- The possibility of proceeding below the melting point of aluminium for reactive diffusion bonding test.
- The orientation of the interface between Al and Fe: vertical in dipping tests and generally horizontal in reactive diffusion bonding test, at least in the present review.
- The amount of aluminium, considered as infinite for dipping test and limited in the reactive diffusion bonding.

Observations of the system slightly differs depending on the experimental procedure, in terms of morphology and kinetics. In addition, more complex experiments were done e.g. by Tanaka *et al.* [11, 44] who heated the two pure elements separately before putting them into contact. As the initial interface is horizontal it was chosen here to relate this type of diffusion couple experiment to RDB measurements. Jiang [67] also used an exotic procedure, drilling a hole in an Al block to insert a Fe rod. This technique is considered as a variant of dipping test as the interface is vertical.

2.5.4 Morphology

A typical profile that results from the interaction between iron and liquid aluminium was observed by Bouché *et al.* [56] and presented in Fig. 2.14 . A thin Fe_4Al_{13} (or $FeAl_3$) layer of the order of $10\,\mu$m grows on the aluminium side (black contrast, bottom) and a thicker phase, the Fe_2Al_5, grows as tongues of the order of 100µm in length, mainly into the Fe specimen (white contrast, top) [44]. It was shown through electron back scattering diffraction (EBSD) observations that the tongues are nearly single crystallites [45]. Eggeler *et al.* were the first to propose that this structure is due to the anisotropy of the diffusion coefficient in Fe_2Al_5 [52]. Furthermore, Bouayad *et al.* [58] and Tanaka *et al.* [44] gave as possible explanation the favourable diffusion path of aluminium atoms along the c-axis of the Fe_2Al_5 orthorhombic structure, which is composed of pure Al but vacancy rich ranges, as presented in section 2.5.2. They proposed that the growth direction is parallel to the c direction because during nucleation, grains with their c-axis perpendicular to the interface are favoured in term of Al supply [44]. In

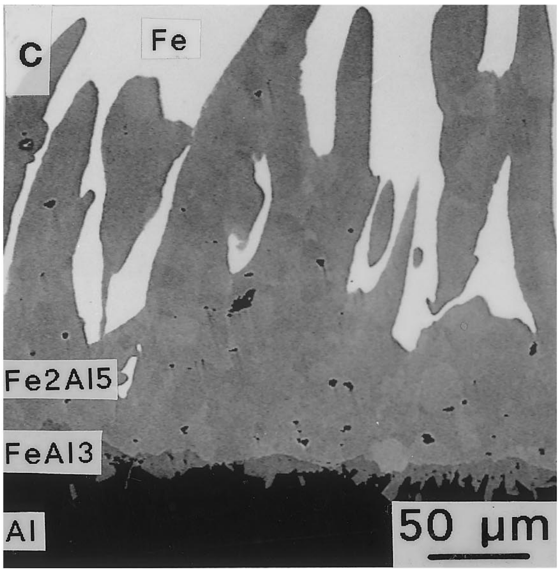

Figure 2.14: from [56], SEM micrography of an interface between iron and liquid aluminium after a dipping test of 15 min at 800 °C.

addition, Kwon *et al.* [51] and Eggeler *et al.* [68] showed few years later that this feature has no link with the grain size of the ferrous substrate.

Tongue microstructure

The internal microstructure of the tongue tips was investigated, by transmission electron microscopy (TEM). A periodic pattern was observed by different groups [69, 70] as presented in Fig. 2.15. Interpretations of this contrast differ. For Lapin *et al.* [69] (Fig. 2.15(a)) it is due to

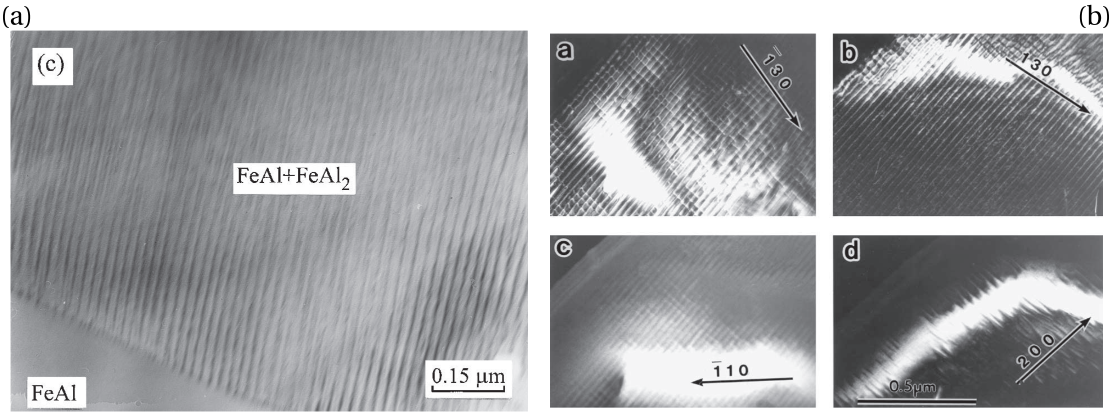

Figure 2.15: TEM observation of the intermetallic phases: (a) Lapin [69] proposed that this microstructure is due to the co-presence of α_2 FeAl and FeAl$_2$ (b) Hirose [70] justified this structure by nano twinning.

the coexistence of FeAl and $FeAl_2$ while Hirose *et al.* [70] described it as nano twins forming in the Fe_2Al_5 tongues due to stress implied by the growth.

Mechanical properties

Kobayashi *et al.* [38] realized measurements of Vickers micro-hardness (HV) on the different phases and obtained, for pure aluminium, HV < 100, pure iron HV = 200 and a hardness between 800 and 1200 for the Fe_2Al_5 phase, depending on contact time and bath temperature. By increasing bath temperature they were also able to form the Fe-rich phases Fe_3Al and FeAl, which are more ductile and thus present better mechanical properties with a HV between 300 and 700. They were not able to determine the HV of Fe_4Al_{13} because of its low thickness of approximately 10 µm that did not allow proper indentation as diagonals of the indentation were also approximately 10 µm long. However, this important difference of ductility between the Al-rich intermetallic compounds and iron can imply internal stress fields and subsequent plasticity, in particular of the Fe.

Flattening of the intermetallic-iron interface

Tanaka *et al.* showed that the tongue-like structure decreases with increasing temperature, tending towards a nearly flat layer above 800 °C [44]. They explained this modification by the decrease of the interdiffusion coefficient anisotropy. They also showed that the inter spacing between neighbouring tongues decreases with time, meaning that thickening occurs in the Fe_2Al_5 phase. It has to be mentioned that observations were made on reactive diffusion bonding samples, implying a full consumption of Al. Dipping tests of pure iron into pure aluminium did not show such a behaviour. However, Kwon *et al.* [51] showed that Si or C addition flattens the interface between Fe_2Al_5 and Fe, thus decreasing the tongue-like structure. Danzo *et al.* [63], working on aluminium coating of electrical steel of different Si content, reached the same conclusion. Finally, Barbier *et al.* [54], comparing the corrosion of a martensitic steel to the one of an austenitic steel, concluded that Ni addition also flattens the intermetallics-Fe interface.

2.5.5 Kinetics

Intermetallics thickness

Many research groups studied the growth by measuring the thickness of intermetallic layers, especially Fe_2Al_5, for different contact times. The classical way is to measure the mean position between the tip and the valley [44] or the mean position of each tips [56, 58]. Another way is to determine the total surface of the intermetallic compound and to divide it by the width of the region of interest [66]. Either way gave a parabolic behaviour of Fe_2Al_5 thickness as a function of the time, explained by a thermal diffusion controlled mechanism [40]. This first section reviews measurement of the intermetallics thickness by comparing both experimental procedures, i.e. dipping test and reaction diffusion bonding. A general fit was done for each of them expressing the thickness W as a function of time and temperature as follow:

$$W(T,t) = K_0 \exp\left(\frac{-Q}{RT}\right)\sqrt{t} \tag{2.43}$$

Fig. 2.16 presents the measured thickness W as a function of the test temperature and time. It also presents surface fitted on data found in the literature. Fig 2.16 (a) and (b) present the data for dipping tests and reaction diffusion bonding tests, respectively.

The global fitting parameters that are the growth constant K and the activation energy Q derived from the fits presented in Fig. 2.16 are given in table 2.5.

Table 2.5: Growth constant K and activation energy Q of Fe_2Al_5 in the Fe-Al system for the two experimental procedures obtained by the fitting of data found in the literature.

Test type	K_0 [m· $s^{-1/2}$]	Q [kJ·mol^{-1}]	t range [s]	T range [°C]
Dipping test	4.21×10^{-5}	15.8	2 - 3600	660-1000
Reactive diffusion bonding test	2.11×10^{-3}	49.3	72 -7200	550 - 820

Although those fits give rough estimations of the Fe_2Al_5 growth and cannot be considered to give a full description of the kinetics, they give an indication on their difference. Indeed, the fitted activation energies are of the same order of magnitude, showing that whatever the type of experiment used, temperature has the same effect on the kinetics. On the contrary, the calculated growth constant for the dipping test is 50 times smaller than for reaction diffusion bonding. This important difference is associated in dipping test with the dissolution of the intermetallics in the melt during growth, which was not taken into account in the measurement of W as suggested in section 2.1.5. Although in the present research both test configurations were performed, the quantification will be preferentially done on horizontal interface samples, which should suffer a lesser dissolution as natural convection should, if any, be negligible (see section 5.3).

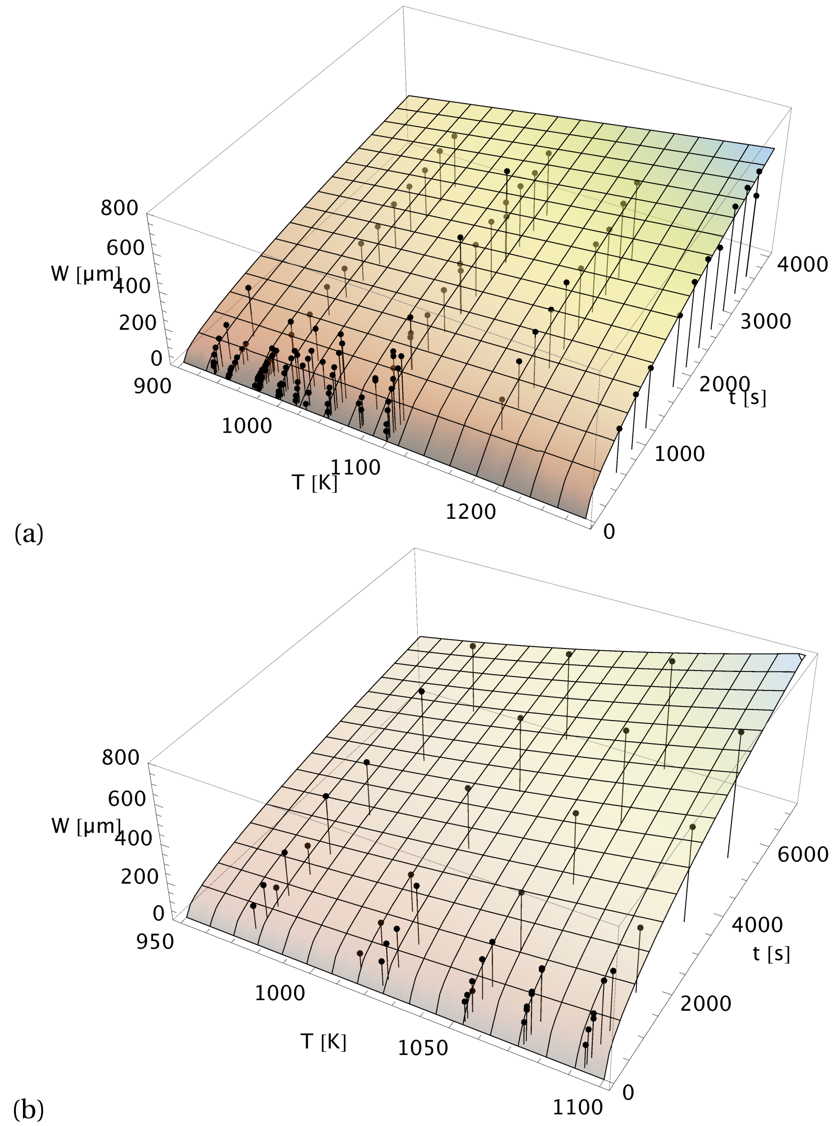

Figure 2.16: Review of measured intermetallic thickness W with respect to time and temperature respective fits: (a) dipping tests from W measurements of [10, 50, 58, 62, 64, 66], (b) reactive diffusion bonding from W measurement of [11, 12, 39, 41, 44, 46]

Growth constant coefficients

Table 2.6 presents the growth constants *K* at 700 °C found in the literature. As the experimental procedure and the measurement method play an important role, they are also mentioned. Growth constant are directly reported for Yermenko [10] and Hibino [64]. Others are deduced from reported thickness. The growth constants are of the same order of magnitude for all measurements, except the value reported by Yeremenko who took Fe dissolution into consideration and found the double of the other values. With this information it appears that reported growth constants are related to *apparent growth* and that deduced interdiffusion

Table 2.6: Growth constant K from literature: calculated from thickness measurement or directly reported: RDB: reaction diffusion bonding. DT: dipping test.

Experiment	Measurement	K $[ms^{-1/2}]$	Remarks	Ref.
RDB	not mentioned	4.6×10^{-6}	from W data	[46]
RDB	mid trunk	6.6×10^{-6}	from W data	[44]
DT	tongue tip	5.4×10^{-6}	from W data	[71]
DT	tongue tip	6.9×10^{-6}	from W data	[62]
DT	conversion factor	7.0×10^{-6}	transformed Fe	[64]
DT	not mentioned	14.1×10^{-6}	dissolution	[10]

coefficients resulting from the estimation of Equ. 2.16 are also apparent ones.

2.5.6 Diffusion coefficients

Diffusion coefficient of Al tracer

The Al tracer diffusion coefficients in the different phases are given in Fig. 2.17. Self-diffusion

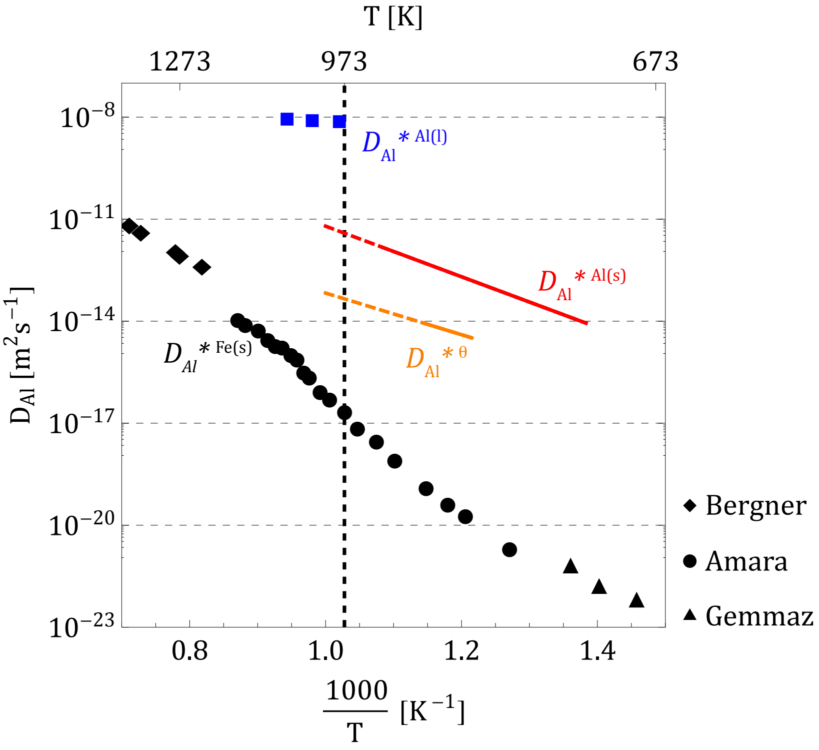

Figure 2.17: Diffusion coefficient of tracer Al in the different phases: $D_{Al}^{*Al(l)}$ [72], $D_{Al}^{*Al(s)}$ and $D_{Al}^{*Fe_4Al13}$ [3], D_{Al}^{*Fe} [6, 73, 74].

in liquid Al in blue is taken from Kargl *et al.* [72], who used incoherent quasi elastic neutron scattering to determine self diffusion at three different temperatures. Evaluated $D_{Al}^{Al(l)}$ value at 700 °C is of $7.2 \times 10^{-9}\,\mathrm{m^2 \cdot s^{-1}}$. Self-diffusion in solid Al [3] is given in red. Temperature range of the measurement being lower than 700 °C, the dashed line represents the trend used to estimate the coefficient. Thus, $D_{Al}^{*Al(s)}$ estimated at 700 °C is equal to $3.8 \times 10^{-12}\,\mathrm{m^2 \cdot s^{-1}}$. A single estimation of tracer diffusion in Fe-Al intermetallic compound was found in the literature for the θ Fe_4Al_{13} phase. It is reported in orange with the projection in dashed. Its value at 700 °C is equal to $4.5 \times 10^{-14}\,\mathrm{m^2 \cdot s^{-1}}$. Diffusion of Al in iron is given by three sets of data at different temperature ranges [6,73,74]. The shift observed at 1043 K, the Curie temperature of pure iron, makes the diffusion coefficient value decrease faster at lower temperature. It is due to the change in magnetism of the α phase, from paramagnetic at higher temperatures to ferromagnetic at lower ones. This results in a low diffusion coefficient of Al in pure iron of $1.9 \times 10^{-17}\,\mathrm{m^2 \cdot s^{-1}}$, lower than the one in the other phases.

Diffusion coefficient of Fe tracer

Tanaka [11] reviewed data of Fe diffusion in liquid aluminium. The two extremum values are given in blue in Fig. 2.18. At 700 °C, the diffusion coefficient is within 2×10^{-9} and $5 \times 10^{-8}\,\mathrm{m^2 \cdot s^{-1}}$. Diffusion in solid Al is estimated at 700 °C at $7.5 \times 10^{-13}\,\mathrm{m^2 \cdot s^{-1}}$ while the

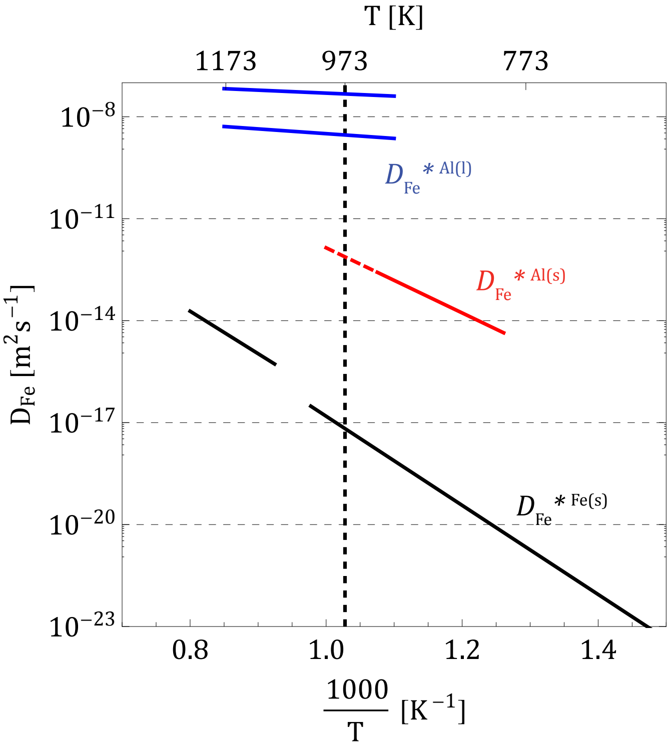

Figure 2.18: Diffusion coefficient of tracer Fe in the different phases: $D_{Fe}^{*Al(l)}$ [11], $D_{Fe}^{*Al(s)}$ [3], D_{Fe}^{*Fe} [75].

one of self-diffusion is equal to $6.6 \times 10^{-18}\,\mathrm{m}^2 \cdot \mathrm{s}^{-1}$. One can remark that as for diffusion of Al in Fe, the evolution of the coefficient with temperature is also slightly modified at Curie temperature.

Interdiffusion coefficient in Fe_2Al_5

Kajihara [12] developed a mathematical model to precisely determine interdiffusion coefficient in Fe_2Al_5, considered here as the only intermetallics forming. At 700 °C they obtained an interdiffusion coefficient $\tilde{D}$ of $3.5 \times 10^{-13}\,\mathrm{m}^2 \cdot \mathrm{s}^{-1}$. Tanaka [11] proceeded the same way than for tracer diffusion of Fe in liquid Al by reviewing different authors. Their own measurements appeared lower than the reviewed ones. Extremum results from Tanaka's review are given in light and dark red and are surrounding Kajihara one. Furthermore, estimated interdiffusion coefficient from the growth constant coefficients of table 2.6 using Equ. 2.16 are presented as red dots at 700 °C. One can remark that those estimations from the highest and the lowest K values of table 2.6) are within the domain described by Tanaka with respectively $2 \times 10^{-12}\,\mathrm{m}^2 \cdot \mathrm{s}^{-1}$ and $2 \times 10^{-11}\,\mathrm{m}^2 \cdot \mathrm{s}^{-1}$, respectively for the lowest and the highest growth constant. Finally, in order

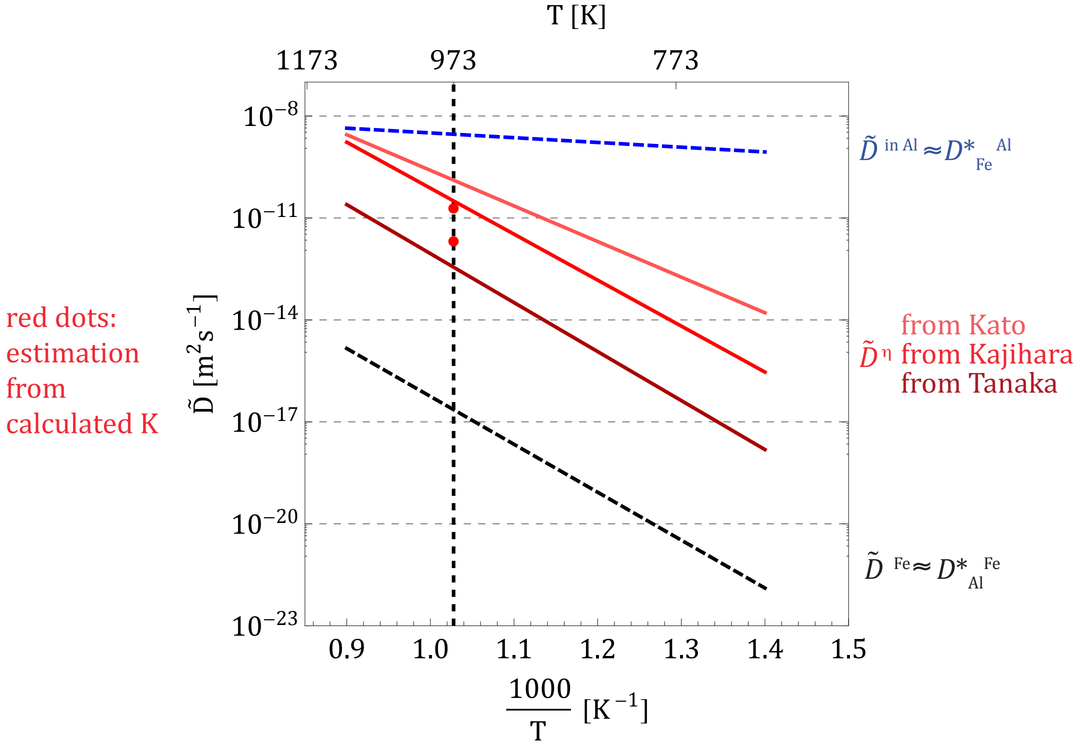

Figure 2.19: Interdiffusion coefficient in Fe_2Al_5. Red lines: from Tanaka [11], Kajihara [12], Kato (reviewed in [11]). Red dots from K measurements of table 2.6 using Equ. 2.16 with data from Torres [46] (lower value) and Yeremenko [10] (higher value). Dashed lines are estimated interdiffusion coefficient in nearly pure Fe and Al from Amara [6] and Tanaka [11] respectively.

to compare those values with diffusion in pure phases, tracer diffusion plots of one element in the phase formed by the other one are drawn in Fig. 2.19. As in Equ. 2.18 if $X_A \rightarrow 0$ then $\tilde{D} = D_A$ which corresponds in this particular situation to D_A^*, then tracer diffusion coefficients can be compared to interdiffusion coefficients.

2.5.7 Intermetallics dissolution

Although dissolution plays an important role in the kinetics description of the system, only few groups studied it. Some qualitative information can be found and are reported here. Jiang *et al.* [67] observed precipitates in the aluminium phase after the solidification. They also observed that precipitates are smaller when away from the interface, and that the interface is quite regular, only exhibiting small serrations. Shivpuri *et al.* [76], studying the weight loss of dipping tested steel samples, concluded this was due to the direct dissolution and intermetallic detachment from the substrate. They also observed that turbulence dramatically accelerates the sample dissolution. Giorgi *et al.* [77] proposed a mathematical model for galvanization reaction of steel by Zn-1%Al alloy, taking into account nucleation on the interface and iron dissolution rate as a first order reaction falling to zero with bath saturation it can predict the concentration of Fe and Al in the ternary system and especially in intermetallic layers, the nucleation rate and the time necessary to form a continuous layer.

Finally, Yeremenko *et al.* [10] studied intermetallics growth taking into account the dissolution rate k of iron in the Al bath. He proceeded by rotative dipping test (section 3.2.2) to force the convection in the bath. The dissolution of the solid metal in the liquid one was described in terms of mean species concentration in the melt:

$$\bar{c}(t) = c_s\left(1 - \exp\left(-\frac{kSt}{V}\right)\right) \tag{2.44}$$

with c_s the saturation concentration in $\mathrm{kg \cdot m^{-3}}$, S the specimen surface in $\mathrm{m^2}$, V the melt volume in $\mathrm{m^3}$ and k the dissolution rate in $\mathrm{m \cdot s^{-1}}$. Measuring the bath concentration with time, he obtained the dissolution rate constant from Equ. 2.44. In order to determine the diffusion coefficient of the dissolved species through the boundary layer, he used the following relation:

$$k = 0.554 I^{-1} D_\delta^{2/3} \nu^{-1/6} \omega^{1/2} \tag{2.45}$$

with D_δ the diffusion coefficient in the boundary layer in the liquid in $\mathrm{m^2 s^{-1}}$, ν the kinematic viscosity in $\mathrm{m^2 \cdot s^{-1}}$ of the melt, ω the sample rotation speed in rpm and $I = f(Sc)$ the correction factor of the Schmidt number *Sc*. He obtained a constant dissolution rate k for Fe in Al at 700 °C $k = 3.8 \times 10^{-5}\,\mathrm{m \cdot s^{-1}}$.

3 Investigation methods

This chapter presents the different tools used to study Fe–Al interaction. Section 3.1 presents the materials used for fundamental and technological investigations. The two next sections focus on *post mortem* observation with a description of sample production (section 3.2) and observation methods (3.3). Contact times for these tests were chosen in the interval between 15 and 90 min every 15 min. A description of the X-ray *in situ* set-up and the sample preparation is given in section 3.4. This observation method allows to follow the evolution of the intermetallics layer with a time resolution of 2 min. Section 3.5 describes the way the raw data is treated in order to quantify the results and to construct three-dimensional representations. Finally, the one-dimensional numerical model developed to predict Fe-Al diffusive reaction is described in section 3.6.

3.1 Materials

3.1.1 Materials used for fundamental investigations

Fundamental investigations are performed with pure elements in order to understand the basic mechanisms leading to the formation of the observed intermetallic compounds. The starting materials are Armco ferritic iron (99.98 %) provided by AKSteel and high purity aluminium 5N (99.999 %) provided by Pechiney . Table 3.1 gives impurity content in the Armco Fe.

Table 3.1: Chemical composition of Armco pure iron provided by AKSteel (impurities wt%).

Element	C	Mn	P	S	N	Cu	Fe
wt%	0.02	0.2	0.015	0.015	0.007	0.06	balance

3.1.2 Materials used for technological investigations

Technological investigations are performed on two different ferrous substrates, namely a ferritic steel 1.2343 provided by Allper and a grey cast iron C-31 provided by Centricast. Table 3.2 gives their composition.

Table 3.2: Chemical composition of the 1.2343 ferritic steel and the grey cast iron used for technological investigation in wt%.

Element	C	Mn	Si	P	S	Cr	Cu	Mo	Ni	Sn	V	Fe
1.2343	0.4	-	1.0	-	-	5.3	-	1.3	-	-	0.4	balance
C-31	3.0	0.7	1.8	0.4	0.05	0.3	0.4	0.4	0.06	0.1	-	balance

1.2343 is actually the steel currently used for the shot sleeve of the die casting facilities. C-31 is a potential material to replace the 1.2343. In order to increase 1.2343 wear resistance, coatings were also deposited. To types of coating are deposited, namely a Ni-based and a Co-based one. Furthermore, powders can be added in the Ni-based coating as inert charges to improve properties of the layer. Coatings were deposited by Atela in Neuchâtel, Switzerland. Table 3.3 gives the three main batches that are tested in the present study:

Table 3.3: Coating types deposited on 1.2343 for the present study.

#	Alloy	Remarks
1	Ni-based	different grades in Ni alloy
2	Ni-based + charges	AlN, Al_2O_3, Mo, B
3	Co-based	-

In order to make the coating denser and to improve its mechanical properties, a heat treatment at 600 °C during 3.5 h was performed after the deposition. In addition to the coating, BoreFuse™ paste provided by Surface Technology Inc. was added to a Ni-based sample before the heat treatment in order to charge the coating in boron. It is associated to the second batch.

All those samples are tested by dipping test (see section 3.2.2) in a pure Al bath. In addition, dipping tests in the Silafont-36 aluminium alloy provided by Rheinfelden is performed. Table 3.4 gives the chemical composition of the latter.

Table 3.4: Chemical composition of Silafont-36 aluminium alloy in wt%.

	Si	Fe	Cu	Mn	Mg	Zn	Ti	Sr	Al
wt%	9.5-11.5	0-0.15	0-0.03	0.5-0.8	0.1-0.5	0-0.08	0.04-0.15	0.01-0.02	balance

3.2 Sample testing

3.2.1 Liquid Metal Immersion Facility

Fig. 3.1 gives the schematics of the *Liquid Metal Immersion Facility* (LMIF).

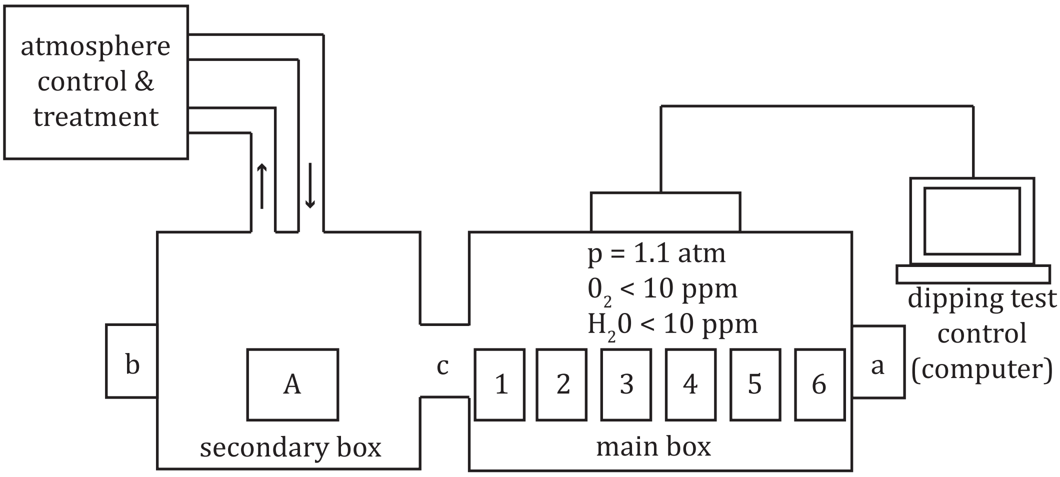

Figure 3.1: Schematic of the Liquid Metal Immersion Facility. The main box contains six furnaces (1-6) dedicated to dipping tests. In the secondary box a regular furnace (A) is used for planar-interface sample production. The two boxes are connected by an airlock (c) that can be closed in order to use either boxes separately. Double-door entrances (a and b) are used for external exchanges.

It is composed of two glove boxes: the main one is hosting six furnaces (1 to 6) that are dedicated to dipping tests. They are presented in section 3.2.2. The secondary box is hosting a regular furnace (A) in which the horizontal interface sample are produced. This method is presented in section 3.2.3. Humidity and oxygen levels are controlled by a MBraun LM 20G LMF device, which filters the atmosphere to keep them under 10 ppm. A slight overpressure is kept in the LMIF in order to avoid air intake from outside. Two double-doors entrances (a) and (b) are used as airlocks for the introduction or the withdrawal of parts, such as equipment and samples before and after test. A third airlock (c) located between the glove boxes can be closed in order to work only in one of the two boxes. The control of the six furnaces in the main box is made through a Matlab routine. The regular furnace is not connected to the computer system and is thus controlled manually.

3.2.2 Sample with vertical interface (dipping test)

Dipping test is the main testing method used for the fundamental as well as for the technological research of this work. The latter is fully completed with this technique. Fig. 3.2 presents a picture of one of the six furnaces (a) and the schematics of its central part containing the crucible (b). The central part consists of a cylindrical steel box (furnace in Fig. 3.2 (a)), containing

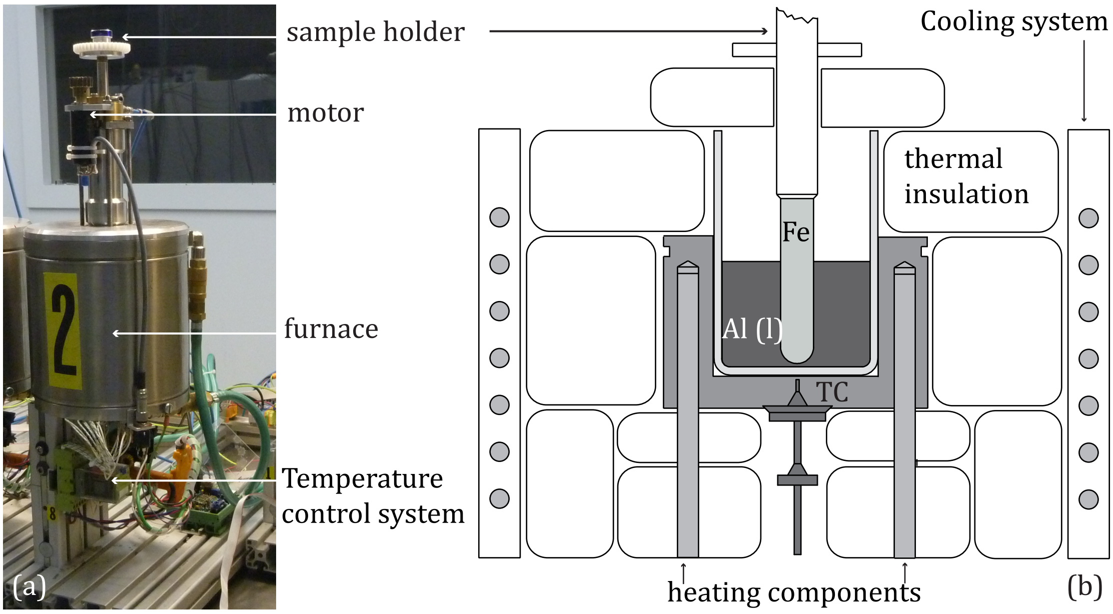

Figure 3.2: (a) Picture of one of the six furnaces dedicated to dipping tests with the central part containing the crucible and detailed in (b), with the sample-holder and the temperature control system.

a boron nitride crucible, which is surrounded by the heating system. The heating system is made out of a steel container in which six heating components are inserted. A thermocouple (TC) is placed in contact with the crucible bottom to control the temperature. A shift of about 30 °C between the Al melt and the measured temperature was observed due to the thermal insulation of the crucible. A calibration of each furnace has been performed in order to get a bath temperature of 700 °C with a stability precision of ±10 °C. Between the external steel wall and the crucible, an insulating material is placed to limit heat loss and stabilise the bath temperature. The steel wall is cooled down by a water circulation system in order to limit the heating of the glove box atmosphere.

The sample holder is a vertical axis on which the sample is screwed. It allows two vertical positions by means of an air piston. The standby position keeps the sample above the molten bath and the engaged position maintains it 2 mm above the crucible bottom, in the melted Al. Two cogwheels driven by an electrical motor and situated on the top of the sample holder allow to rotate the sample during the experiment. The rotation speed is controlled by a Matlab routine. The input is given as an electrical potential U from 0 to 255 V and the corresponding rotation speed ω is given by:

$$\omega = 6.135 \times U \qquad [\text{rpm}] \tag{3.1}$$

The ferrous sample is prepared as a cylinder of 10 mm in diameter and 50 mm in height with one hemispheric end at the bottom and a thread on the other one to fix it to the sample holder. The total mass of one finger before dipping test is about 28 g for a bath mass of 125 g.

The Al bath is first melted at 700 °C. During this time, the finger is kept at room temperature. Once the bath temperature is stabilised, approximately two hours after the beginning of the heating, the finger is inserted in standby position and preheated during 2 min. Then, the finger is inserted in the melt at the so-called engaged position and maintained for the chosen time. Immersion time is 15, 30, 45, 60, 75 and 90 min. One longer immersion time of 180 min is also performed for fundamental investigation. Once contact time is reached, the finger is removed from the bath, cooled down to room temperature by local atmosphere in the glove box and extracted to be prepared for *post mortem* investigation (section 3.3).

3.2.3 Samples with horizontal interface

In order to limit convection effects, samples with planar interface are produced and tested in a regular furnace placed in the secondary glove box. This sample production method is exclusively used for the fundamental research and thus only pure iron – pure aluminium couples are tested. Iron parts are produced by cutting one finger to obtain cylindrical slices 2 mm thick, 10 mm in diameter. Those pellets are mechanically polished with SiC paper 4000 just before insertion in the glove box. 3 g of pure Al is prepared from the same batch used as the one for dipping tests.

The aluminium is melted in an alumina crucible, sprayed with boron nitride suspension to avoid sticking. An immersed thermocouple controls its temperature. A boron nitride cylindrical crucible, described in Fig. 3.3, is also placed in the furnace to be preheated. The crucible is made of to parts. The base is a disc 5 mm thick and 30 mm in diameter that is screwed to the upper part, a cylinder of internal diameter 10 mm, with a height of 30 mm. The upper part is a funnel that facilitates the pouring of the melt. Once the melt and the

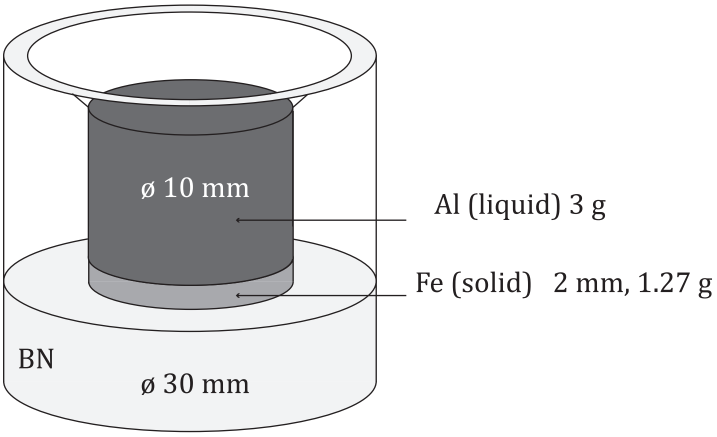

Figure 3.3: Schematics of the planar interface sample testing set-up. A cylindrical iron pellet is placed at the bottom of a boron nitride crucible (BN), which is filled with liquid Al at 700 °C and kept at this temperature for a chosen time. Lateral crucible wall are made transparent to see the sample.

crucible are stabilised at 700 °C, the furnace is open, the iron pellet deposited in the crucible and the melt poured over the pellet. Then, the filled crucible is placed in the furnace and the thermocouple plunged in it to control temperature during immersion time. The total manipulation lasts less than 10 s and the melt temperature is stabilised at 700 °C after about 5 min. At the end of the contact time, the crucible is removed from the furnace, deposited in the glove box and cooled down to room temperature before unmoulding. It is then removed from the glove box to be prepared for *post mortem* investigation.

3.3 *Post mortem* observations

3.3.1 Sample preparation

In order to observe the result of the interaction between the two metals, samples are cut across the interface and polished. Both sample types, dipped fingers or planar interfaces, are prepared the same way. The cut revealing the interface is made with a SiC disc saw (Struers Accutom-2). Fingers are cut at 44 mm from its flat base (not immersed one). Planar interface samples are cut along the vertical axis in the diameter. Samples are embedded with an electronic conductive resin (Buehler Konductomet) in an embedding facility (Struers LaboPress-3) and mechanically polished on a rotary polisher (Struers Labopol - 5) with silicon carbide grinding papers with grain sizes 600, 2500 and 4000 (Buehler Met II) and diamond pastes with decreasing grain size: 6, 3, 1, 0.25 µm (Buehler Metadi Diamond Polishing Compound). Final step is a mechanical polishing using a colloidal silica solution with a grain size of 0.2 µm (Struers OP-S suspension).

The grain structure of the iron is revealed with chemical etching by immersing the polished sample for 5 s in nitric acid HNO_3 50 vol%. Keeping the sample immersed during several hours in this solution allows to totally dissolve the iron while preserving the intermetallics and remaining Al [45]. This technique is used to reveal the tongue-like structure, as presented in Fig. 4.2.

3.3.2 Light Microscopy

Light Microscopy is used to control the quality of the polishing and also to obtain a global overview of the sample as presented in Fig. 4.1 by means of image stitching. Image stitching consists in recording grid of images that are overlapping each other. Then, with a dedicated software (Fiji ImageJ open source software [79]), the images are put together to form one single image of large dimensions with a better resolution than a single one recorded at lower magnification. For this, an Olympus BX60 Light Microscope is used and image acquisition is made with an Olympus Colorview III u camera and AnalySIS docu™acquisition software.

3.3.3 Scanning Electron Microscopy

Scanning electron microscopy (SEM) consists in a discrete scanning of the sample with an electron beam focused to the nanometre size and recording the emitted signal at each scanned point. Three main signals are acquired this way: secondary electrons (SE), back scattered electrons (BSE), and by means of an energy dispersive X-rays spectrometer (EDS). They are presented hereafter. SEM observations are performed at the CIME on a FEI-XLF30, which allows in addition to the acquisition of these three signals, the acquisition of electron back scattered diffraction (EBSD). EBSD is based on the recording of a full camera image at each scanning point, which gives crystallographic information. In addition, a focused ion beam (FIB) Carl Zeiss NVision 40 at PSI, Villigen is used for TEM lamella preparation and the same microscope in CIME is used for three dimensional imaging. These two techniques are also described in the present section.

Secondary electrons (SE) result from inelastic interactions between the incident beam and the atoms of the sample and are emitted when the energy transferred is sufficient for them to escape the specimen. Thus, SE are of low energy (<50 eV) and those escaping from the sample and reaching the detector come from the near sample surface. Furthermore, the number of detected SE depends on the sample inclination relatively to the incident beam. The resulting contrast is thus due to topographic variations of the sample's surface [80]. Apart from few particular observations, as samples are generally polished, topographic information was not relevant for the present research.

Back-scattered electrons (BSE) are incident electrons that suffer one or more quasi elastic interactions with the sample before escaping and being detected. Their energy is thus of the order of magnitude of that of the incident beam. The scattering is mainly affected by the atomic number Z of the observed element. The ratio between BSE and the incident beam intensities increases with Z. A chemical contrast is thus obtained. Contrary to SE, as BSE have a high energy, they do not come from the near surface of the sample. Therefore, the collected signal in a specific position contains information from a larger volume than for SE. This interaction volume limits then the resolution, in comparison with SE [80]. In the Fe – Al system, with respective Z of 26 and 13, for Fe and Al, the pure Fe matrix appears brighter and phases are progressively darker with increasing Al concentration. The main information relevant for this work comes from back-scattered electrons.

X-ray energy dispersive spectrometry (EDS) allows the identification of the elements forming a phase by the detection of X-rays emitted by the sample. When an incident electron kicks out an electron from the core atomic level of an atom, one electron of the outer shell will decrease its energy to replace the missing one. The energy difference is emitted as a photon, which is characteristic of the transition. As different transitions are possible for a given element, it emits X-rays at different energies, which are forming a characteristic spectrum. The energy of the incident beam should be sufficient to excite the highest energy level but should also be limited in order to minimize the interaction volume. It is generally considered that the energy of the incident beam should be between 1.5 and 2 times higher than the highest excitation level. In the present research, EDS measurements are performed at 12 keV as the highest line is at about 7 keV (table 3.5).

Table 3.5: Characteristic X-rays for Fe and Al in [keV]

Element	K_β	K_α	L_β	L_α
Fe	7.059	6.400	0.717	0.704
Al	-	1.487	-	-

Electron back scattered diffraction (EBSD) is a technique based on the recording of a full image of the back scattered electrons for each scanned point. This allows recording information about the crystallography of the sample. A high energy of this latter is mandatory, typically 20 keV. Incident electrons are backscattered in the sample and diffracted by the specimen on their way to the surface. Diffracted electrons form cones of intensity above the sample with large opening angle [80]. The interception of those cones with a phosphorous screen brings up flat-hyperbolic curves, so-called pseudo-Kikuchi bands, which form the EBSD pattern and are characteristic of the sample crystallography. An EBSD pattern is recorded for each pixel. Then, the indexation of each of those patterns is done by comparison with standard patterns of the candidate phases. The resulting image gives phase types, orientation and grain boundaries among others. Grain boundaries are detected by relative orientation between neighbouring pixels. A limit angle, typically 5° of disorientation between neighbours is interpreted as a grain boundary during reconstruction. For the Fe – Al system, EBSD mapping is used for phase identification. It is also the only tool able to differentiate tongues and to situate the initial position of a single tongue in *post mortem* observation by the difference in crystallographic orientation.

Dual beam is an SEM coupled with an ion column, usually Ga^+ ions to compose a so-called *dual beam platform*. Ions can be used for imaging, producing the equivalent signals than an electron source. The much larger energy transfer of ion, in comparison with the electrons, makes this tool optimal for micro or even nano machining. Ions allow thus to precisely mill the sample. It is used for the so-called *slice and view* technique and for transmission electron microscopy (TEM) sample preparation. Slice and view technique consists in imaging the sample with the electron beam and milling a slice away with the ion beam alternately. The sample is tilted such that the ion beam is perpendicular to its surface. A primary trench is milled to generate a first flat surface, which is perpendicular to the sample one and an image of it is recorded. Then a few nanometres layer is removed by ion milling and another image is recorded by SEM. The process is then repeated and images are collected as a stack that can be treated to reconstruct the milled volume. The TEM lamella extraction consists in milling two primary trenches separated by few micrometres of material, the future lamella. This section is then extracted from the bulk material and welded to a TEM grid. It is then milled until its thickness is sufficiently thin to be transparent to electrons.

3.3.4 Transmission Electron Microscopy

The general function of a transmission electron microscope (TEM) consists in recording electrons that have been transmitted through a thin sample [81]. It can be operated in different modes giving information described hereafter.

TEM observations are made mainly close to the tongue tips in order to study their internal structure. Different microscopes are used for this characterization:

- Philips CM12 at CIME and JEOL JEM2010 at PSI (Villigen, CH) for bright field (BF) imaging and diffraction patterns acquisitions.
- FEI Tecnai Osiris and Philips CM300 in STEM HAADF mode at CIME for EDS analysis
- FEI Titan stem connected at Forshungszentrum (Jülich, D) for HRSTEM HAADF observations.

Bright field imaging is the primary imaging mode in TEM, consisting in recording the image with the transmitted beam only . Contrast depends mainly on the atomic number, the sample thickness and the crystallographic orientation.

Diffraction patterns record the diffracted electrons of a selected region and give information on the phase and the crystal orientation.

EDS measurements can be done in Scanning Transmission Electron Microscopy (STEM) mode, meaning that the beam is scanned over the sample, similarly to SEM (see section 3.3.3). However, as samples are only tens of nm thin, the interaction volume is much smaller than in a SEM and thus the spatial resolution is better.

HRSTEM with high angle annular dark field detector (HAADF) consists in recording electrons diffused by the sample with an angle 50 to 150 mrad. The contrast depends essentially on atomic number, depending on the atomic mass of the atom, the so-called Z-contrast. This technique allows high resolution and it reveals atomic columns together with atomic content variation.

3.4 *In situ* observations with X ray tomography

3.4.1 X-ray tomography

X-ray tomography is a non-destructive technique that acquires projected radiographies of a sample in rotation. The two principles on which X-ray tomography is based are the Lamber-Beer law and the Radon transform [82]. The Lamber-Beer law links the attenuation of photon energy to the properties of the illuminated material while the Radon transform is the mathematical formulation of a projection. The inverse transform allows the 3D reconstruction from a set of projections recorded at different angular positions. Since different phases and materials have different absorption coefficients, coupling these two principles allows to reconstruct the 3D microstructure with an inverse absorption contrast. The resulting reconstruction will render phases similarly to BSE imaging (section 3.3). High Z elements having a higher absorption coefficient appear thus brighter than light elements. In practice, transmitted X-rays hit a scintillator, which converts them into visible light that is recorded by a CCD camera. The sample is rotated by 180° with a constant angular steps for projections acquisition.

3.4.2 Data acquisition

For the present study, X-ray absorption micro-tomography was performed on the ID15A beam line of the European Synchrotron Radiation Facility in Grenoble, France. The fast micro-tomography series are collected using a high resolution tomography set-up of ESRF [83]. The detector consists of a 25 µm thick LuAG:Ce scintillator screen. This image is magnified by a 10x mirror optics and is collected by a high-speed CCD camera, the DALSTAR Pantera 1M60. The high flux of the ID15 high energy undulator source allows to perform a 3D tomographic scan in less than 20 s. In order to get a better contrast, with the strong absorbance of Fe, a monochromatic beam at 52 keV was chosen, which imposed a slower scan of about 90 s. Additionally, the number of projections acquired during the rotation of the sample (1800, one every 0.1°), the exposure time of each projection (50 ms per projection) and the acquisition frequency of flat images, needed for background subtraction (one after every tomogram) leaded to a time resolution of 2 min for the acquisition of a complete tomogram, which is short enough to render the evolution of Fe-Al interface [84].

Experiments are carried out in a resistive furnace mounted in the ID15 line. Samples are heated to 700 °C with a temperature ramp of $1\,°\mathrm{C}\cdot\mathrm{s}^{-1}$ under a He flux of $0.4\,\mathrm{L}\cdot\mathrm{min}^{-1}$ to avoid oxidation of the iron part of the sample. The reference time is given by the first tomogram recorded once the temperature of 700 °C is reached. Although the reaction starts already during heating, the difference between the start of the experiment and the reference time does not exceed a few minutes, which is small compared to the overall reaction time. The total reconstructed volume is a cylinder 1.2 mm in diameter and height as illustrated by dashed lines in Fig. 3.4 presenting the two sample geometries. The space resolution is given by a cubic voxel size of 1.2 µm and experiments lasts approximately 4 h from reference time.

3.4.3 Samples

Two geometries are observed *in situ* , one with a vertical interface (Fig. 3.4 (a)), the second with a horizontal one (Fig. 3.4 (b)). In this figure, sketches of the reconstructed volume inside the samples is shown as a dashed cylinder. They correspond to stacks of horizontal images forming cylinders 1.2 mm in diameter and 1.2 mm in height. From those reconstructions 2D images stacks are extracted as presented in section 3.5 and are represented as a cubic volumes of 600 µm in side in Fig. 3.4. One of the 2D images is also represented in both cubes of this figure. The sample with vertical interface is produced by forcing iron cylinder of 1 mm in diameter in an aluminium tube. This tube had respective internal and external diameters of 1 and 2 mm, and a height of 6 mm. One difficulty during imaging is the eccentric position of the interface. It is not possible to follow the full evolution of the formed intermetallic layer due to its disappearance from the field of view after a certain time. The second geometry did

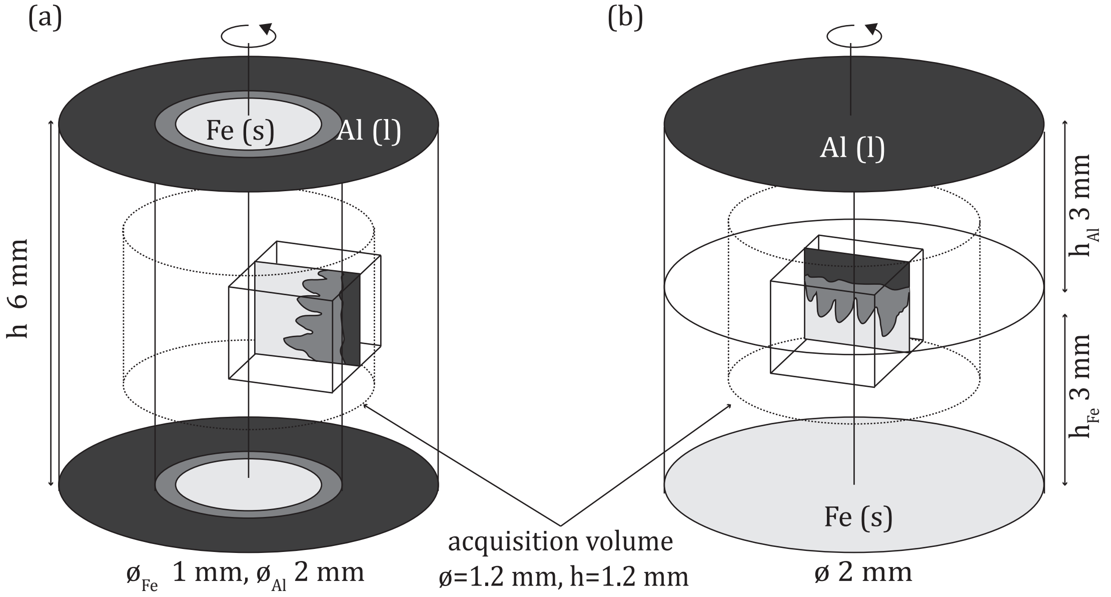

Figure 3.4: Schematics of sample geometries used for *in situ* observations. (a) Vertical interface (b) Horizontal interface. Dashed cylinders represent the reconstructed volumes, cubes the extracted and treated stacks of 2D images. One of those images is also represented in the cubes. Contrasts indicates materials: the lighter grey corresponds to Fe, the darker one to Al and intermetallics is sketched in between.

not suffer from this positioning problem. It is therefore the main source of information used for the present study. This geometry is composed of one cylinder 3 mm in height and 2 mm in diameter of Al, which is put on top of an Fe cylinder having the same dimensions. Although the native oxide layer initially surrounding the Al cylinders was resistant enough to contain the molten aluminium, an inorganic glue (Aron Ceramic D produced by Toagosei CO.,LTD, Tokyo, Japan) was applied all around the aluminium in both geometries in order to avoid any liquid leak.

3.5 Quantification

In order to quantify the intermetallic growth, SEM images and tomographic reconstructions are treated with the Fiji ImageJ open source software [79]. The automation of the phase recognition on the tomographic reconstructions is performed with the ilastik 0.5 open source software [85].

3.5.1 Image treatment

Image treatment consists in thresholding the images to separate the different phases. SEM (BSE) images are recorded with a strong contrast and thus the iron phase appears totally saturated (white) and aluminium phase fully dark. The two main intermetallic phases, namely Fe_2Al_5 and Fe_4Al_{13} are then easily thresholded. Before threshold, a median filter is used in order to facilitate the treatment. Tomography reconstruction treatment due to the large data volume was partially automated. Indeed, every two minutes, one tomogram of 1500 slices and 3.5 Go (dashed cylinder in Fig. 3.4) is recorded. Every tomogram is first pre-treated in Fiji ImageJ to extract a cubic volume 500 µm in side as shown in Fig. 3.4, applying a ROF denoise filter and changing the image dynamic range from 32-bit to 8-bit. This change is mandatory for the treatment with ilastik 0.5. The difference in density between Fe_2Al_5 and Fe_4Al_{13} is not enough to differentiate one from the other in the tomograms. The pre-treatment is automated by a macro script. The threshold is made with ilastik 0.5, which allows image classification and segmentation of arbitrary chosen classes by means of features recognition and iterative training [85]. Every tomogram is manually opened with ilastik, three classes Fe, Intermetallics and Al are chosen with two features colour and texture at large scale on the ilastik scale of five degrees from tiny to extra large. The classes are then manually marked on one image and the software predicted the same classes on the other ones, allowing threshold of the complete volume (500 images) in few minutes. The result is saved as a stack of binary images with intermetallics appearing in white and iron and aluminium in black. Post-treatment consists in opening binary stacks with Fiji-ImageJ, smoothing them by an erode / dilate operation and performing the different measurement described hereafter.

3.5.2 Equivalent thickness

The measurement of *equivalent thickness* consists in measuring the surface taken by the intermetallics on an image and dividing it by the image width. This technique is applied to SEM micrography.

3.5.3 Area fraction

The quantification of the binary image stacks obtained from the tomograms is performed through the measurement of the area fraction of intermetallics as a function of the position perpendicular to the initial interface. Fig. 3.5 presents a typical result together with the definitions of interfaces and regions. As this method was developed on a horizontal sample, the perpendicular position corresponds to the one along z axis. This denomination is also used for the other geometry. A threshold for detection of intermetallics is defined at 10 %, which corresponds to the measurement error due to the automation. Three interfaces defined by phase fraction values are used. Numbering refers to the annotations in Fig. 3.5.

1. The solid - liquid interface is defined by the mean z value between the first slice above 10% and the first above 90% when the area fraction is increasing.
2. The tongue - iron interface is defined by the first slice with a phase fraction below 10% when the intermetallics surface fraction is decreasing.

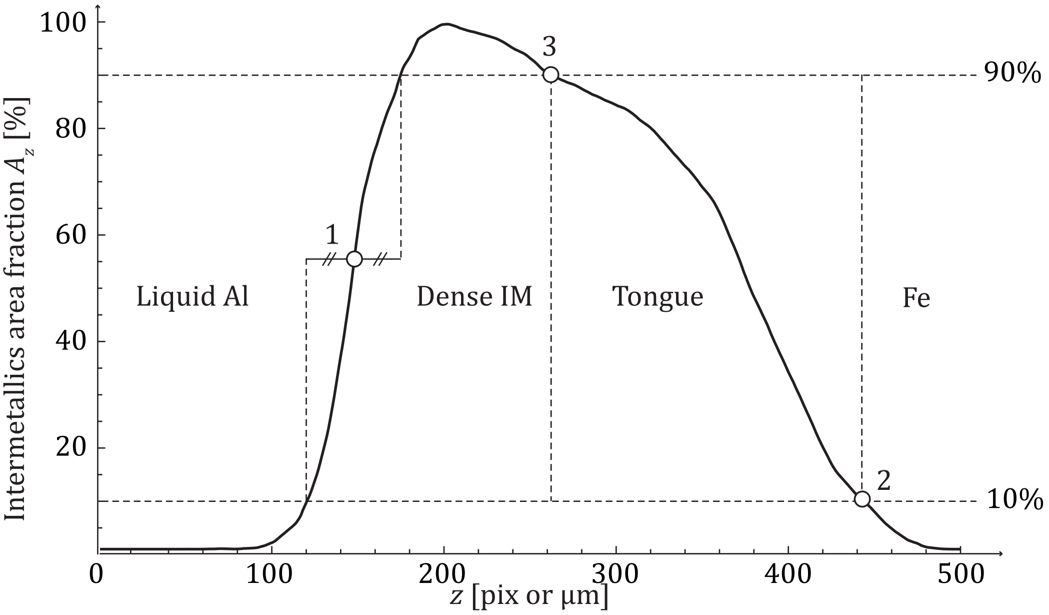

Figure 3.5: Intermetallics area fraction from the tomogram at 30 min of the sample with horizontal interface. Interface positions defined by:solid-liquid interface (1): mean z between 10 and 90 % when increasing, interface dense intermetallics - tongue (2) 90 % when decreasing, tongues - Fe (3) 10% when decreasing.

3. In addition, a limit between the dense intermetallics region and the tongues region is defined by the first slice with a fraction below 90% when the area fraction is decreasing (on the tongue side).

The measurements are performed for each tomogram (i.e. one tomogram acquired every 2 min during 4 h). When the 90% limit is not reached, as it is the case at the beginning of the reaction, the value for the interface position is replaced by the position of the maximum of the curve. Data are extracted with Fiji ImageJ and treated with Mathematica. The interfaces positions as function of time are obtained directly. The volume formed is calculated by summing the area fraction in each domains v described by the interfaces above and knowing the pixel size:

$$V_\zeta = \sum_{z_{\zeta,s}}^{z_{\zeta,e}} A_z \tag{3.2}$$

with V_ζ the volume of the domain v, $z_{\zeta,s}$ and $z_{\zeta,e}$ the first (s = start) and the last (e = end) slice within the domain ζ and A_z the measured area fraction at slice z.

3.5.4 Tongue thickening

Tongue thickening is evaluated from tomograms. The tongue domain as defined in Fig. 3.5 is isolated from the others and treated in three successive steps presented in Fig. 3.6. A *particle*

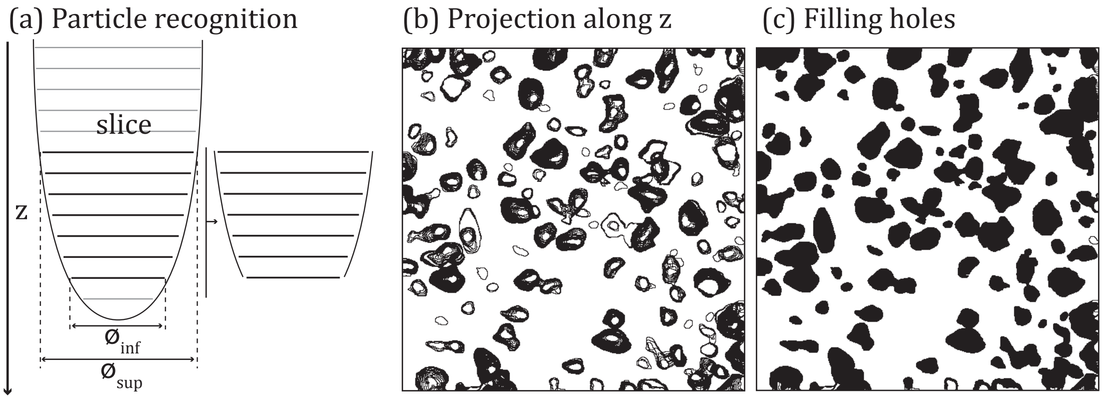

Figure 3.6: Thicknening measurement: (a) Particle recognition on each slice, (b) Projection along z, (c) Filling holes and particle analysis .

recognition algorithm is first applied on each slice, choosing a limited diameter range for the particles between $Ø_{inf}$ = 22.5 pix or 27 µm and $Ø_{sup}$ = 43.7 pix or 52.4 µm. Therefore, each tongue is only extracted in a range of slices (z direction) where it had the right diameter. This limitation allows to extract only part of each tongue situated on a middle position and thus limited tongues overlapping during projection along z Fig. 3.6 (b). Then, the mentioned projection along z is performed, giving for each tongue concentric surfaces presented in (b) that are filled to obtain single particles representing each tongues (c). Three consecutive erosions to separate the particles followed the filling. Finally, a particles measurement is performed, from which the number of tongues as a function of time is extracted. As thickening is evaluated by tongue density, the geometrical dimensions on each tongue are useless. One notices that particles on image side of Fig. 3.6 (c) are not filled due to the filling algorithm. As it is not possible to avoid this non filling, it corresponds to the main error source of the measurement as the unfilled particles are partially removed by the erode / dilate steps.

3.5.5 Saturation

Dissolution of Fe in the Al bath is evaluated on *post mortem* samples with horizontal interface. The area fraction of Fe_4Al_{13} present in the melt is measured by SEM (BSE) micrography analysis at different positions. With this fraction, it is possible to evaluate the local melt composition assuming the following assumptions:

- Solidification occurred by infinite quenching that froze the microstructure.
- No convection effect occurred in such configuration. Thus, local measurement relates the local composition before solidification.

With these assumptions and considering the eutectic part of the Fe – Al phase diagram presented in fig. 3.7, one can relate the measured Fe_4Al_{13} phase fraction to the bath saturation.

Indeed, the fraction of Fe_4Al_{13} in the eutectic is given by the lever rule and is of 3.75 %. At saturation concentration (98.2 at % of Al), if solidification occurs, the primary solidified phase Fe_4Al_{13} represents 3.89 % of the surface fraction, the rest being eutectic. Thus, a solidified saturated bath exhibits a Fe_4Al_{13} fraction given by the addition of the primary phase and the part of the eutectic that corresponds to a phase fraction of 7.64 %. It has to be mentioned that the measurement suffers from an important error due to the assumptions presented here above.

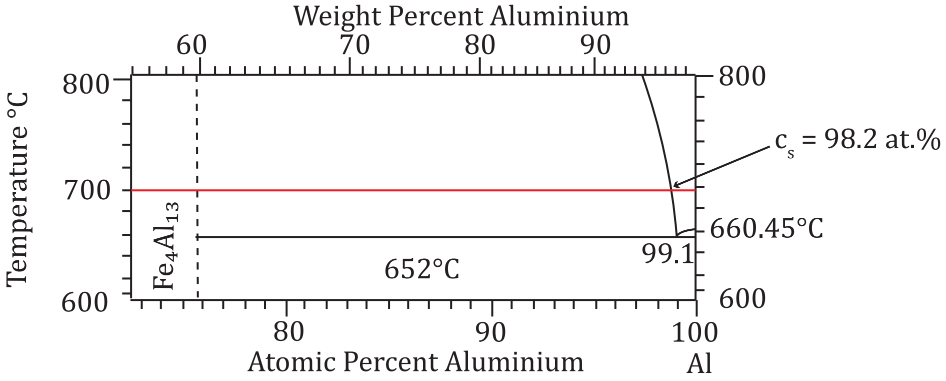

Figure 3.7: Al-rich region of the Fe – Al phase diagram [23] with a eutectic transformation at 652 °C.

Bath composition measurements are not performed on the dipping tests as bath solidification is not controlled at all and convection is important in this configuration. Indeed, as already mentioned, in addition to the natural convection involved by the vertical Fe–Al interface, the bath height of about 5 cm involved a slight temperature gradient of about $2\,°C \cdot cm^{-1}$, which also implied convection. The convection effect on the dissolution is evaluated for this test by measuring the difference of the diameter between the initial and the reacted sample. For that, the remaining intermetallic layer aluminium are dissolved in a HCl 32 % solution during 1 h. This method required producing one sample dedicated to this measurement as the intermetallics are disappearing during the chemical etching. The mass difference was also tested on those samples but the measurement precision is not sufficient to obtain a significant result.

It has to be mentioned that those semi-quantitative methods are not optimal and are only considered as indicators of the effect.

3.5.6 Quality coefficient

For the investigation of the technological relevant materials, the penetration of the intermediate phases is not homogeneous around the fingers. To render the effect of the coating, a quality coefficient is defined, taking into account the thickness of the formed compound and the fraction of the perimeter that is actually attacked by liquid aluminium. Light microscopy stitched micrographies of finger's cross-section are used for this method. Fig. 3.8 presents the measurement method. Each portion of the perimeter where the ferrous sample is attacked is identified by the angle α_i representing its chord. The quality coefficient QC is defined as follow:

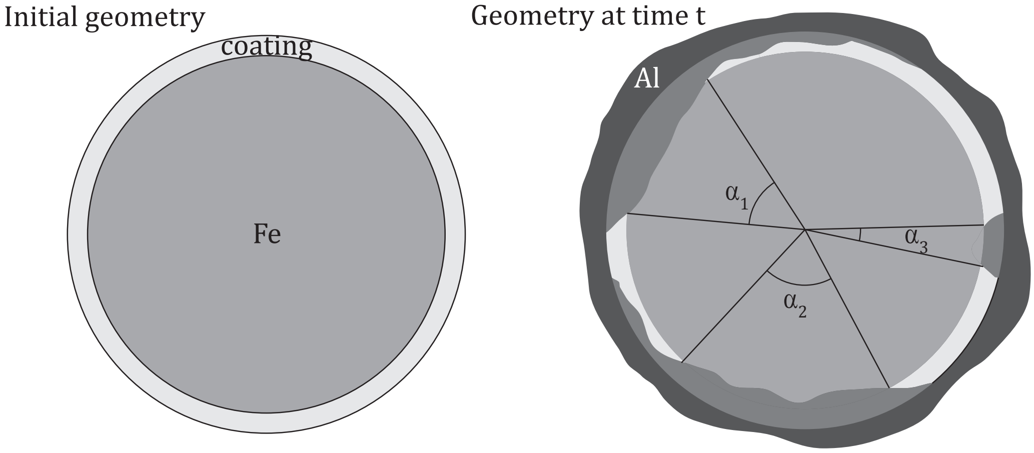

Figure 3.8: Quality coefficient definition: (a) initial cross-section with coating surrounding the ferrous sample. (b) After contact with liquid Al, attacked zones marked by portions of angle α_i.

$$QC = \frac{W}{2\pi}\sum_{i}^{N}\alpha_i \qquad [\mathrm{m}] \tag{3.3}$$

with W the equivalent thickness of the formed compound. Thus, for sample without coatings, the reaction is homogeneous all around the sample and the quality coefficient is equal to the measured intermetallic thickness W. In the case of partially attacked sample, the latter is weighted by the fraction of the attacked surface.

3.6 Numerical modelling

A one dimension numerical model was developed by Léa Deillon [16] to reproduce interfaces' movements in the multi phases Au-In system by finite differences method. In this work, the code is modified for the Fe-Al system and is described in the following sections.

3.6.1 Hypothesis

As the aim of the numerical model was to calculate values used in the analytical model of chapter 6, which considers the growth of one single intermetallic phase at the interface between iron and aluminium, the following assumptions have been made:

1. The initial system is formed of pure iron and pure aluminium domains separated by a thin layer of intermetallics.
2. Nucleation steps are not taken into account.
3. Al diffusion only is considered.
4. Only Fe_2Al_5 growth is taken into account, as Fe_4Al_{13} has a constant thickness regardless of the test and is considered as part of the intermetallics, FeAl is considered as a transition layer included in the initial matrix and $FeAl_2$ appears only in particular cases (see section 4.2).
5. Kirkendall effect is not introduced in the calculation.
6. Interfaces are at equilibrium.
7. The Al melt is saturated with Fe.
8. Chemical potentials vary linearly in the intermetallics.

The saturation step as it will be shown, can be neglected for *in situ* measurements as the volumes involved materials are sufficiently small for the bath to saturate rapidly. The linear variation of the chemical potential is justified by the fact that concentration and atomic mobility are supposed to be constant. thus it implies second Fick's law:

$$\frac{\partial C(x,t)}{\partial t} = -\frac{\partial J}{\partial x} = MC\frac{\partial^2 \mu}{\partial x^2} = 0 \tag{3.4}$$

3.6.2 Thermodynamic parameters

The thermodynamic data presented in section 2.5.1 are used to determine chemical potentials and Al atomic fraction equilibrium values at the interfaces. Profiles are schematically presented in Fig. 3.9 with values at 700 °C. A secondary module of the model calculates the chemical potentials and the interfaces concentration as a function of the temperature. Once those parameters are known, they are introduced in the main code.

3.6.3 Discretisation

Second Fick's law given in Equ. 2.5 is solved for the iron domain in a centred explicit scheme. It is solved under the following form for each node in the Fe domain and at each time:

$$\frac{c_i^{t+\Delta t} - c_i^t}{\Delta t} = D_{Al}^{Fe}\frac{c_{i+1}^t - 2c_i^t + c_{i-1}^t}{h^2} \tag{3.5}$$

with c_i^t the concentration of the node i at time t, Δt the time step and h the space step.

Space discretisation: The mesh consists in 1020 nodes distributed in the different phases as described in Fig. 3.9. In addition, this schematics gives the interfaces position x_i^*, the interfaces node names and the chemical μ_i potentials and atomic fractions X_i profiles. Most of the nodes are located in the Fe domain in order to precisely describe the Al profile during growth. Furthermore, as diffusion of Al in Fe is really low, the space step h should be as small as possible, while limiting calculation time. As indicator, a rough estimation of the Peclet number, which should be smaller than 2 in order to obtain a stable solution, is done using Equ. 3.6.

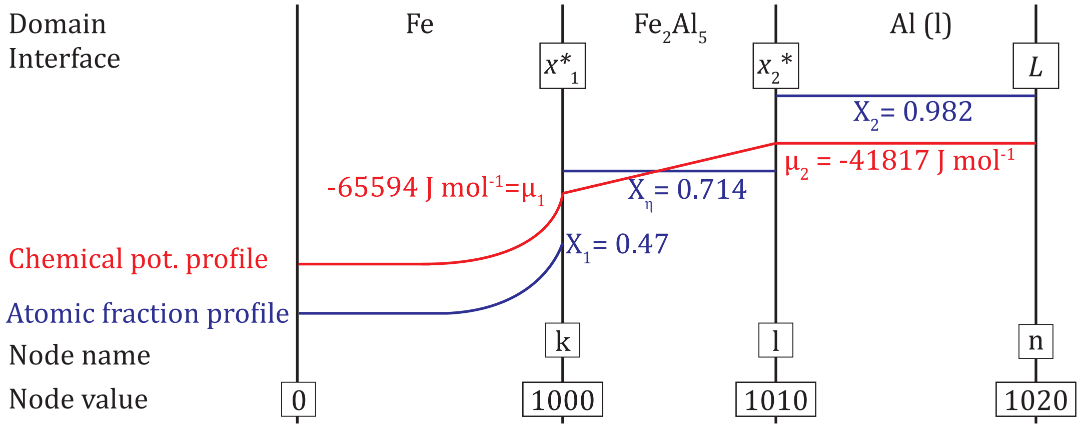

Figure 3.9: Discretisation description: domain names, interface names node names and node values at interfaces.

$$2 \geq Pe = \frac{vh}{D_{Al}^{Fe}} \approx \frac{10^{-8}\,h}{3\times 10^{-17}} \approx h \times 10^{9} \tag{3.6}$$

This calculation shows that a stable solution of the concentration profile is obtained when the space step is in the order of the nanometre. To limit calculation time, it was decided to not increase the node number in the iron but to fix its thickness of 2 µm in front of the interface with an infinite supply at the node 0. In other words, the observed iron domain consists in the close region near the interface where the Al concentration strongly varies. This implies that the first interface does not reach the domain limit. The latter is thus artificially immobile and used as referential in order to calculate movements of the other interfaces. This technique allows to precisely describe the profile while consuming less calculation time. Interface x_2^* is placed on node l=1010. L representing the Al side is placed on node n= 1020.

Time discretisation: The convergence of the explicit resolution is also dependent on the time step. The stability criterion is given by the Fourier number Fo defined in Equ. 3.7. For the Fe domain it gives:

$$\frac{1}{2} \geq Fo = \frac{D\Delta t}{h^2} \approx \frac{3\times 10^{-17}\Delta t}{4\times 10^{-18}} \approx 10 \times \Delta t \tag{3.7}$$

With this information, the time step was chosen as 0.01 s to ensure stability

3.6.4 Conditions

Boundary conditions: They are of Neumann homogeneous type on the Al domain sides (flux null) and Dirichlet type at interfaces (fixed chemical potentials and concentrations).

Initial conditions: They concern the initial domain sizes and the atomic fractions. The iron domain size, as already mentioned is fixed to 2 µm and moves with the interface. The Al domain size is fixed to 5 mm to insure that Al is not fully consumed. Initial domain for intermetallic compound is of 1 µm. Atomic fractions are listed here as function of the node position

- in Fe, for $0 < i <$ k : $X_i = 0$
- in Fe at the interface with Fe_2Al_5, for i = k: $X_\mathrm{k} = 0.471$
- in Fe_2Al_5, for k $< i <$ l+1: $X_i = 5/7$
- in Al at the interface with Fe_2Al_5, for i = l+1: $X_\mathrm{m+1} = 0.982$
- in Al for l+1 $< i <$ n+1: $X_i = 0.982$

Al concentration c in at/m^3 is determined from the atomic fraction X by taking into account the molar mass, $\mathscr{M}^v$ and the density, ρ^v of each phases v according to Equ. 3.8

$$c = \frac{X \times N_a \times \rho^v}{\mathscr{M}^v} \tag{3.8}$$

3.6.5 Flux and interface velocity

The flux in the aluminium bath is considered as null by hypothesis as it is saturated in iron. In intermetallic phase, as chemical potential gradient is supposed to be linear, fluxes are evaluated by Equ. 2.2 as follow:

$$J = -Mc\frac{\Delta\mu}{\Delta x} \tag{3.9}$$

where $\Delta\mu$ is the difference between the chemical potentials of Al at each interface and Δx the thickness of the intermetallics. The flux in iron is given by Fick's first law (Equ. 2.3) and is expressed as follow:

$$J^{Fe} = -D^{Fe}\frac{c_i - c_{i-1}}{h} \tag{3.10}$$

with h the fixed space step in the iron domain.

Balance equations [22]

Mass conservation is given by its general form:

$$\frac{\partial \rho}{\partial t} + \nabla(\rho \vec{v}) = 0 \tag{3.11}$$

Applied to the case of an interface between two phases α and β it gives:

$$(\rho^{\alpha} - \rho^{\beta})\vec{v^*} \cdot \vec{n} = \rho^{\beta} \vec{v^*_{\beta}} \cdot \vec{n} - \rho^{\alpha} \vec{v^*_{\alpha}} \cdot \vec{n} \tag{3.12}$$

where $\vec{v^*}$ is the interface velocity and $\vec{v^*_{\alpha}}$ and $\vec{v^*_{\beta}}$ are phase velocities at the interface. Solute balance is given in its general form by:

$$\frac{\partial \rho C}{\partial t} + \nabla \cdot (\rho C \vec{v}) = -\nabla \vec{j} \tag{3.13}$$

with C the weight fraction of Al and $\vec{j}$ the mass flux of Al in g· m^2·s^{-1} . Applied to the same interface, one obtains:

$$\rho^{\beta} C^*_{\beta} (\vec{v^*_{\beta}} - \vec{v^*}) \cdot \vec{n} - \rho^{\alpha} C^*_{\alpha} (\vec{v^*_{\alpha}} - \vec{v^*}) \cdot \vec{n} = -\nabla \vec{j} \tag{3.14}$$

Fixing the velocity of the iron phase v_{α} to zero, it is possible to determine interface velocities with Equs.3.12 and 3.14. In order to simplify the notation, letters are used here for phases with α, η and L for iron, Fe_2Al_5, and liquid aluminium respectively. Numbers are given for interfaces, with 1 for Fe/Fe_2Al_5, and 3 for Fe_2Al_5 /aluminium interfaces.

$$v_{\alpha} = 0 \tag{3.15}$$

$$v^*_1 = \frac{j^{\eta} - j^{\alpha}}{\rho^{\alpha} \cdot (C_{\eta} - C^*_{\alpha})} \tag{3.16}$$

$$v_{\eta} = v^*_1 \left(1 - \frac{\rho^{\eta}}{\rho^{\alpha}}\right) \tag{3.17}$$

$$v^*_2 = \frac{-j^{\eta}}{\rho^{\eta}(C_L - C_{\eta})} + v_{\eta} \tag{3.18}$$

$$v_L = \frac{v^*_3(\rho^L - \rho^{\eta}) + \rho^{\eta} v_{\eta}}{\rho^L} \tag{3.19}$$

The new interface positions are then calculated from the initial one and the displacement is obtained as the time increment multiplied by the velocity. But as the x^*_1 interface is artificially kept immobile, $\Delta t \times v^*_1$ is subtracted to all other positions. Updated position have thus the following forms:

$$x_1^{*t+1} = 0 \tag{3.20}$$
$$x_2^{*t+1} = x_2^{*t} + \Delta t(v_2^{*t} - v_1^{*t}) \tag{3.21}$$
$$L^{*t+1} = L^{*t} + \Delta t(v_L^t - v_1^{*t}) \tag{3.22}$$
$$\tag{3.23}$$

This calculation allows then to follow the position of the interfaces as a function of time.

3.6.6 Densities

Change in volume due to density differences are taken into account in the model. The theoretical density as a function of temperature and of Al atomic fraction is given by:

$$\rho^{\alpha}(X_{Al}, T) = \frac{2\,(X_{Al}\mathscr{M}_{Al} + (1 - X_{Al})\mathscr{M}_{Fe})}{N_a V^{\alpha}(T)} \qquad [kg \cdot m^3] \tag{3.24}$$

The factor 2 is due to the presence of two atoms in the unit cell of the *bcc* structure of α-iron. $V^{\alpha}(T)$ is the volume of this unit cell, which could also be influenced by the presence of Al atoms. This aspect is neglected, as atomic radii are similar, thus inducing a negligible change in structure size. Liquid Al density as function of the temperature is given as follow [3]:

$$\rho^{L}(T) = 2385 - 0.35(T - T_m) \qquad [kg \cdot m^3] \tag{3.25}$$

Concerning the intermetallic compounds, no information on the thermal dependence of their physical properties was found. Densities are thus estimated from their crystallographic structure as presented in table 2.4.

4 Intermetallic compounds

This chapter describes the interface between liquid aluminium and solid iron after reaction. Fig. 4.1 (a) presents a cross-section of a pure iron finger that was dipped into liquid aluminium during 90 min at 700 °C . The cross-section is situated at 10 mm from the immersed tip of the finger. It was chemically etched to reveal the iron microstructure. Besides the iron and some solidified aluminium stuck on the surface, one can observe a darker ring that corresponds to intermetallics formed during the reaction. Fig. 4.1 (b) presents a SEM micrography in BSE mode revealing the intermetallics layer that forms between the iron matrix and the liquid

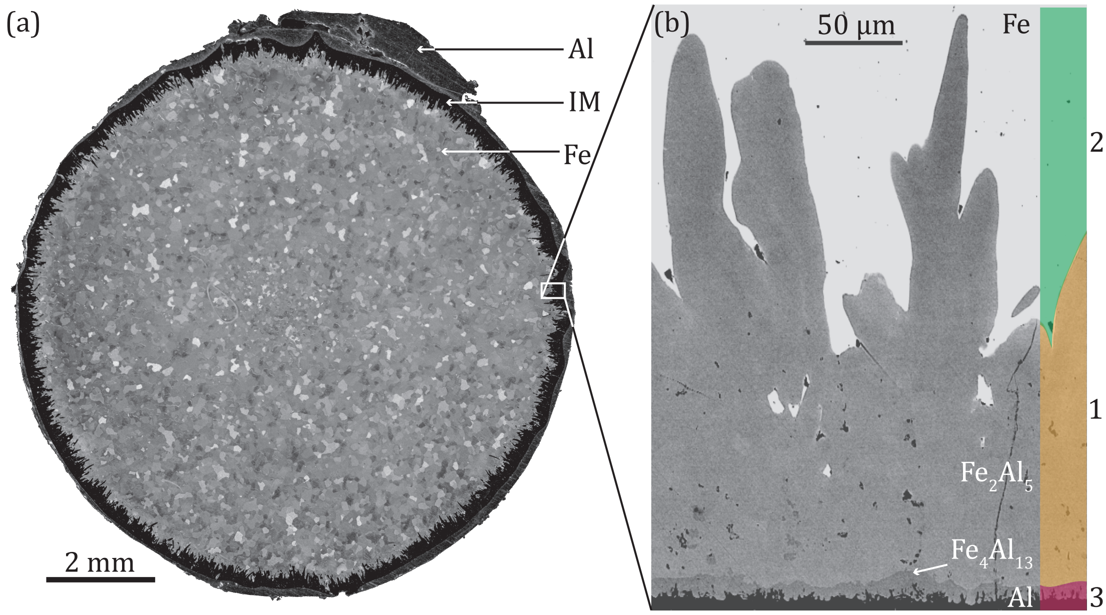

Figure 4.1: (a) LM micrography reconstruction: cross-section of an Fe sample dipped in liquid Al during 90 min at 700 °C. (b) SEM (BSE) micrography at higher magnification revealing (1) the intermetallic layer in grey between, (2) the iron matrix in light grey Fe and (3) the remaining Al in black. They make the three regions of interest treated in this chapter.

aluminium. Three regions of interest represented by coloured regions 1, 2 and 3 in Fig. 4.1 (b) are thus defined as follow:

Region 1 The main intermetallic phase, namely Fe_2Al_5 with its particular *tongue-like* feature is investigated from grain size down to the lattice structure.

Region 2 The iron matrix and especially the surrounding of the Fe_2Al_5 tongues is then investigated. It reveals the appearance of FeAl and $FeAl_2$, matrix deformation and porosity formation, related to the tongue growth.

Region 3 The interface on the liquid aluminium side, including a thin Fe_4Al_{13} layer reveals the dissolution of the formed compounds in the Al bath.

4.1 Main intermetallic phase Fe_2Al_5

4.1.1 Phase morphology

The peculiar tongue-like shape of the Fe_2Al_5 phase is revealed in Fig. 4.2 (a) showing part of a dipped Fe finger that was cut along its axis and chemically etched to remove the Fe as explained in section 3.3. Iron is only partially dissolved with some remainings at the bottom of the image in Fig. 4.2 (a). Tongues emerge from its surface. The observed ones are in between the remaining iron and the cut surface. Fig.4.2 (c) presents a view at higher magnification of a region with different tongues behaviours.

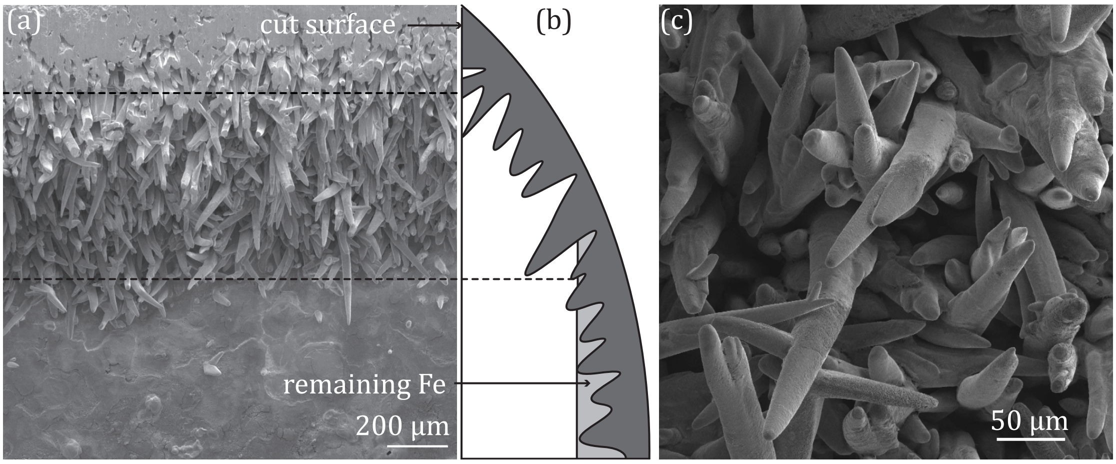

Figure 4.2: Fe finger dipped into Al during 90 min at 700 °C, longitudinally cut and chemically etched to dissolve iron. (a) SEM (SE) micrography of the remaining intermetallics. (b) Schematics of the corresponding etched specimen shown here sideways. (c) SEM (SE) micrography at higher magnification of the tongues revealed by iron etching.

Tongues appear as sharp cones, with an orientation close to the normal of the interface, for all tongues. Some tongues appear to be split into 2 or more tongues. More in detail, an analogy with solidification, considering each tongue as a dendrite tip, although the present reaction occurs at solid state, allows to observe two similar behaviours, namely (1) tip splitting and (2) secondary arms formation. However, while dendritic solidification proceeds by competition between dendrites, favoured when aligned along the thermal gradient, here tongue growth does not seem to happen similarly. Although the general growth direction is perpendicular to the initial surface, tongues seem to undergo several reorientations. Instead of stopping its growth when meeting an obstacle, a single tongue seems to bypass it. Seemingly a complex and random structure is resulting from this interaction. Nevertheless, EBSD mapping of a cross-section, as the one presented in Fig. 4.3 (c), shows a certain texture within the tongues. Fig. 4.3 presents three different visualisation modes of the EBSD mapping as follow:

(a) Phase reconstruction, gives phases that were indexed during acquisition and colour coded with namely yellow for Fe, blue for Fe_2Al_5 and red for Fe_4Al_{13}.

(b) Arbitrary reconstruction, gives manually coloured tongues from observation of micrography (c) to distinguish the tongues of interest.

(c) Euler 1 reconstruction, gives the grain orientation as a function of the first Euler angle of the grain, its disorientation with respect to vertical axis in the observation plane.

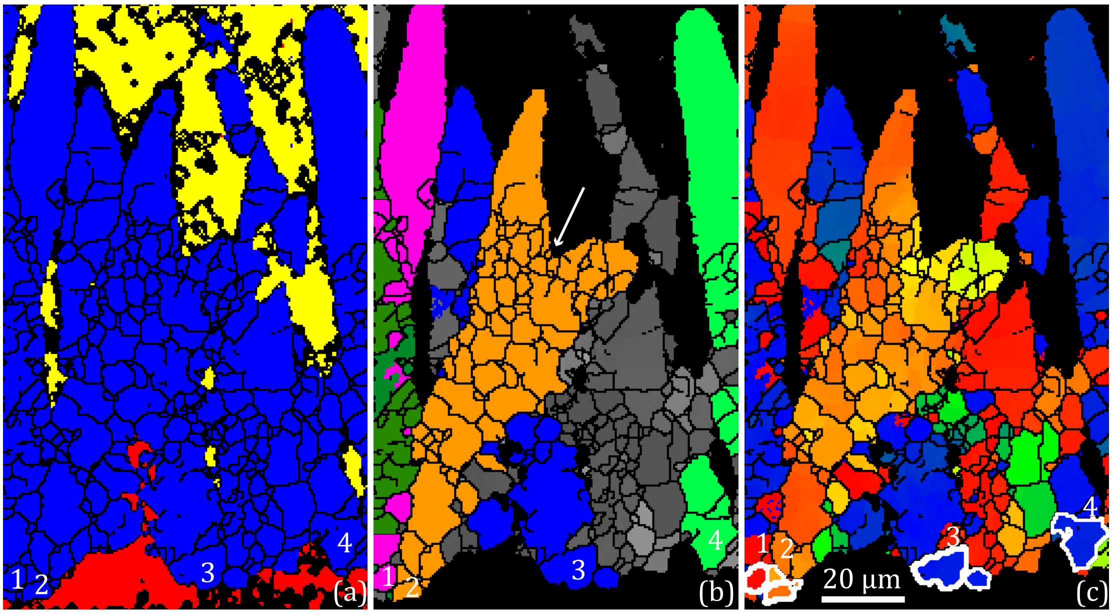

Figure 4.3: Fe_2Al_5 intermetallic phase formed in Fe finger dipped into Al during 15 min at 700 °C. EBSD maps with colours representing (a) phase (b) arbitrary colouring to distinguish tongues of interest (c) orientation according to the Euler 1 angle.

In these views, sub-grain boundaries in the Fe_2Al_5 phase delineated by black lines are identified by disorientation larger than 5°. On can observe four main tongues denoted from 1 to 4. It appears that grain orientation does not significantly change along the tongue (Fig. 4.3 (c)). It seems that a single crystalline grain is at the origin of each of the four tongues. They are tentatively outlined in white at the bottom of Fig. 4.3 (c)) . Furthermore, the following observation are made with colours referring to Fig. 4.3 (b):

1. The pink tongue (1), which is hidden in the left of the field of view by a green one presents a high homogeneity of its top part above the green tongue indicating a single crystal structure. This is also the case for the tip of tongues 2, 3 and 4.
2. The orange tongue (2) starts in the bottom left of the image exhibits secondary arm formation (white arrow) with a sharp tip growing vertically while a second one grows at about 45° toward the right.
3. The blue tongue (3) being at the beginning in the same plane as the orange one (2) re-emerges a bit further, as it bypasses the orange one by passing under or over it.
4. The green tongue (4) seems to be almost not disturbed by other ones during growth. It results in a regular orientation or no variation in Euler angles and no misorientation higher than 5° in the upper part of the tongue.

4.1.2 Phase structure

Fig. 4.4 shows the TEM analysis of an Fe_2Al_5 tongue in a FIB (Focused Ion Beam) lamella extracted across a tongue tip.

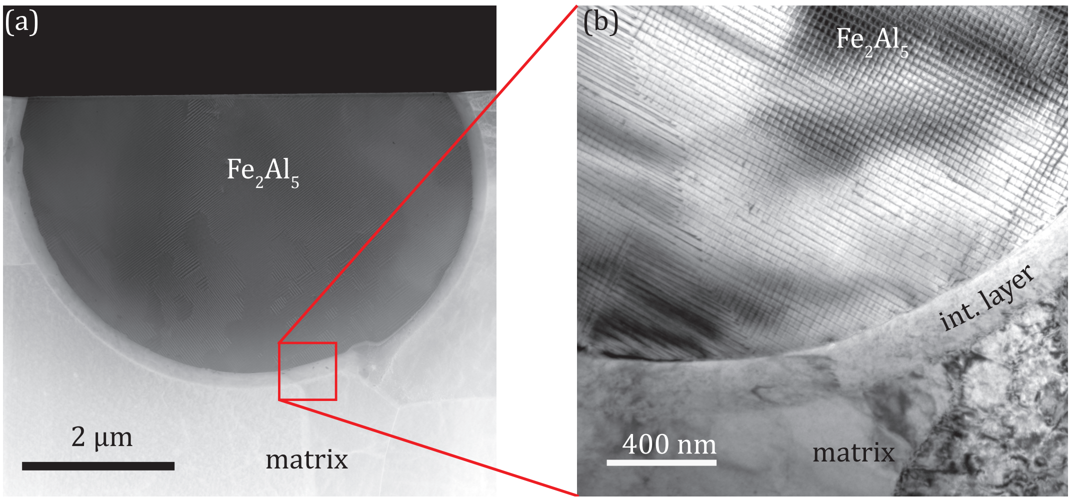

Figure 4.4: Fe_2Al_5 tongue in Fe finger dipped into Al during 15 min at 700 °C. (a) DF-STEM micrography showing the tongue section in grey in the Fe matrix in light grey. (b)TEM (BF) micrography revealing the Fe_2Al_5 phase with a periodic pattern, the deformation in the Fe matrix and a thin layer of intermediate phase between the two.

The STEM micrography in Fig. 4.4 presents the whole lamella with the tongue in dark grey in the middle, surrounded by the iron matrix. A thin layer between the tongue and the iron is seen. The upper part of the tongue was removed by mechanical polishing before the FIB preparation explaining its truncated ellipse geometry in the top. The TEM (BF) micrography presented in Fig. 4.4 (b) exhibits contrasts forming nano squares and lines. The long-range bright contrast in the tongue section is due to the bending of the lamella, which results from stress relaxation during its preparation.

The patterned structure in Fe_2Al_5 may have various origins, such as nano-twinning or local chemical variation. Fig. 4.5 (a) presents a view at higher magnification of this nanostructure in STEM BF contrast. One can remark regions with single lines (white insert) and regions with periodic lines crossing at 90°, forming squares. Focusing on a region with parallel lines in order to simplify the investigation, a STEM HAADF micrography was acquired and is presented in Fig. 4.5 (b). This image shows atomic columns in the lines. A magnified view, filtered by selecting spots in the Fourier transform of this image in a region with two adjacent lines (black insert) is presented in Fig. 4.5 (c). In this image, contrast is inverted with atomic columns appearing white in darker lines. Red and green dots are coloured atomic columns showing two directions that define each domains. Despite long range oscillations it appears that the lines are crossing the domain boundary without a change in orientation, indicating that it can't be a twin boundary.

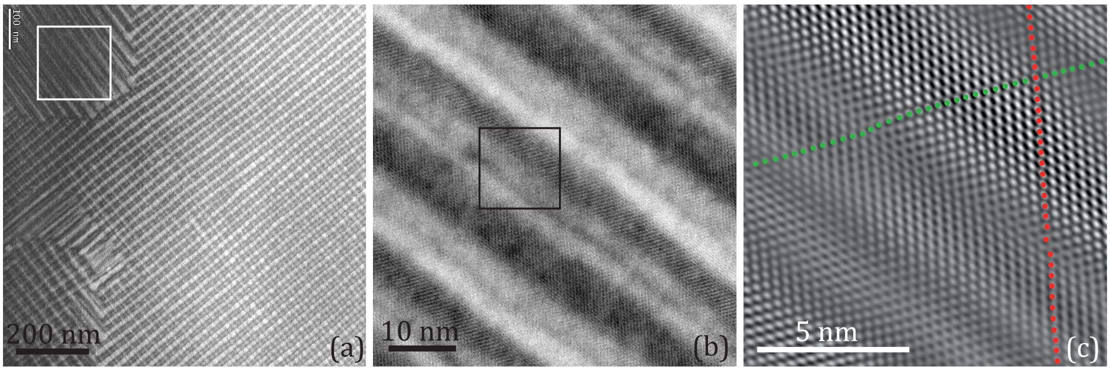

Figure 4.5: Fe_2Al_5 tongue nanostructure observation: (a) STEM BF contrast revealing the periodic nano lines and squares (b) STEM HAADF micrography of insert in (a). (c) Filtered and magnified view of micrography insert in (b).

Fig. 4.6 (a) shows a STEM HAADF micrography of lines in Fe_2Al_5 with its Z-contrast profile across the lines in (b). The position of the Z-contrast profile is indicated by the white line in the upper part of image (a). In addition a profile of quantified chemical composition made across the lines using X-ray EDS at the same position than the Z-contrast profile is presented in Fig. 4.6 (c).

Z-contrast profile is arbitrary thresholded at 130 (on the 255 scale for an 8 bit image). This

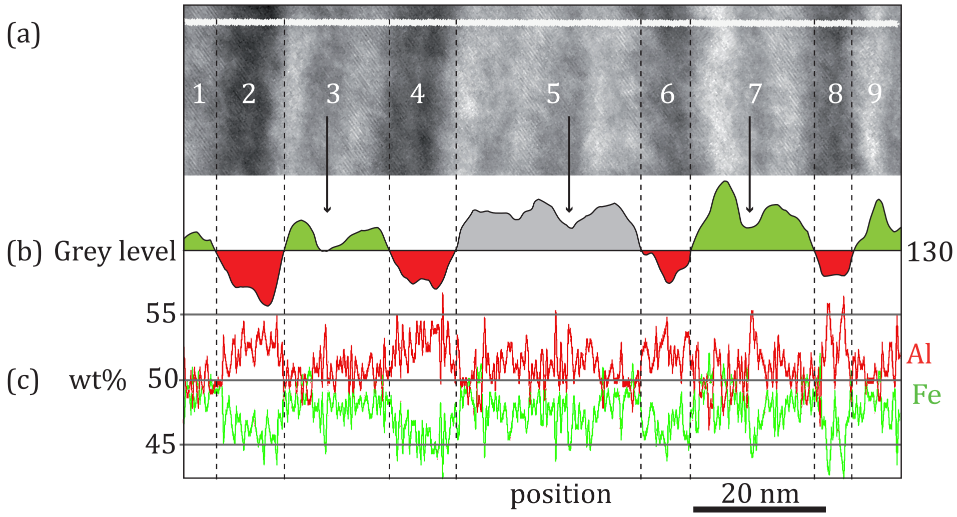

Figure 4.6: Nano structure of the Fe_2Al_5 tongue of Fig. 4.5 (a) contrast in HAADF imaging and its intensity profile in (b). (c) Weight percent profile across the nano structure observed in the Fe_2Al_5 tongue obtained by X-ray EDS.

makes appear four main darker regions, given by even numbers (2, 4, 6, 8) from left to right in image (a). The complement to 130 for these regions is coloured in red in the grey scale profile (b). The lighter regions in between are given by odd numbers (1, 3, 5, 7, 9) and their contrast profile is filled in green. One notices local minima in regions 3, 5 and 7, which are marked by arrows. Regions 5 is not clearly identified as being a lighter or a darker line. Lines 3 and 7 are interpreted as including a darker line in between two lighter ones, which is missed due to the threshold.

The EDS profiles in Fig. 4.6 (c) give Al and Fe contents in red and green respectively. Rapid oscillations in the profiles are due to the measurement precision. However, a general behaviour can be identified. One notices that in even regions Al content slightly increases compared to the odd regions. It is visible in regions 2 and 4 with the increase of the distance between the red and the green lines. Smaller regions such as 6 and 8 are less obvious due to these measurement rapid oscillations. Thus, chemical variation may indeed be responsible for this contrast in HAADF.

The range of values obtained by EDS for the Al content goes from 49 to 55 wt%. It is coloured in red in Fig. 4.7 that presents the Al-rich part of the phase diagram. The EDS measurement is covering a wide range of the phase diagram, including Fe_2Al_5 and $FeAl_2$ phases. In order to control the obtained domain, a diffraction pattern was recorded from a selected region in the middle of the tongue. Fig.4.8 presents this pattern in (a) and indexations along ⟨100⟩ direction with the Fe_2Al_5 structure in (b) and with the $FeAl_2$ structure in (c). One remarks that the indexation with the Fe_2Al_5 structure along ⟨100⟩ perfectly fits the pattern while the one with $FeAl_2$ structure does not. Note that the indexation was performed with an error margin

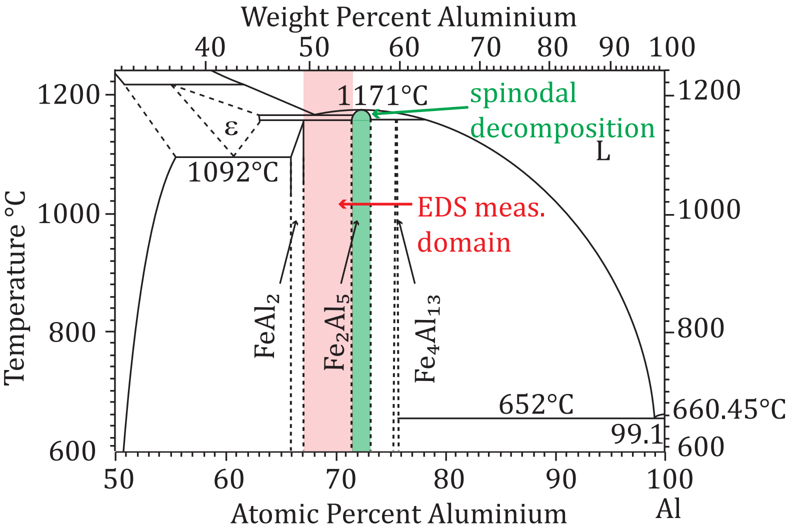

Figure 4.7: Al-rich region of the Fe-Al phase diagram with domain of the EDS measurement coloured in red.

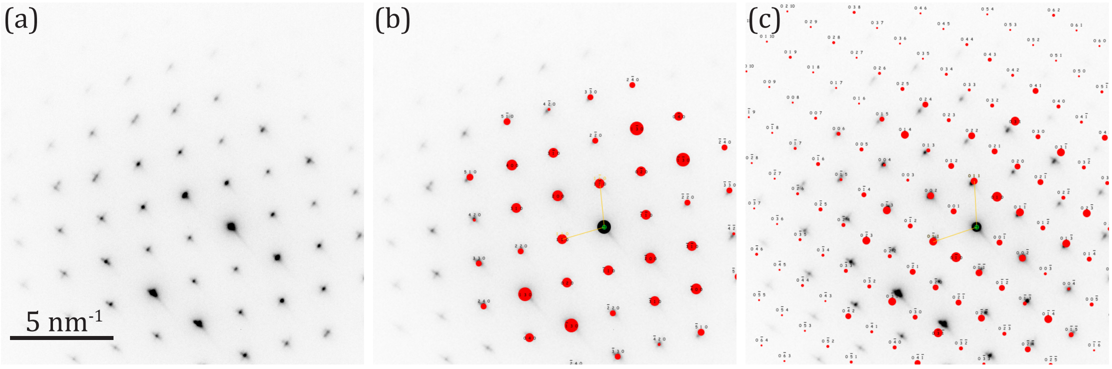

Figure 4.8: (a) TEM diffraction pattern of a selected region in the tongue with (b) spot indexation with the Fe_2Al_5 structure along [1 0 0] direction (c) spot indexation with the $FeAl_2$ structure along [1 0 0] direction.

of 10 % in angle and in distance. The presented one in Fig. 4.8 (c) is the best found and does not correspond to the structure. As the crystallographic structures of both phases have clear different parameters (see section 2.5.2) one should at least see spots from the $FeAl_2$ structure in this pattern, which is obviously not the case. One can conclude that there is no $FeAl_2$ in the tongue and that the EDS measurement presents a large error in this quantification.

This result is thus more in agreement with Lapin *et al.* [86] who interpreted the contrast as two different phases than with Hirose *et al.* [70] with the twin interpretation. However, one difference with Lapin's result is that we do not observe any $FeAl_2$ in the present system while he observed the co-presence of $FeAl_2$ and FeAl. As his TEM observations were performed on samples produced by squeeze infiltration, it may lead to a different reaction resulting in Fe-rich phases such as FeAl and $FeAl_2$. Thus his observation seems to comes from a system different than the one studied here.

Another explanation comes from the existence domain of Fe_2Al_5. Indeed, although this phase is usually considered as stoichiometric, the phase diagram proposes a thin domain between 54.5 to 56 wt %, which is shown in green in Fig. 4.7. It has to be noticed that the use of dashed lines in the phases diagram suggests that domains are still not fully defined. However, the proposed existence domain may also be responsible for the chemical variation. Furthermore, this domain exhibits a spinodal decomposition at higher temperature. It is marked by a green arrow in Fig. 4.7, which could be linked to a chemical arrangement and thus to the observed contrast and the slight chemical variations.

4.2 Interface with solid Fe

4.2.1 Transition layer

As mentioned in section 4.1.2, TEM observations reveal the presence of a thin layer between the tongues and the Fe matrix. Fig. 4.9 (a) shows a BF micrography exhibiting the deformed Fe

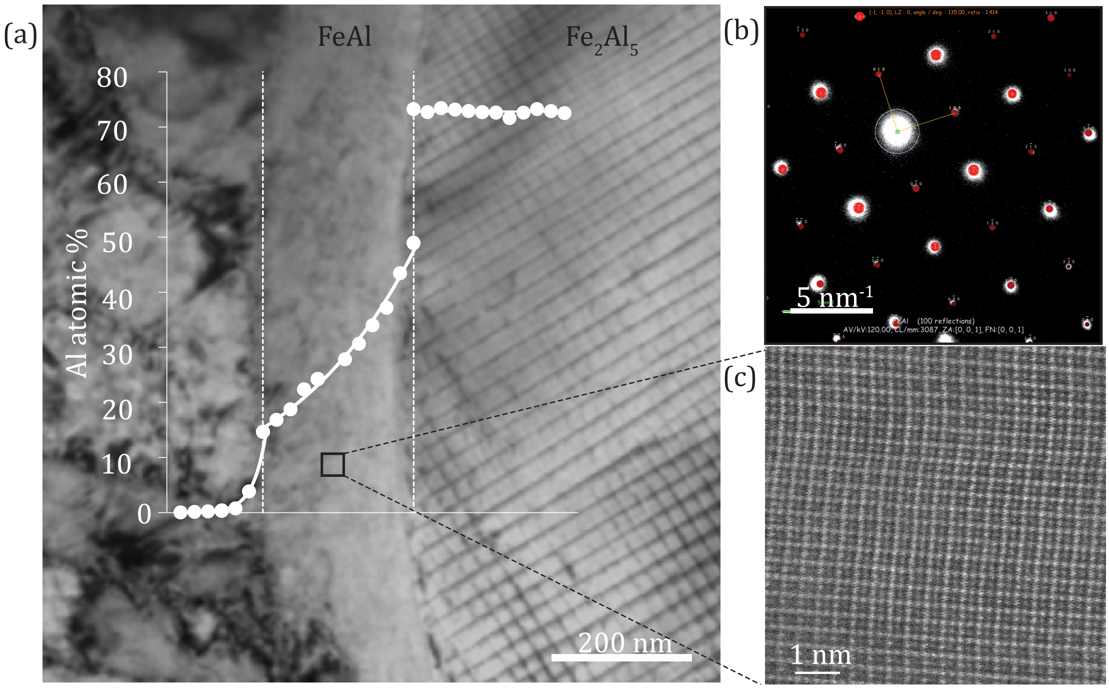

Figure 4.9: TEM of Fe sample dipped 90 min at 700 °C into Al. (a) TEM BF micrography showing the phase between the Fe matrix in the left and a Fe_2Al_5 tongue in the right, with the Al content profile across it obtained by X-ray EDS. (b) SADP image obtained in the phase and its (c) HAADF STEM micrography.

matrix in the left, the patterned Fe_2Al_5 and the phase in between, with a nearly homogeneous contrast. The chemical profile in Fig. 4.9 (a) made with X-ray EDS shows that the content in Al in the Fe matrix is constant till the interface. It has to be mentioned here that EDS measurement were performed with another microscope than in section 4.1.2 and at lower magnification. The measurement is more precise in this case. It starts to rise in a region about 20 nm before the interface. The Al content presents a steep rise across the inter-phase, indicative of a phase with a wide existence domain in the phase diagram. It corresponds to FeAl. When it reaches the interface with Fe_2Al_5, it presents a large step of more than 20 at % to reach the content in Al of Fe_2Al_5. This indicates a first order phase transition. In Fe_2Al_5 the Al content is constant at this scale (see previous section).

In addition, a selected area diffraction pattern taken in the transition layer is presented together with a HRSTEM observation of the layer in Fig. 4.9 (b) and (c) respectively. The diffraction pattern (b) as well as the regular BCC-B2 crystallographic structure observed by STEM (c) both confirm that the phase forming this layer is FeAl. The slight deformation of the lattice observed in micrography (c) is due to sample drift during the scanning.

A FIB 3D reconstruction of the layer confirms its presence all around the tongue as presented in Fig. 4.10. This reconstruction was made on an Fe sample dipped during 90 min at 700 °C. The ion milling steps used for this reconstruction was large with regards to the layer thickness at approximatively 1 μm for this sample explaining that the layer appears as separated lines. After thresholding of the phases, only the FeAl was reconstructed. One can also remark a line following on the iron side of the FeAl reconstructed surface. It corresponds, to an iron grain boundary. FeAl forms preferentially on these kind of defects due to the increased diffusion in

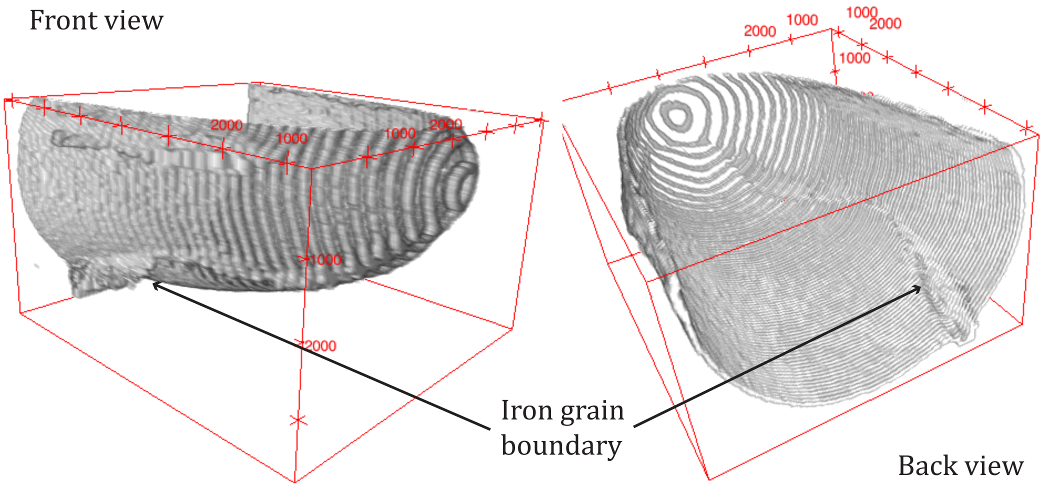

Figure 4.10: TEM of Fe sample dipped into Al for 90 min at 700 °C. 3D reconstruction SEM (SE) micrography obtained by FIB slice and view technique of the FeAl layer surrounding the tongue.

those locations (see section 2.1).

This thin FeAl layer can be considered more as a transition region between the Fe and Fe_2Al_5 phases with atomic rearrangement than as a phase transformation with global atomic rearrangement as the crystallographic structure is related to the initial iron structure. Indeed, its BCC-B2 structure, while ordered, remains centred cubic and the cell parameters are close to each other, 2.869 Å for pure Fe to 2.91 Å for FeAl. Subsequently, for the modelling this layer will be considered as included in the concentration profile in front of the Fe_2Al_5 intermetallic front instead of being treated separately from the iron matrix.

4.2.2 $FeAl_2$ phase

Cheng *et al.* [47] showed by EBSD observations that in the case of a reactive diffusion bonding, when the aluminium is fully consumed, $FeAl_2$ appears in tongue tips and grows from those ones in the opposite direction. The occurrence of $FeAl_2$ seems thus related to the full consumption of the external Al supply. Although the present study uses a larger volume of liquid that is never fully consumed (see section 5.3), it happened at times that the sample was only partially covered with aluminium after the dipping test. The uncovered regions were exhibiting an intact iron surface that seemed not having reacted. For such samples, the SEM investigation highlighted presence of $FeAl_2$ locally as seen in Fig. 4.11.

In this case part of the surface only react with liquid aluminium. Fig. 4.11(a) shows one regions with on the middle a small part that reacted and intermetallics formed (arrow). On the rest of the surface, no reaction occurred. One also notices that only little Al remains in this region forming with intermetallics blocks that are somehow detached from the iron sample (arrow).

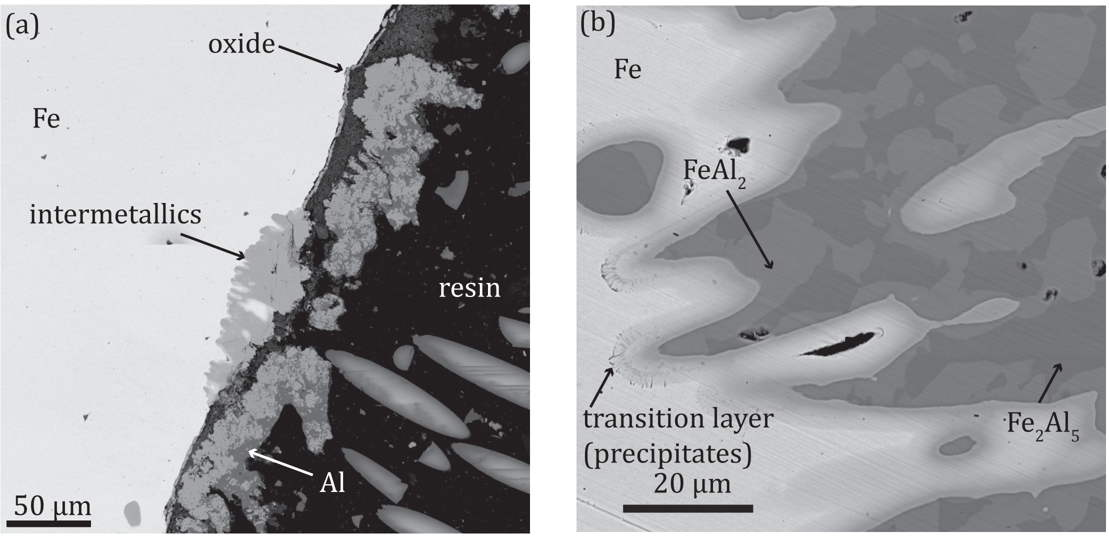

Figure 4.11: SEM (BSE) micrography of Fe sample dipped into Al during 45 minat 700 °C showing (b) the Fe matrix in the left and the tongues in the right in which the $FeAl_2$ appears.

The exact reason of this non reaction is not clear but as one can notice, in these regions, a layer is present on the iron sample. As it will be observed in section 5.1, this layer is an oxide, which could act as a diffusion barrier, keeping aluminium and iron separated. As no reaction occurred, Al did not stick to the surface at the end of the dipping test.

Fig. 4.12 gives the chemical analysis done by EDS in various locations in a tongue. It indicates that light contrasts in the tongue are made of $FeAl_2$, while the rest is made of Fe_2Al_5. The halo in the matrix along the tongues is made of FeAl, that can make precipitates (arrow). in Fig 4.11 (b).

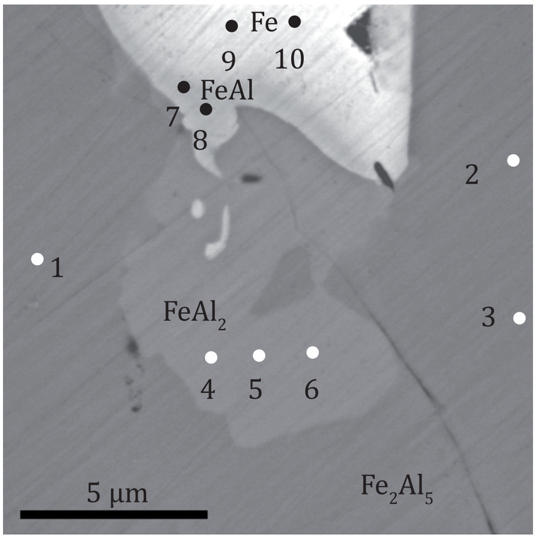

#	Al at. %	Fe at. %	Phase
1	70.88	29.12	Fe_2Al_5
2	70.85	29.15	Fe_2Al_5
3	71.03	28.97	Fe_2Al_5
4	65.86	34.14	$FeAl_2$
5	66.26	33.74	$FeAl_2$
6	66.34	33.66	$FeAl_2$
7	46.83	53.17	FeAl
8	50.31	49.69	FeAl
9	15.46	84.54	Fe
10	17.93	82.07	Fe

Figure 4.12: SEM (BSE) micrography of an Fe sample dipped into Al during 45 min at 700 °C in a valley and results of the EDS analysis giving the concentration of the different locations.

Although the reasons of the incomplete supply in Al are not totally understood, it appears that the latter influences the $FeAl_2$ appearance as the few times this phase was observed, one also observed regions without intermetallic formation.

One remarks in Fig. 4.11 (b) that Fe_2Al_5 is not any more in contact with iron. FeAl or $FeAl_2$ colonised the whole interface in the intermetallics side. It confirms Cheng conclusions on the nucleation of $FeAl_2$ at the interface between tongues and iron and on its growth in direction of the aluminium.

However, they did not observe the contrast in the iron matrix in front of the tongues that is seen in Fig. 4.11 (b), which corresponds to the FeAl transition layer mentioned in the previous section. It appears much thicker than in Fig. 4.9 and 4.10. This larger thickness could also be due to the incomplete Al supply as it was also more visible for sample with intact surface. The small dots present in this transition layer were described by Balloy *et al.* as small graphite lamellae or carbides [61]. Carbides are made of impurities present in the initial Al and Fe.

Solubility limit of this kind of elements in Fe_2Al_5 is much lower than in the initial phases. Thus, during growth, the tongues are rejecting them to the front growth.Their concentration increases, which promotes their precipitation. One can remark that precipitates are more present in front of the tongue tips than on sides of the tongues.

4.2.3 Iron matrix deformation

As tongues are growing in the solid iron matrix, they generate complex strain field in the region of the interface. The tongues being much harder than iron, as seen in section 2.5.4, most of the deformation will occur in the latter. Fig. 4.13 presents the time evolution of a cross-section obtained by X-ray micro-tomography . The liquid Al is in the upper part (dark grey in reverse contrast image), the solid Fe in the lower part (white) and the intermetallic phases in between (light grey). To ensure that the position of the observed cross-section is always the same, a defect in the iron phase is used as a fiducial mark and followed along the experiment. This defect is marked by a black circle in Fig. 4.13 (a).

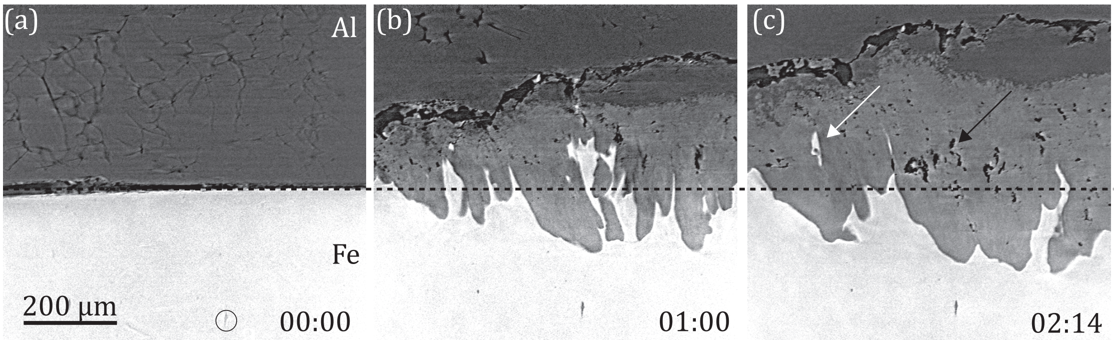

Figure 4.13: *in situ* X-ray micro-tomography observation of the horizontal interface between liquid Al and iron at 700 °C exhibiting an upward movement related to the matrix deformation. Time is given in (hh:mm). A defect circled in image (a) is used as a fiducial mark to ensure the observation position. White arrow marks the presence of an isolated iron island above the initial interface while the black one shows porosity formation discussed in further

.

The initial Fe-Al interface exhibits an upward movement toward the liquid Al, relative to the dashed line in Fig. 4.13 representing the initial position of the liquid-solid interface. Indeed, iron regions are observed above this limit for times different from zero as presented in Fig. 4.13 (b,c). Furthermore, after 2 h as in Fig. 4.13 (c) parts of the iron matrix are isolated from the main matrix and trapped in the dense part of the intermetallic layer as indicated by the white arrow. This upward movement cannot be associated with any sample displacement, as the defect used as reference, did not show any significant displacement. It should then be associated with the growth of the intermetallics phase into the matrix, which causes a strong deformation of the latter. SEM observations of chemically etched sample also reveals this matrix deformation. Fig. 4.14 presents an Fe sample dipped into Al during 30 min at 700 °C. The etching makes

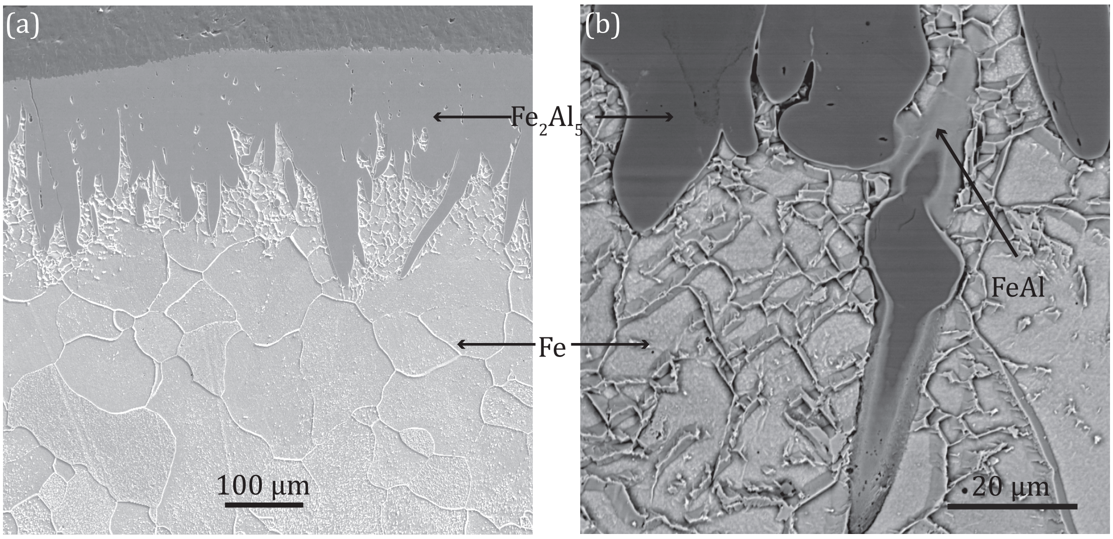

Figure 4.14: SEM (SE) micrography of an Fe sample dipped into Al during 30 min at 700 °C, and chemically etched to reveal the iron microstructure. (a) micrography showing the deformation of the iron matrix in the direct surroundings of the tongues. (b) Higher magnification micrography revealing the FeAl phase around the tongue.

appearing the grain boundaries in the matrix.

It appears that the iron matrix surrounding the tongues suffers a recrystallisation and thus confirms the presence of a stress field induced by the tongue growth.

The upward movement observed *in situ* and the recrystallisation observed *post mortem* confirm swelling observation made by Gedevanishvili *et al.* [18] and Kang *et al.* [19]. The swelling could be interpreted as an increase of molar volume when pure materials transform into Fe_2Al_5. In this situation, stress field is induced by the tongues, which occupy a larger volume than the initial matrix. Thus, tongues are under a compressive field while iron matrix is under a traction field. However, the lack of information on Fe_2Al_5 properties and in particular on the thermal expansion coefficient, does not allow to compare the pure material molar volumes to the transformed one at 700 °C.

Furthermore, as deformation induces an increase in grain boundary density in between the tongues Al diffusion in this region increases, promoting the tongue thickening described in section 5.5. Thus, presence of Al in the Fe matrix could also explain the stress field by increasing its molar volume. In this situation, stress field is inverted compared to the first one with the iron matrix suffering compression while the tongues are in traction. Nevertheless, this situation implies diffusion of Al at a large scale in the iron matrix, which is in contradiction with the concentration profile measured in Fig 4.9 showing that the boundary layer is of some nm.

4.2.4 Porosity formation

In addition to the iron islands observed in Fig. 4.13 (c), dark dots progressively appear in the intermetallic layer as the one indicated by the black arrow. They correspond to porosity. As mentioned in section 2.3, two phenomena can cause porosity formation: the Kirkendall effect, due to a difference in atomic species flux in the layer, and a more mechanical effect linked to phase transformation and associated to a stress field. Fig. 4.15 (a) presents an Fe sample dipped into Al during 60 min at 700 °C and investigated by SEM. The EBSD reconstruction presenting Euler 1 angle colouring allows tongues differentiation and is superimposed to SEM (SE) micrography in Fig. 4.15 (b).

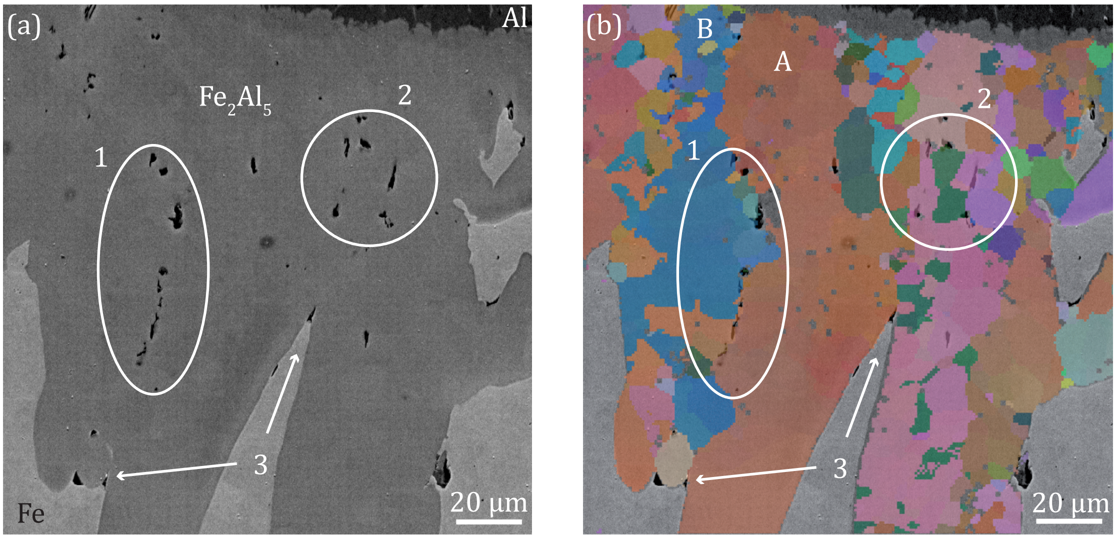

Figure 4.15: Fe sample dipped into Al during 60 min at 700 °C. (a) SEM SE micrography of the tongues with three regions including porosities. (b) EBSD mapping (Euler angle) allowing differentiating tongues. (1) & (2) Interfaces between tongues: regions with higher porosity concentration. (3) tongues valleys that also exhibit porosity.

The polished plane of the image seems to more or less correspond to the central axis of the red tongue (A) growing in the middle of image as its diameter is more or less constant along its growth direction. In its left, the blue tongue (B) may have grown in a different direction, and may have crossed the image plane and thus the red tongue. Indeed, the projection of this blue tongue seems to become thicker towards its tip, as if it was initially hidden under the red tongue and then came out of the plane during growth. The regions marked by the ellipse (1) would correspond thus to the interface between these two tongues, which is situated in the image plane. On can remark that this region exhibits porosity, which is located along the interface. Porosity in region (2) also relates to interfaces between tongues, albeit not as clearly as in region (1). In addition, porosity is regularly observed at the valleys between two tongues as indicated by arrows (3). It therefore might nucleate at the Fe-Fe_2Al_5 interface and not in the Fe_2Al_5 phase itself. In the opposite, the presence of porosity inside a single tongue was not observed.

Porosity formation observed here seems to form on the iron matrix side of the interface. Thus, it is interpreted as related to a mechanical stress field and not to a Kirkendall effect. Indeed, Kirkendall effect is recognizable by a clear positioning of the porosity parallel to an interface (see section 2.3) of the phase in which it is forming. If a Kirkendall effect was at the origin of this porosity formation, it would be due to a species flux difference in the iron matrix, with Fe diffusing slower compared to Al. In other words, Fe supply from the matrix would be limited, which is inconsistent.

This observation tends to confirm that iron matrix is in traction due to the tongue growth as presented in the previous section and thus that molar volume of Fe_2Al_5 is larger than the one of five moles of Al and two of Fe at 700 °C.

In addition, Fig 4.16 presents *in situ* observations of the solid-liquid interface. Arrow (1) in image (a) shows remaining iron matrix (as mentioned in section 4.2.3). In image (b), this iron island is not present any more and is replaced by a large pore that can be observed in each image of Fig. 4.16. This porosity is similar to the one denoted by arrow (2) in image (a). They

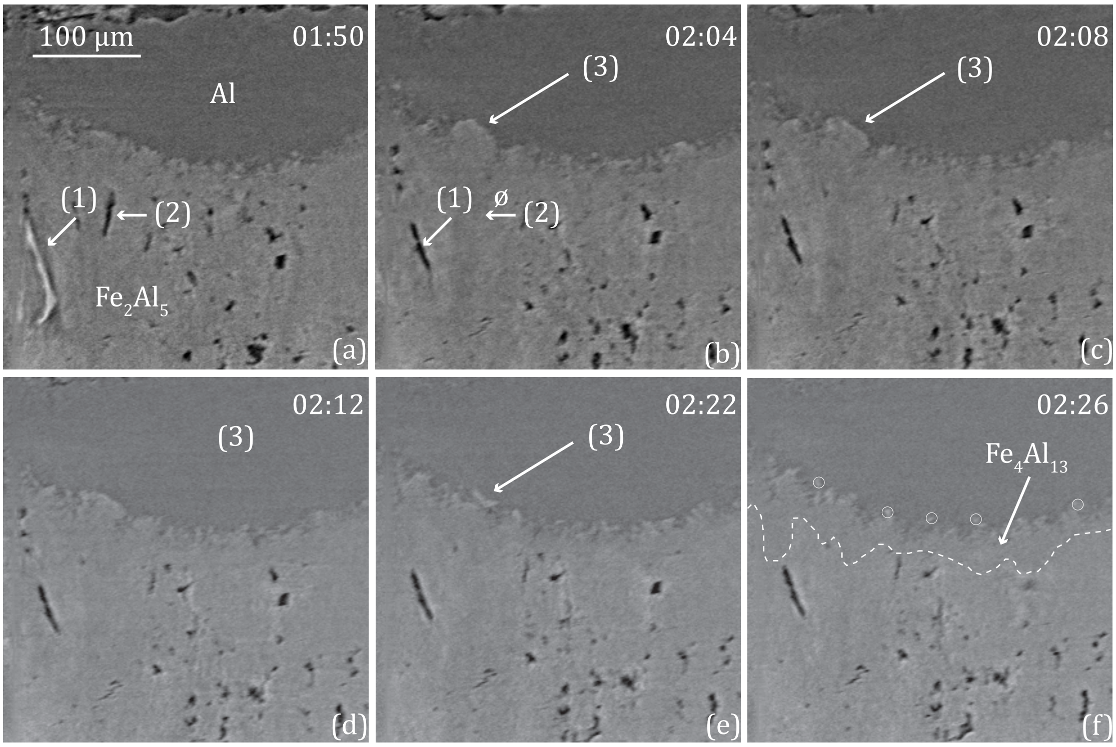

Figure 4.16: *in situ* observation sequence of the interface between the formed intermetallic layer and the liquid, time is given in hh:mm. Arrows corresponds to: (1) porosity formation, (2) porosity disappearance and (3) Intermetallics dissolution (see section 4.3.2). Dashed line in (f) highlights the presence of Fe_4Al_{13} (section 4.3.1).

both exhibit a preferential orientation slightly misorientated compared to the main growth direction that is vertical. It can be interpreted as the interface between two tongues. It also shows that both of them result from the meeting of two tongues.

In addition, pore (2) disappears between image (a) and (b), showing that porosity evolves in the solid-liquid interface vicinity. It is not possible to clearly explain the phenomena that lead to pores closing. However, it could be due to a mechanical compression field or effect of the layer dissolution presented further.

4.3 Interface with liquid Al

4.3.1 Fe_4Al_{13} phase

Increasing the contrast in one of the images presented in Fig. 4.16, one can distinguish a thin layer close to the liquid interface. This layer is marked by a dashed line in the Fig. 4.16 (f). The intermetallic compound above this line is the Al-richest intermetallics, Fe_4Al_{13}. The low difference in density between the Fe_2Al_5 and Fe_4Al_{13} explains the low contrast by X-ray tomography. A better contrast is obtained in SEM (BSE). Fig. 4.17 shows a SEM (BSE) micrography of the interface between the intermetallics and the Al phase on an Fe sample dipped during 60 min into liquid Al at 700 °C. A Fe_4Al_{13} layer is present for every contact time and for any test configuration, vertical or horizontal, with the same thickness of about 10 µm. Thus its means that interfaces, with liquid Al and Fe_2Al_5, move to adapt their velocities in order to keep this thickness constant. As the growth velocity of Fe_2Al_5 is one or two orders larger than the one of Fe_4Al_{13}, the growth of the latter is neglected in the different models

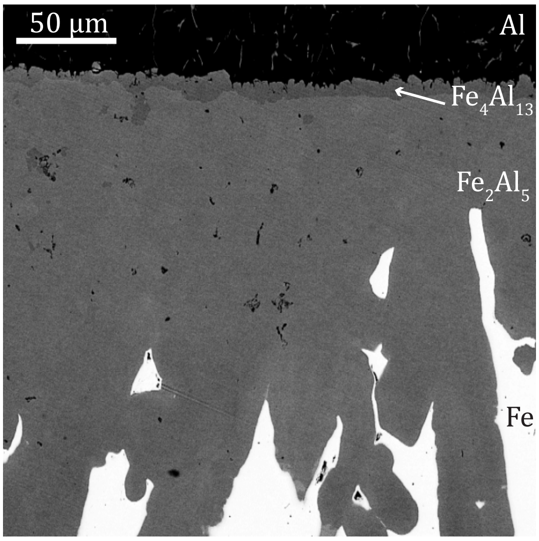

Figure 4.17: Fe sample dipped into Al during 60 min at 700 °C. SEM (BSE) micrography showing the presence of a thin layer of Fe_4Al_{13} between Fe_2Al_5 and Al phase.

(chapter 5 and 6).

4.3.2 Dissolution

Fig. 4.18 presents the interface of three samples after 60 min in contact with aluminium at 700 °C. Fig. 4.18 (a) corresponds to dipping test and Fig. 4.18 (b) corresponds to the test with horizontal interface. In addition, one horizontal test was performed with a pre-saturated bath and is presented in Fig. 4.18 (c).

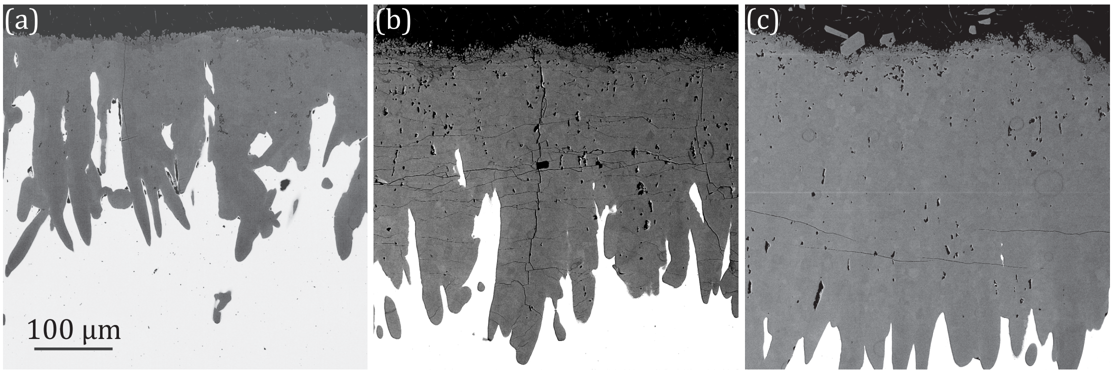

Figure 4.18: SEM (BSE) micrography of Fe samples in contact with liquid Al during 60 min. (a) Vertical interface, (b) Horizontal interface, (c) Horizontal interface with pre-saturated bath.

As expected, the dissolution effect is much more important in dipping test results than in horizontal interface. This comes from the vertical orientation of the interface, implying natural convection and from the bath size, which is almost 50 times larger in dipping test. The dissolution effect is also less visible on the sample tested in the pre-saturated bath, that exhibits a larger intermetallic thickness.

Dissolution seems also to modify the shape of tongue-like. Indeed, from (a) to (c) or from the most to the less affected by dissolution, tongues become less pronounced.

One can also observe in Fig.4.16 (b-f) that intermetallic blocks are disappearing (arrow 3). In addition, the interface seems to desegregate with parts just above the layer that seem detached. Some of them are circled in whit in Fig. 4.16 (f). After detaching, these parts lay on the interface as they are denser than the liquid.

It will be shown in chapter 5 (section 5.3.1) that saturation is achieved in less than one hour for the sample with horizontal interface for *in situ* observation. Thus even though after saturation as it is the case in Fig. 4.16, dissolution still occurs and is observable by blocks disappearing or detaching from the interface. It is interpreted as an effect of the convection, locally on the interface [87]. Indeed a local irregularity as a block being further forward in direction of the liquid than the rest of the surface, the melt in its surrounding is poorer in Fe than at the near interface. A local density gradient appears that implies natural convection.

Fig.4.19 presents the solidified melt microstructure of a horizontal sample for *post mortem* observation after a contact time of 45 min. The microstructure evolution from the interface to

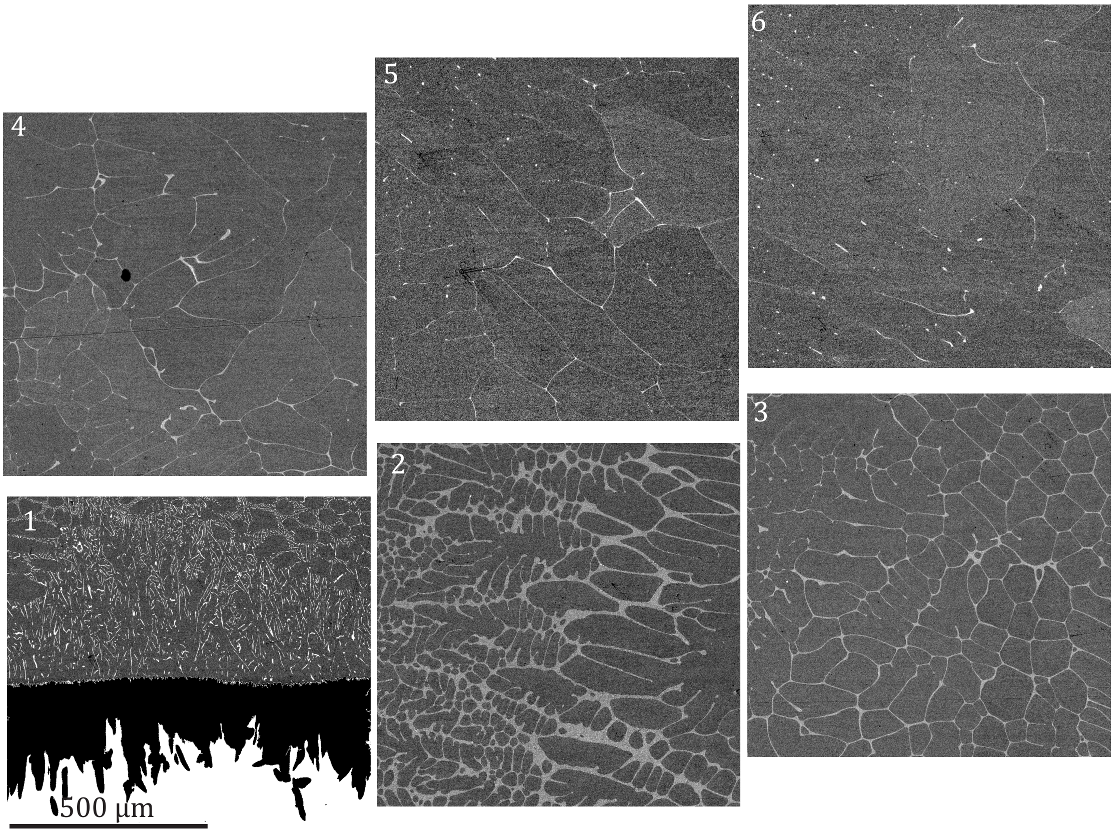

Figure 4.19: SEM (BSE) micrography of the solidified aluminium melt after 45 min of contact with iron. From 1 to 6 evolution from the interface to the melt surface.

the melt surface is presented from image 1 to 6. The intermetallic layer appearing black in image 1 was filled before modifying the contrast that reveals the melt microstructure.

One notices that the Fe_4Al_{13} appearing in white in the melt evolves with the position. In this case, at the near interface, needles of Fe_4Al_{13} are observed. In the other images, it is included in the eutectic phase that surrounds pure Al grains. Thus, compositions correspond to the hyper eutectic region as the primary phase corresponds to pure aluminium. The eutectic fraction progressively decreases from image 2 to 6 as the iron content decreases. It is not possible to resolve both phases in the eutectic at this magnification.

Solidification behaviour also influences the microstructure, especially concerning the morphology of the phases, that are influenced by the cooling rate. As the crucible was laid on the glove box bottom, it is suggested that the main heat flux is in this direction. Then, the first solidification occurs at the interface with iron. It results in a complex microstructure that is difficult to interpret with out of equilibrium frozen phases. Farther in the melt, solidification seems to be more regular. The estimation of the phase fraction made in section 5.3 will mainly consider the phase fraction far from the interface.

Dissolution is a complex problem, involving many aspects such as fluid flow with non-stationary problems. Thus in the next chapter presenting the quantification of intermetallics growth, the quantity of iron needed to saturate the bath and the time needed to achieve the saturation will be approximated. Measurements will then focus on the less affected ones, neglecting the saturation effect. The author is aware that the results will be biased by this assumption. Nonetheless, dissolution will be implicitly included in the determined growth constant. The latter should thus be considered as an apparent one.

4.4 Summary

The close contact between iron and liquid aluminium leads to the formation of an intermetallic layer that is described by three regions, namely the main intermetallics Fe_2Al_5, the interface of the latter with the iron matrix and the one with liquid aluminium.

Fe_2Al_5 grows with a peculiar tongue-like shape in the iron matrix. Tongue tips are close to single crystal and exhibit a regular contrast at nanometre scale. This contrast is identified as due to a slight variation in the chemical concentration. It is suggested that this chemical variation remains within the existence domain of the Fe_2Al_5 phase.

A thin intermediate FeAl layer of some hundreds of nanometres is observed all around the tongues. This phase corresponds to the ordering of the α phase with Al content increasing within its existence domain. In addition, for a particular case related to the partial Al supply, $FeAl_2$ is observed in the tongues. This observation confirms the one of Cheng [47]. Under the effect of tongues growth, iron matrix is strongly deformed. This results in a recrystallisation of the iron matrix close to the tongues, a swelling of the system and pores formation at the interface with tongues.

A Fe_4Al_{13} layer of about 10 µm is observed between the Fe_2Al_5 and the liquid Al for any times and any configurations. Intermetallics dissolution occurs in parallel to its growth in direction of the liquid. It is observed by the comparison of the tests with one performed with a pre-saturated Al alloy. Furthermore, the vertical position of the interface, as for dipping tests is more affected by dissolution, due to natural convection. This point is more detailed in chapter 5.

5 Intermetallics evolution

This chapter focuses on the time evolution of the intermetallic layer. Fig. 5.1 presents the time evolution of the cross section in the X-ray tomography of an iron specimen exposed to Al at 700 °C. Iron appears in light grey at the bottom, while aluminium is dark grey at the top. The intermetallic layer progressively appears at the interface in medium grey. Time zero (Fig. 5.1.1) is given by the last tomogram exhibiting an interface without visible intermetallics, which happened after 16 min at 700 °C in this case. Evolution of the morphology was described in a publication in Metallurgical and Materials Transactions A in September 2013 [84].

The incubation time observed before the formation of the first intermetallics is presented in section 5.1, which focuses on the very beginning of the reaction with blocks appearing in the liquid aluminium side of the interface (Fig. 5.1.2) and the rapid emergence of the tongues in the iron matrix (Fig. 5.1.3).

Section 5.2 presents the thickness W of intermetallics as a function of time for the four different test configurations, namely the *in situ* and *post mortem* observations of samples with horizontal and vertical interfaces. Section 5.3 presents an estimation of the melt saturation effect for each test and the effect of the cylindrical geometry on tongue growth.

Section 5.4 focuses on intermetallics growth in the *in situ* observation of the sample with a horizontal interface and presents the analysis of the equivalent thickness of the formed tongues and the thickness of the dense intermetallic layer. The resulting growth constant coefficients are compared to values from the literature by means of the numerical model presented in section 3.6.

Section 5.5 presents the tongues surface density and compares its evolution to the different regimes measured in section 5.4.

Growth is also described by the interface positions with time in section 5.6. It gives complementary information that allows a better representation of the swelling and saturation effects.

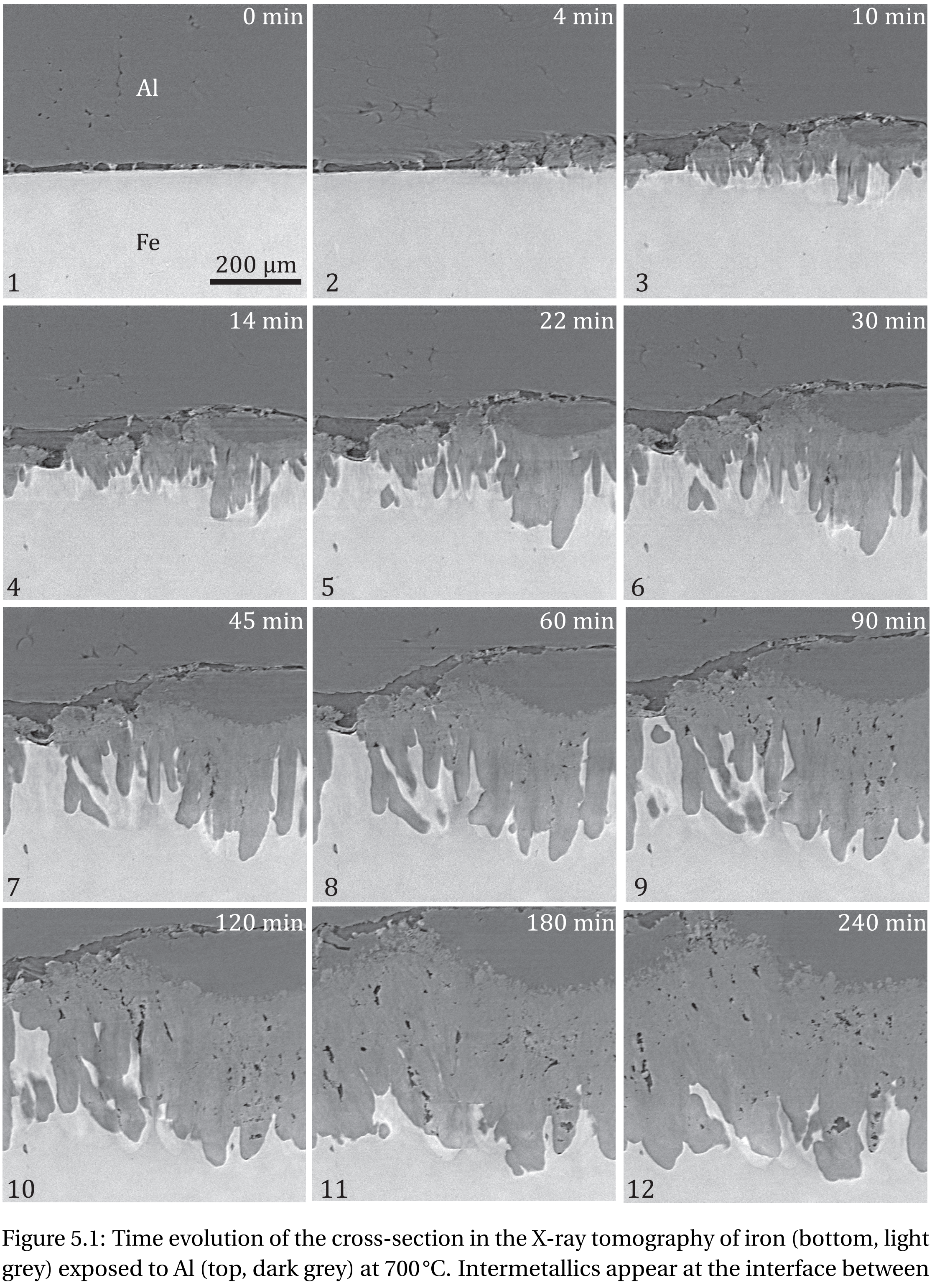
0 min
Al
Fe
200 μm
1
4 min
2
10 min
3
14 min
4
22 min
5
30 min
6
45 min
7
60 min
8
90 min
9
120 min
10
180 min
11
240 min
12

Figure 5.1: Time evolution of the cross-section in the X-ray tomography of iron (bottom, light grey) exposed to Al (top, dark grey) at 700 °C. Intermetallics appear at the interface between them, in medium grey.

5.1 Beginning of reaction

In situ observation allowed obtaining information concerning the very beginning of the reaction. Fig. 5.2 presents two cross-sections similar to the one presented in Fig. 5.1 and one SEM (SE) *post mortem* micrography of a horizontal interface after 60 min of contact. One can observe in Fig. 5.2 (a) that the reaction occurred first in the liquid side of the interface with the formation of blocks, from which tongues emerge and grow into the iron phase. Furthermore, the reaction did not occur uniformly at the iron surface. Region marked by arrow (1) was free of intermetallics while region (2) already reacted. This non-uniformity of the reaction is interpreted as due to a native oxide layer present on the aluminium, which represents a diffusion barrier and thus an obstacle to liquid Al supply. Although experiments were performed under a protective atmosphere, the presence of a few ppm of oxygen is sufficient to form an oxide layer on the iron surface, that can also slow down the Al supply.

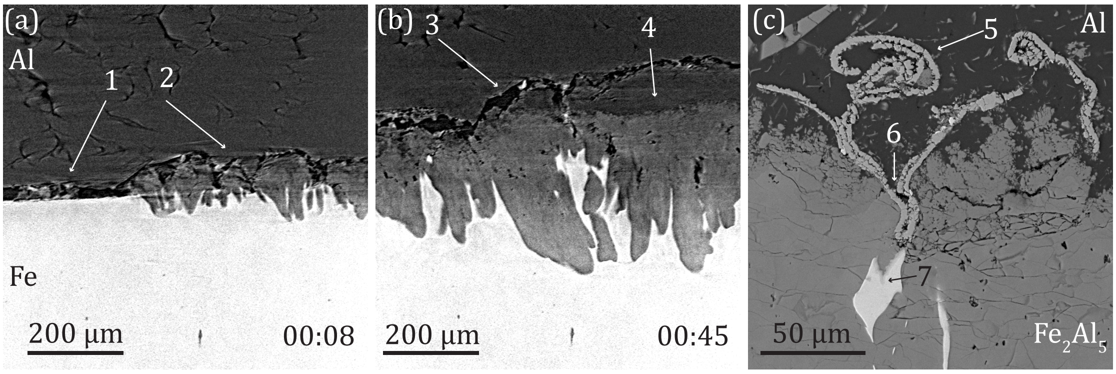

Figure 5.2: Pure Fe expose to Al at 700 °C showing the beginning of the reaction and effect of the initial oxide layer. (a) and (b) cross-sections of the *in situ* X-Ray tomography horizontal sample 20 and 60 min after the beginning of the recording, respectively. (c) *post mortem* SEM (SE) micrography of the interface between Fe_2Al_5 and liquid showing the oxide layer (5,6) blocked in the intermetallics.

While the oxide skin is too thin to be observed *in situ* , the gap between this oxide and the iron or intermetallic appears black in Fig. 5.2 (b, arrow (3)). The reaction can proceed further only if the liquid can flow under this oxide skin through a crack. Note that this supply may originate from other locations not visible in this cross section. One can observe, especially in image (b), a portion of liquid that has flown under the oxide skin (arrow 4). This region was likely to be more supplied at the beginning of the experiment, the reaction started first here. The cracks may be induced by strains on the interface, as a result of thermal or phase expansion. This is verified by a *post mortem* SEM (BSE) micrography in Fig. 5.2 (c) presenting a thick oxide layer (arrow 5) that broke and was caught by the growing intermetallics (arrow 6). One can remark the presence of iron (arrow 7) near the interface, indicating that a low supply in Al to this the region due to the oxide layer damped the reaction.

5.2 Intermetallic thickness evolution

The intermetallic thickness W as a function of time was extracted from the equivalent thickness measurement from *post mortem* observations (section 3.5.2) and from the area fraction measurement from *in situ* observations (section 3.5.3). In the latter, the thickness was obtained by dividing the measured volume by the observation surface of $600 \times 600\,\mu m^2$. The thicknesses for the four different tests are presented in Fig. 5.3 as a function of the square root of time. Errors are estimated as the standard deviation for equivalent thickness measurements and from the estimation of 5 % of error in the measurement of the area fraction. *In situ* measurements at negative times are due to the incubation time observed at the beginning of the reaction and induced by the oxide layer (i.e., time t= 0 was set at the beginning of the reaction). In order to compare the different measurements, the reaction start up time was defined by the time at which W reached 5 µm. It was not possible to adjust the reaction time for *post mortem* observation and thus no correction was performed for them.

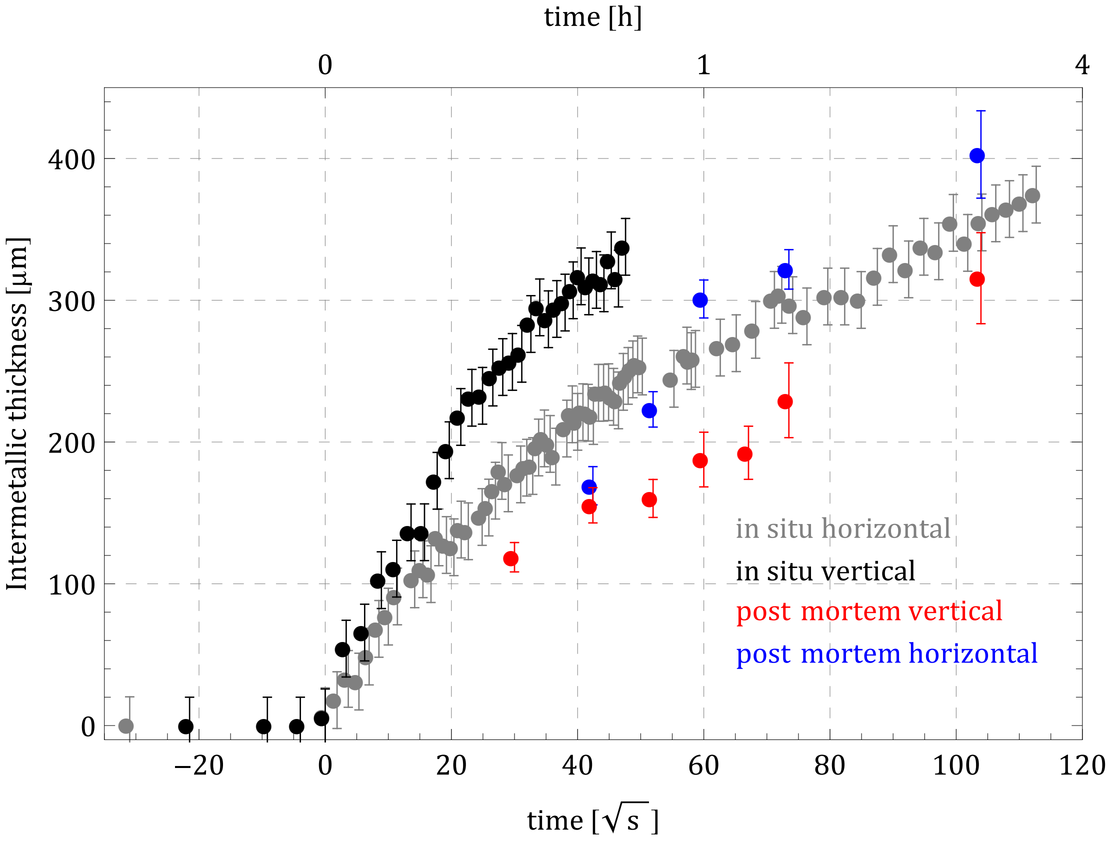

Figure 5.3: Intermetallic equivalent thickness measurements as a function of the square root of time. Black: *in situ* vertical, grey: *in situ* horizontal, red: *post mortem* vertical, Blue: *post mortem* horizontal.

Note that the measurements of the vertical *in situ* specimen (black dots) could not be performed after about 40 min because the solid – liquid interface disappeared from the field of view.

The sample with horizontal interface for *post mortem* observation in contact during 15 min (blue dots) is missing. The reaction was not sufficient to obtain a good welding and no adhesion was observed. It also confirms the effect of oxide layers on the reaction initiation.

5.3 Measurement variation according to test configuration

As mentioned in section 2.1.5, the melt saturation that occurs at the beginning of the contact influences the measured thickness W by dissolving part of the intermetallic layer. Melt saturation is achieved at 700 °C when the Al concentration reaches 98.2 at %. The saturation achievement depends on the bath volume and on the iron flux. The latter depends on the exchange surface and on the dissolution rate k at the interface. Thus, each configuration saturates over different times and needs different iron quantity. This section tries to estimate the thickness of material that should dissolve and the time needed to achieve the saturation for the four configurations.

Furthermore, the dissolution rate is associated with diffusion in the liquid, which is strongly influenced by convection, especially for vertical interfaces. A complementary observation of a dipping-test sample is done here as additional information on the convection effect.

In addition, the sample with a small radius used for the *in situ* observation of the vertical interface presents an increase in tongue growth that is also presented in this section

5.3.1 Bath saturation

Iron content in the saturated bath

The quantity of iron needed to saturate the bath is calculated from system dimensions. In order to compare the four different configurations, one can deduce the thickness of the solid part (Fe or Fe_2Al_5) that has to be dissolved to saturate the melt. As saturation occurs at the beginning of the reaction, they can be both in contact with pure Al. Table 5.1 presents the geometry of the four different tests and the calculated dissolved thicknesses for both the Fe and the Fe_2Al_5 phases.

One can notice that both *in situ* experiments experience nearly equivalent dissolution with about 100 μm of the initial iron sample that dissolves. It represents about 20 % of the sample radius in the vertical configuration and about 4 % of the sample height in the horizontal one.

The dipping tests with the largest melt dimensions would need more than 80 % of sample's initial radius to saturate the bath, which was not observed. One can thus consider that dipping tests were performed in a nearly unsaturated bath over the whole time of the experiment.

Table 5.1: Dimensions of the four different configurations and calculated thicknesses of dissolved Fe. r_1 corresponds to the iron sample radius, r_2 in the vertical configuration to the melt radius, h to the melt height. S is the surface of contact between the initial iron and the melt and V the melt volume. Dissolved thickness of Fe and Fe_2Al_5 is calculated assuming each of the phases is in direct contact with the melt.

Test	*in situ* V	*in situ* H	*post mortem* V	*post mortem* H
r_1 [mm]	0.5	1	5	5
r_2 [mm]	1	-	21	-
h [mm]	6	3	40	16
S [mm^2]	19	3.1	1256	78.5
V [mm^3]	4.7	9	52100	1250
dissolved Fe thickness [μm]	97	114	4100	604
dissolved Fe_2Al_5 thickness [μm]	110	146	4600	775

Likewise, it would represent about 30 % of the iron thickness for the sample with horizontal interface.

The estimation does not take into account the quantity of Al that diffuses into iron and forms intermetallics. The calculated dissolved thicknesses are thus over evaluating the real dissolution effect as the bath volume is actually smaller than at the beginning of reaction. One can nevertheless see that the least dissolved sample is in absolute value the the one with vertical interface for *in situ* observation but relatively to the initial iron sample, the one with horizontal interface for *in situ* is the less dissolved.

Saturation time

On the one hand, taking into account the work of Yeremenko [10], and particularly Equ. 2.44 remembered here:

$$\bar{c}(t) = c_s \left(1 - \exp\left(-\frac{kSt}{V}\right)\right) \tag{5.1}$$

that gives the mean melt concentration $\bar{c}(t)$ as a function of time, one can estimate the time at which the bath should be saturated. However, unlike Yeremenko's experiment's, the present experiments were performed without rotating the samples. Therefore, the dissolution rate k measured by Yeremenko is certainly higher than the ones valid in this work. In particular because Yeremenko's experiments were performed under a forced convection regime implying an Fe depletion of the liquid near the interface. One can consider this Yeremenko's coefficient as the highest dissolution rate and thus the time at which saturation is achieved as the shortest one. In the following, this dissolution coefficient is called k_s.

On the other hand, an upper limit for the saturation time is given by pure diffusion of iron in the melt, without convection and neglecting saturation effect on the flux. The dissolution rate k_l for this case is defined by the ratio between the diffusion coefficient in liquid and the boundary layer δ:

$$k_l = \frac{D_{Fe}^{Al(l)}}{\delta} = \sqrt{\frac{D_{Fe}^{Al(l)}}{t}} \tag{5.2}$$

A plot of Equ. 5.1 as a function of the square root of time with the two dissolution rates k_s and k_l provides an estimation of the time range needed for bath saturation. Fig. 5.4 (a) presents these ranges as coloured surfaces between the shortest saturation time determined with k_s and the longest determined by k_l as shown in the case of the horizontal interface for *post mortem* observation (in blue). The other colours black, grey, and red correspond to *in situ* vertical and horizontal and *post mortem* vertical experiments respectively.

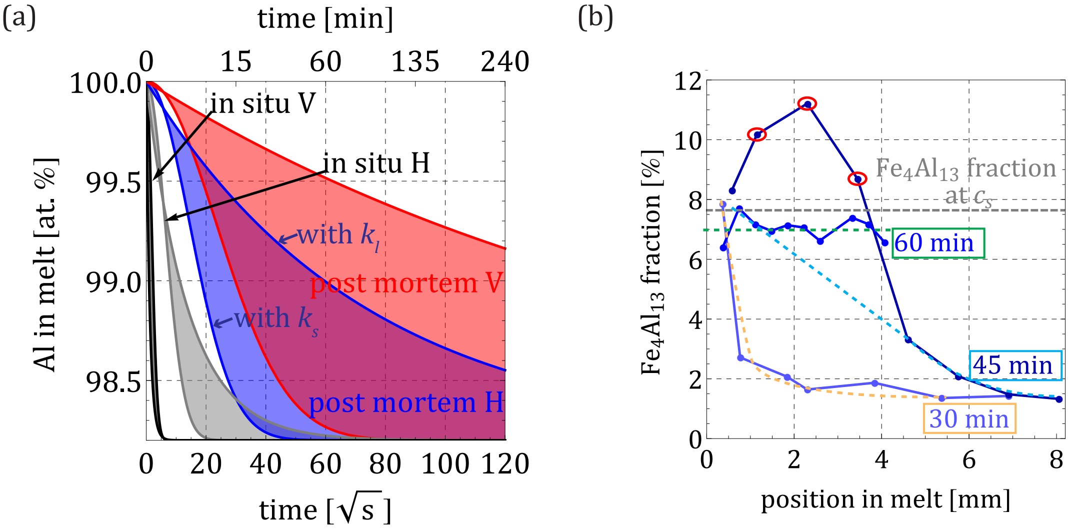

Figure 5.4: Bath saturation. (a) Mean bath Al atomic fraction calculated from Equ. 2.44 taking into account a dissolution coefficient k_s for the shortest saturation time and k_l for the longest one. (b) Results from the area fraction of Fe_4Al_{13} phase in the solidified bath for *post mortem* horizontal samples.

Fig. 5.4 (b) presents the result of the local concentration obtained by phase fraction measurements on *post mortem* the horizontal sample. Phase fractions were extracted from micrographies like the ones presented in Fig. 4.19. Positions are referring to the central point of images used for the measurement. Position zero corresponds to the interface with the intermetallic layer. The measurement on the 60 min-contact sample was performed only 4 mm from the interface because the upper part of the bath was unfortunately cut during sample preparation.

The Fe_4Al_{13} phase fraction of the saturated bath is equal to 7.64 % (section 2.1.5) and is given by the grey dashed line in Fig. 5.4 (b).

As mentioned in section 4.3.2, the fast solidification near to the interface leads to complex microstructructures that may not follow thermodynamics law. It is especially the case for measurement circled in red on the sample after 45 min contact that exhibit measured values above the concentration limit. On the contrary, the two others at 30 min and 60 min give regular profiles.

A rough estimation of the concentration profiles is given by dashed lines in Fig. 5.4 (b). One remarks that the latter is sharp after 30 min and progressively flatten until 60 min where it is horizontal. Thus saturation seems to occur between 45 and 60 min for this configuration. This time is situated within the interval given by k_s and k_l of the horizontal test for *post mortem* observation as shown in Fig. 5.4(a) in blue. The fastest saturation calculated with k_s occurs for this test after about 45 min, while the slowest calculated with k_l occurs at a time out of the experiment range.

In addition, it appears that the result is closer to the limit given by k_s. Thus, saturation time seems to correspond to the lowest time limit, at least for horizontal interfaces.

One can also remark that saturation time ranges are small for both *in situ* measurements with few seconds for the vertical test (black) and between 20 min and 1 h for the horizontal test (grey). As the *post mortem* measurements performed on the sample with horizontal interface show that saturation is achieved at the beginning of the calculated interval, one can suppose this is also the case for the *in situ* test in the same configuration. Thus it is assumed in the following that saturation occurs after approximately 20 min for the *in situ* horizontal test.

For this test, considering that dissolution occurs only on the formed intermetallics and not on the initial iron part, the calculated thickness of 150 µm (table 5.1) represents about 75 % of the formed layer that is about 200 µm at the estimated saturation time of 20 min (see Fig. 5.3).

Convection effect

Saturation in dipping tests (red in Fig. 5.4) does not occur before about 60 min. These tests suffer from natural convection, particularly because of the large volume of the melt. It results in a heterogeneous dissolution of the formed layer along the vertical axis. In order to show this effect, observations at different vertical positions were performed on a sample dipped during 60 min. In parallel, another sample dipped for the same duration was chemically etched to remove intermetallics and stuck Al. Fig. 5.5 presents the etched sample and a plot of the measured diameter along the sample in black and the intermetallic thickness at three different positions in red. Lines between measurements estimate the variation. The position refers here to the bottom of the iron finger and the melt surface is measured at 40 mm as presented by the dashed line on the top of the plot. In addition, arrows show the direction of the convection, given by the vector product of the gravity $\vec{g}$ and the density gradient $\vec{\nabla}\rho$.

Natural convection occurs because of the difference in iron concentration in the bath between the interface with the iron part and far from this interface (at the crucible side). This implies a movement of the fluid that enriches the melt in iron in the lower part and impoverishes it

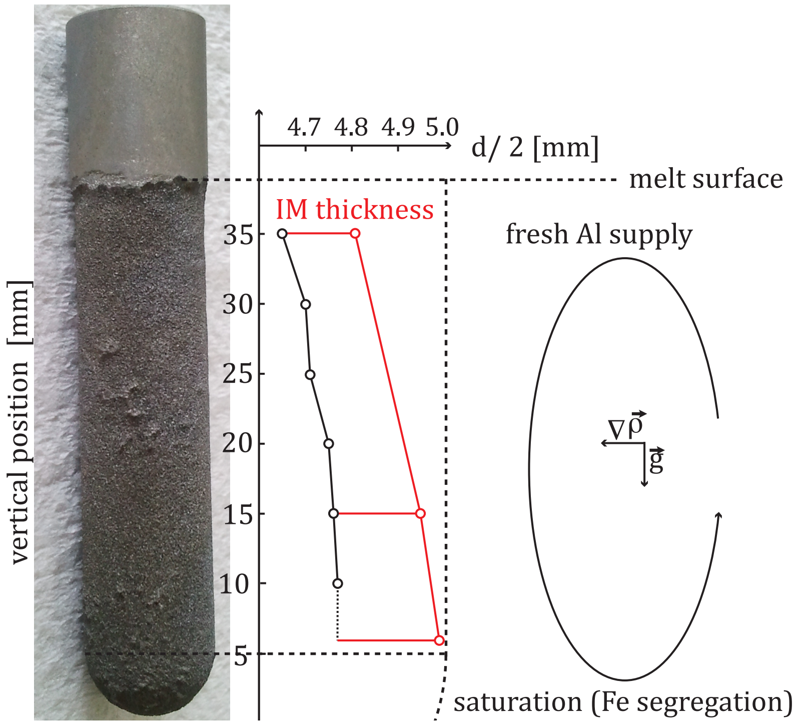

Figure 5.5: Iron sample dipped during 60 min into pure Al at 700 °C and chemically etched together with measurement of remaining iron radius (black) and intermetallic layer thickness (red) as a function of the vertical position. The sample is 50 mm long. Schematics of liquid movement induced by natural convection is given on the right.

in the upper part. In addition, blocks detaching from the intermetallic layer being heavier than the liquid, they tend to sink, increasing the fluid velocity. This implies that the region at the upper part is supplied with fresher Al and is thus more subject to dissolution [88]. This results in a more important dissolution at the upper part of the sample, which is confirmed by experimental results with a remaining radius of 4.64 mm while at the bottom it is about 4.75 mm.

In addition, one can remark that dissolution also influences the measured intermetallic thickness with respectively 230, 190 and 160 µm from bottom to top, with an increase of of almost 50 % between the smallest and the largest thicknesses.

5.3.2 Cylindrical geometry

One remarks in Fig. 5.3 that the beginning of the reaction for both *in situ* experiments is similar but that measurements diverge after about 100 s (or 100 µm). Although this difference is not yet clearly understood, two aspects seem responsible for this difference.

As already mentioned, the vertical interface test for *in situ* observation is the one with the shortest saturation time. Thus one could expect that divergence occurs when the bath is saturated for the vertical configuration, implying in this case that it happened after about 100 s.

The second reason comes from the geometry of the sample. Fig. 5.6 presents one segmented image of the interface between the Fe_2Al_5 tongues and the iron matrix for a sample with a vertical interface. One can notice in this figure that unlike the three other configurations, the vertical one for *in situ* observations presents an intermetallic layer, which is influenced by the curvature of the iron sample. Indeed, with a formed thickness W of about 300 µm after about 30 min, the intermetallic layer represents 60 % of the initial radius. The same intermetallic thickness for the *post mortem* sample represents ten times less of the initial radius, while horizontal interfaces are by definition not influenced by this effect. It has to be remembered here that the thickness corresponds to a planar front and thus the total equivalent thickness represents 300 µm although some tongues are much larger in Fig. 5.6.

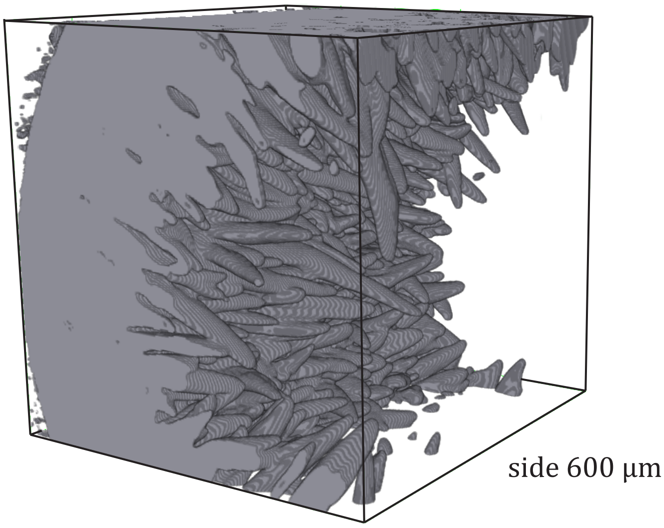

Figure 5.6: 3D segmented image of the interface between intermetallics and iron obtained by X-ray tomography observation after 36min of contact in the vertical configuration. The iron phase has been made transparent.

Taking into consideration the solute balance in cylindrical coordinates, one notices that the flux varies with the inverse of the radius. Thus, as the flux is proportional to the velocity and the concentration and as the latter is constant, growth may accelerate due to the decrease of the radius.

One notices that the sample with horizontal interface for *in situ* observations is the least affected by the effect of saturation and curvature. Indeed, the quantity of iron needed relatively to the size of the iron piece to saturate the bath is the smallest of the four tests. Furthermore, it is observed that in the horizontal configuration, the saturation time is close to the fastest limit described by Yeremenko's coefficient k_s. Knowing that Al and Fe were in contact from the beginning of the heating, which implies some iron dissolution during this period and considering in addition the incubation time before the formation of intermetallics, one can assume that the bath was already partially saturated when the first intermetallics were observed. Thus, the effect of saturation is limited for such test, while geometrical effects do not influence the measurement. Next section will therefore focus on this test for the different measurements.

However, saturation still influences the growth and thus the constant K measured in the next sections should be considered as an apparent one, that includes the formed thickness and its dissolved part. It allows to compare K to values from the literature, which generally also neglects the saturation effect. Furthermore, it also allows the use of the numerical model that considers a saturated bath.

5.4 Growth regimes

Fig. 5.7 presents the intermetallic thickness evolution for the *in situ* observations of the horizontal interface. Data in grey correspond to the dense part of intermetallics (with an area fraction above 90 %, see section 3.5.3) and the red line corresponds to its fits with a function $K_d\sqrt{t}$. Data in black correspond to the total intermetallic thickness, taking also into account the tongues (i.e converted into a dense layer). One notices a change in growth rate between about 5 and 30 min or 17 and 45 $\mathrm{s}^{1/2}$ respectively. Arbitrary regimes presented by arrows in the upper part of the plot are defined as follow, considering the two regimes with constant growth rates T_1 and T_3 and the one with non-constant growth rate T_2:

- T_1 corresponds to the very beginning of the growth and lasts approximately 15 min (image 1 to 5 of Fig. 5.1).
- T_3 is the longest regime and corresponds to the end of the observation, starting after about 30 min (image 9 to 12 of Fig. 5.1).
- T_2 is the transient regime from T_1 to T_3 during which the growth rate is not constant (image 5 to 9 of Fig. 5.1).

Regime limits are arbitrary determined by a *best-fit method*. Best fits are defined as the fits with the lowest mean error (coefficient of determination R^2 nearest to 1). For example, the determination of the fit of T_1 is obtained by considering each data set from the first point (0,0) to the nth, with n varying from 1 to the number of measurements. For each set, fits and coefficient of determination are calculated and the one with the highest R^2 value is considered. The same determination is performed for T_3, starting from the last measured point and adding one after the other measured point to calculate the different fits. The fits allow to extract growth constant for the two regimes with a constant slope K_i with $i = 1,3$ and thus an approximation of the apparent diffusion coefficient by means of Equ. 2.16. Results are presented in table 5.2 and compared to values at 700 °C from the literature (section 2.5.6).

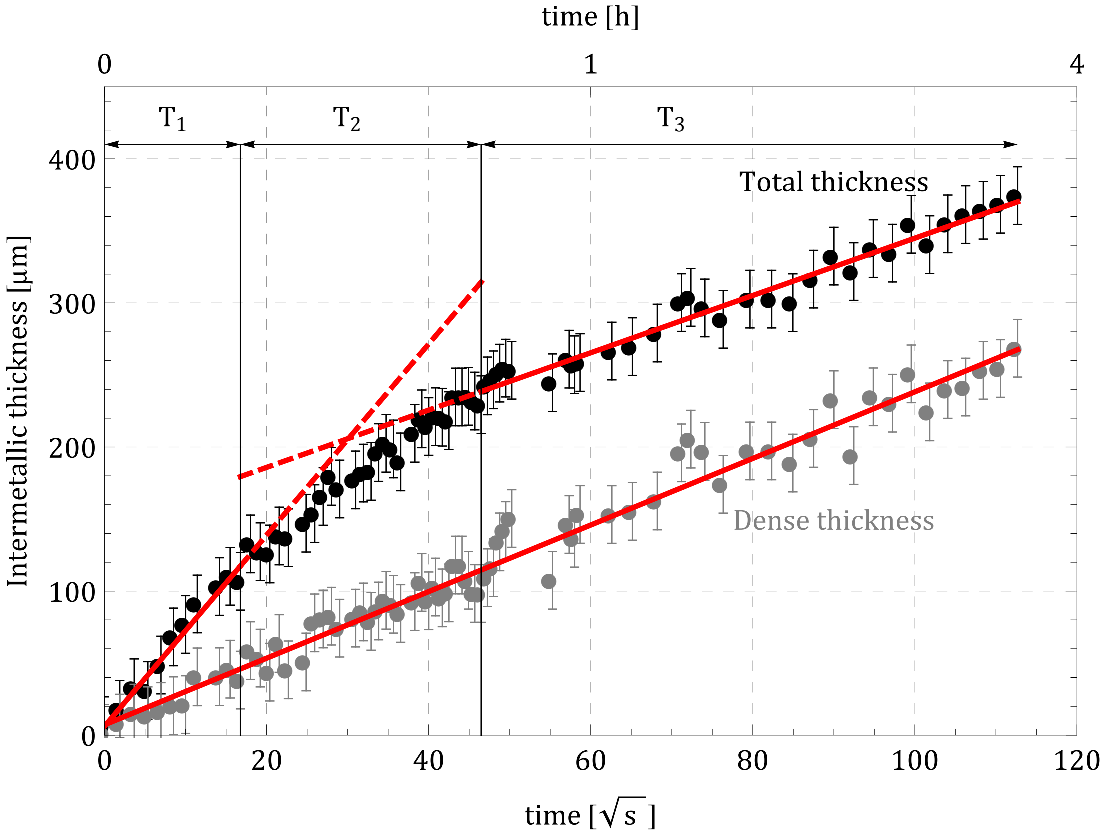

Figure 5.7: Intermetallic equivalent thickness measurement as a function of square root of time for the *in situ* horizontal test. Black: total volume divided by the observed section. Grey: volume of the intermetallic dense part (area fraction above 90 %) divided by the observed section. Difference in growth rate is highlighted by a parabolic fit at the beginning (regime T_1) and at the end (regime T_3). In between, the transient regime T_2 is characterized by a non parabolic behaviour.

Values from the literature presented in this table correspond to the lowest interdiffusion coefficient measured by Kajihara [40] and the highest one measured by Tanaka [11]. The fit of

Table 5.2: Measured growth constant for the different observed regimes. Deduced interdiffusion coefficient in Fe_2Al_5 from Equ. 2.16 and comparison with interdiffusion coefficients at 700 °C found in the literature.

	K [$m \cdot s^{-1/2}$]	$\tilde{D}$ [$m^2 \cdot s^{-1}$]	Ref.
Highest value	-	3.17×10^{-11}	[11]
Regime T_1	6.3×10^{-6}	4.5×10^{-12}	-
Regime T_3	2.05×10^{-6}	4.2×10^{-13}	-
Lowest value	-	3.1×10^{-13}	[40]
Dense layer	2.31×10^{-6}	5.4×10^{-13}	-

regime T_1 gives an apparent diffusion coefficient in Fe_2Al_5 one order of magnitude below the highest value found by Tanaka [11] while the one of T_3 as well as the one of the dense part are close to the lowest value found by Kajihara [40].

When having a look at the time ranges used for experiments, Tanaka [11] studied the intermetallics for short times, up to 10 min while Kajihara [40] studied longer times, between 30 min and 100 h. Thus, Kajihara's results describe the long term evolution while Tanaka's one the very beginning. As they proceeded by *post mortem* observations, they were not able to fully describe the growth.

In order to verify the measured diffusion coefficients, they were implemented in the numerical model, as well as coefficients from literature. To simulate the two regimes, the code was run twice with each diffusion coefficients and the thickness calculated during the second regime was added to the one calculated at the end of the first regime. The limit between both regimes was defined as the time at which the calculated fits of Fig. 5.7 are equal. Fig. 5.8 presents the result of the simulation with the measured diffusion coefficient (in green to distinguish the result from the fits presented in Fig. 5.7) and both results with lowest (Kajihara [40]) and highest (Tanaka [11]) diffusion coefficients. Measurements from the tomography results are added to the plot.

The simulation of regime T_1 follows well the experiments. It is nonetheless much smaller than the result of the simulation with Tanaka's value of diffusion coefficient. It has to be noted that Tanaka worked with a temperature range higher than 700 °C (between 780 and 820 °C) and that he extrapolated values to 700 °C with an Arrhenius law, without taking into account the magnetic transition at the Curie temperature (770 °C). Thus, his measurements might over evaluate the behaviour at 700 °C.

The simulations during the second regime, although thickness is shifted upwards, represents well the behaviour, being parallel to the measured points. The shift upwards is explained by the extension of T_1 in the T_2 domain. Acting longer than in reality, the growth rate in T_1 implies an artificial increase of the thickness. One possible issue to this shift could be to find a diffusion coefficient $\tilde{D}_2$ that varies during the transition regime T_2 from the value of $\tilde{D}_1$ to $\tilde{D}_3$ but such a coefficient would have no real physical meaning and thus would not represent any real phenomena.

Simulation of the dense part growth is slightly diverging from the experimental points, while simulation with Kajihara's coefficient perfectly fits those measurements. One can also remark that these present a similar slope as regime T_3. As no information on Kajihara's measurement method was found and no micrography was presented in his article, it is difficult to interpret their result. The main point is that Kajihara proceeded by reaction diffusion bonding, under the melting point of Al (up to 640 °C). Thus, the beginning of reaction could be much different and tongues might not appear as it will be shown in section 5.5 and chapter 6.

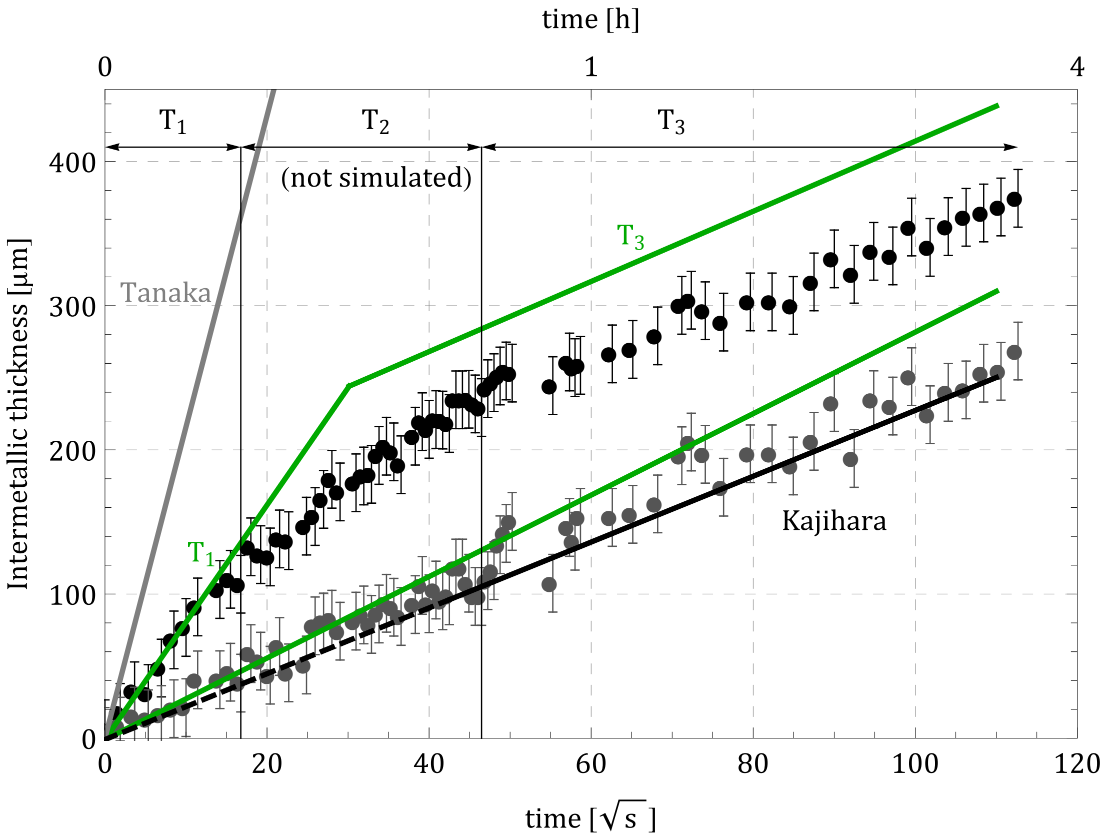

Figure 5.8: Results of the simulations with the different diffusion coefficients presented in table 5.2 and comparison with measured thickness: black: total thickness, dark grey: thickness of the dense part. In order to distinguish them from fits of Fig. 5.7 (in red) simulation result is presented in green. Simulations with diffusion coefficients from the literature are given in grey and black for Kajihara [40] and Tanaka [11] respectively. Dashed line corresponds to the projection to shorter times than the ones studied by Kajihara.

Although two main growth regimes are shown here, with a transition one in between, the reason of this modification in growth behaviour is not explained yet. Tongue thickening presented in the next section could give part of the explanation.

5.5 Tongue thickening

It appears in tomography reconstructions that tongues thicken with time (Fig 5.1). The quantification of the thickening, described in section 3.5.4 gives as result the surface density or the number of tongues per mm^2. This evolution is presented in Fig. 5.9. In addition, the regime limits found by the thickness evolution analysis T_1, T_2 and T_3 are drawn in this plot. One can remark that these limits also correspond to a change in regime for tongue thickening. As a first approximation, two plateaus P_1 and P_3 are visible and are shown by horizontal red

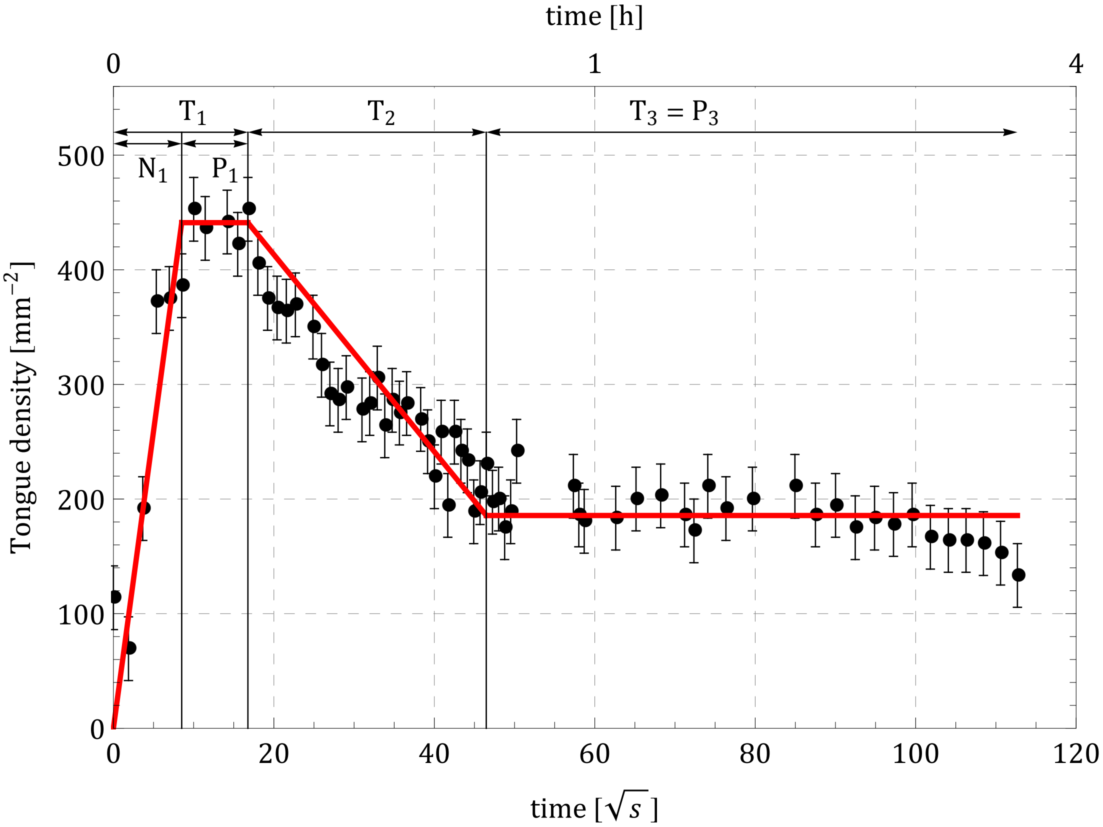

Figure 5.9: Tongue density evolution with time with: N_1 emergence step, P_1 first stabilization, T_2 thickening and P_3 second stabilization. Note that domain limits are the same than determined by intermetallic thickness evolution in Fig. 5.8.

lines in the plot. Mean values in the respective domains are used to draw these horizontal lines. The first plateau P_1 corresponds to the end of regime T_1 while the second one P_3 corresponds to the regime T_3. The line at the very beginning joins the origin to the first point of the plateau P_1. The one in T_2 joins the the last point of P_1 to the first of P_3.

This first evaluation allows to highlight the different thickening modes. The increase at the very beginning of the reaction is interpreted as the rapid emergence of tongues. They are growing independently towards the iron matrix until they occupy the whole surface of the initial iron. Then, as no new tongue can form, they progressively thicken during T_2. Thus, thickening mainly occurs during this regime and then stabilizes in P_3.

Fig. 5.10 presents the three-dimensional reconstruction of the tongues when (a) tongue density reaches the plateau P_1, (b) at the beginning of the transition regime T_2 and (c) at the end of T_2. In Fig. 5.10 (a) one can observe in the red circle a part of the initial surface that did not react at this time. The rapid increase in N_1 is observable because the emergence was progressive on the iron surface, due among others to the oxide layer presented in section 5.1. If this one would

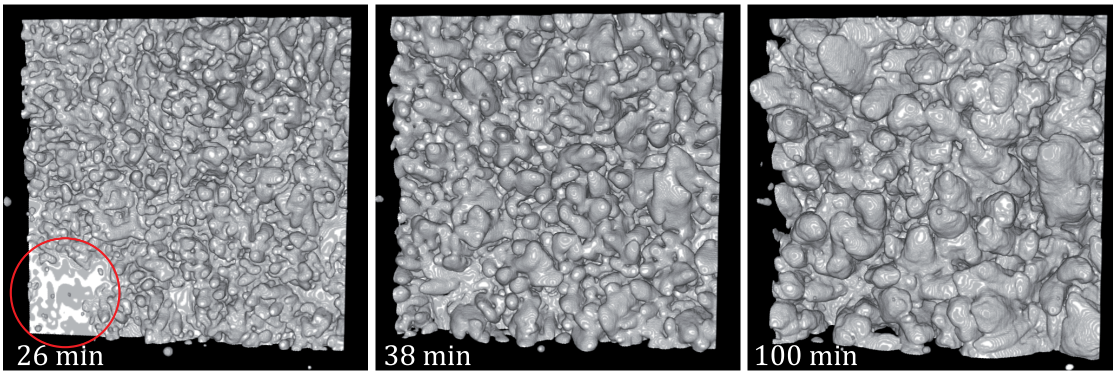

(a) Beginning of P_1 (b) Beginning of T_2 (c) End of T_2

Figure 5.10: 3D reconstructions of the intermetallic tongues at the defined regime limits: (a) End of nucleation (beginning of P_1), (b) Beginning of thickening (end of P_1), (c) End of thickening (beginning of P_3).

be homogeneous, the slope of the increase in N_1 would tend to infinite. It implies that P_1 corresponds to the homogenisation period at the end of which the whole surface is occupied by tongues and no more tongue formation occurs. Note that although a separation between the emergence (N_1) and the thickening (T_2) is made here, it does not prevent thickening to start earlier. As one can see, tongues are already thicker in Fig. 5.10 (b) than in (a).

Considering only the thickening behaviour of regime T_2, measurement were fitted to describe the density decrease as a function of the square root of time. The best fit was given by the following equation:

$$\rho_T(t) = 104.15 + \frac{5600.6}{\sqrt{t}} \qquad [\mathrm{mm}^{-2}] \qquad \text{for } t \in \mathrm{R}_T \tag{5.3}$$

This fit is presented in red in Fig. 5.11 together with the data taken into account in red. The fit of the density in T_2 gives different informations on the behaviour. First of all, its dependence to the square root of time shows that thickening probably behaves, as well as the intermetallics growth. A fit corresponding to a coarsening (n.b. $\rho \propto t^{1/3}$) is not representing the thickening behaviour. Furthermore, its extension in T_3 does not diverge more than the measurement error and thus one can consider that thickening still operates in the latter. One can interpret this as a competition between the two growth directions: along the main axis making tongues longer and perpendicular to this direction, making the tongues thicker. At the very beginning (T_1), as shown in chapter 6, the main direction is favoured. Thickening is delayed until the beginning of T_2, due to the homogenisation of the reaction on the sample surface. Then, thickening is rapid at the beginning of T_2 and progressively tends to a constant value for times tending to infinite, explaining the rather stability during T_3.

Mullins and Sekerka, who worked on the dendrite solidification (section 2.4), obtained the marginal stability criterion predicting that λ multiplied by the velocity v is equal to a constant

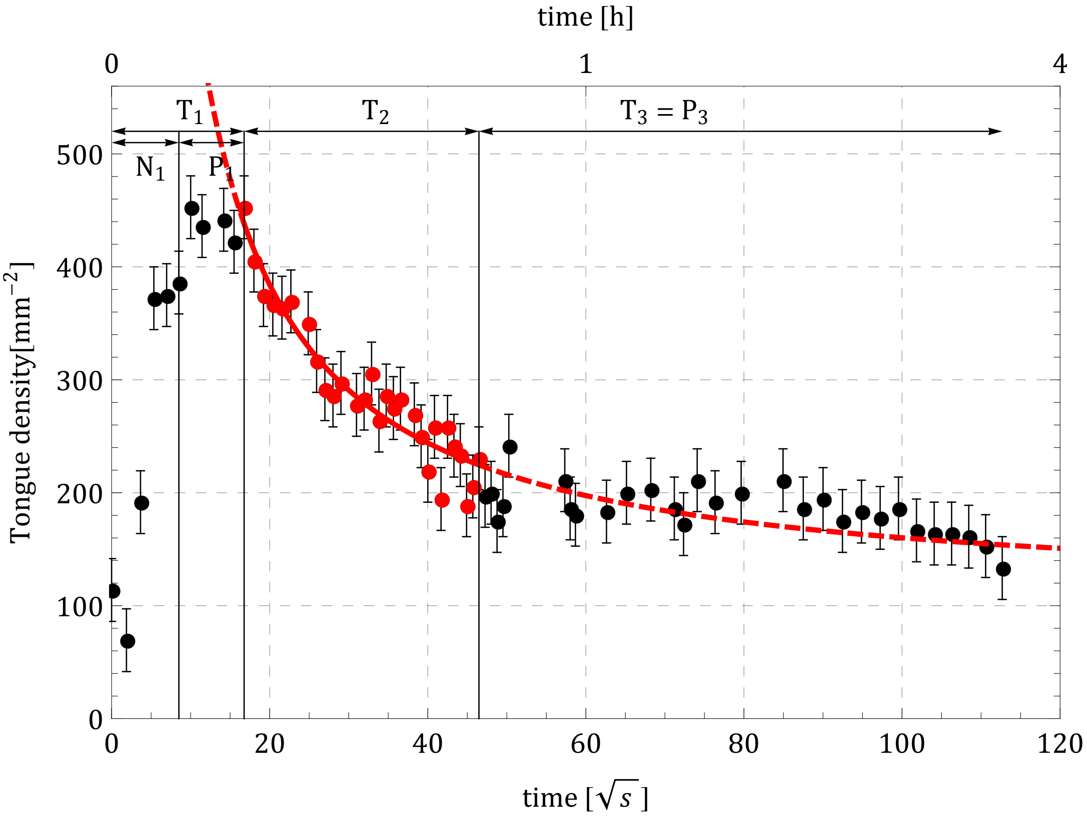

Figure 5.11: Tongue thickening as a function of the square root of time. In red, measured values taken into account for fitting data during regime T_2 given by Equ. 5.3. Dashed red line corresponds to the extension of the fit in T_1 and T_3 regimes.

for a destabilised interface.

$$\lambda^2 \times v = \text{cst.} \tag{5.4}$$

With this equality, as the velocity is proportional to the inverse of the the square root of time, λ^2 should be proportional to the square root of time

$$v \sim \frac{1}{\sqrt{t}} \qquad \rightarrow \qquad \lambda^2 \sim \sqrt{t} \tag{5.5}$$

As the square of the mean distance between tongues is given by the inverse of the tongue density, the latter should effectively vary with the inverse of the square root of time.

$$\lambda^2 = \frac{1}{\rho_T} \qquad \rightarrow \qquad \rho_T \sim \frac{1}{\sqrt{t}} \tag{5.6}$$

This implies that the front is strongly destabilised at the very beginning of the reaction and then the mean spacing adapts (increases) with velocity decreasing. The assumption of the front destabilisation is the subject of chapter 6, which goes a bit further in the development. However, this previous result shows that competition between tongue growth and thickening occurs during regime T_2. Furthermore, the matrix recrystallisation that has been observed in section 4.2 will promote diffusion in the iron matrix between tongues and thus favour thickening.

5.6 Interface position

Fig. 5.12 presents the positions of the solid – liquid interface, of the tongues – iron matrix interface and of the dense intermetallics – tongues interfaces determined by area fraction method as a function of time (section 3.5.3). These positions were measured relatively to the initial Fe – Al interface at position 0, with iron in the negative part and aluminium in the positive one. In addition, the interface positions obtained by the simulation with the apparent diffusion coefficients of table 5.2 are given as dashed lines and the regime limits are marked by arrows.

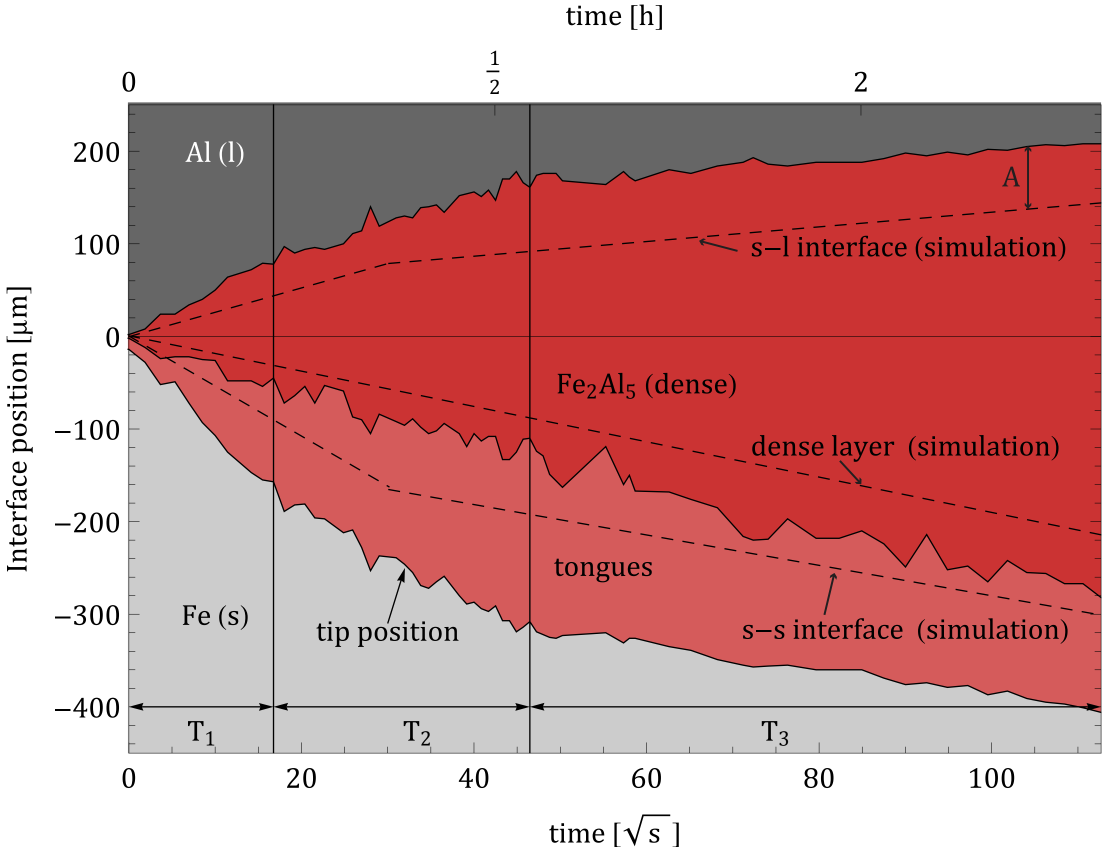

Figure 5.12: Interface position with time relative to the initial solid – liquid interface in *in situ* horizontal observation.

The rapid growth at the beginning is especially visible on the solid side and corresponds to the rapid emergence of the tongues. On the other side, the interface movement is due to the direct growth and also to the deformation of the system induced by the tongue penetration into the matrix (section 2.3.2). Then in T_2 the thickening effect becomes observable by a the flattening of the tongue tip position (arrow). One can see that on the liquid side the velocity also decreases during this regime. Then, entering in T_3, competition between growth and thickening still occurs although it is hardly visible at the measurement scale. It can be seen by the slight convergence of the dense part and the tip positions during T_3. For time tending to infinite, the dense part will catch the tongues and then the growth will finally reach its steady state regime.

Simulations of the two regimes undervalue both interface positions. On the solid side, as the model is considering a planar front growth, the simulation result should be compared to a medium position between tongues and dense part. Indeed, the measured interface position does not take into account that in the tongue domain (lighter red) tongues do not occupy the whole volume thus the model is not representative of this position. Simulation of the dense layer - tongue interface, albeit a slight shift is observed, is well representing the layer growth. Thus, the dense layer evolves as a planar front and this simulation is used in chapter 6 to determine the velocity of the stable interface in the studied cases.

On the liquid side, although dissolution is not taken into account in the simulation, the calculated thickness is also smaller than the measured one. However, as already observed, the global calculated thickness (Fig. 5.8), which corresponds to the difference between the two interface positions (dashed lines), is well evaluated by the model. It has to be remembered that a density change is taken into account in the calculation and thus the difference here is not due to calculation artefact. Thus, the difference between the calculated and the measured liquid – solid interface, given by the double arrow A, is interpreted as the effect of the deformation experienced by the system and presented in section 4.2.3.

Finally, solving the equality between equations giving the intermetallic thicknesses for dense part and for tongues shows that the latter should be caught by the dense layer after about 52 h of contact. This time corresponds to the transient period before a planar front growth is established if the system is still supplied with aluminium and iron.

5.7 Summary

The measurements performed on the different test configurations allowed to bring out the effect of the main phenomenon influencing the measurement: the bath saturation and the curvature of the initial interface. The horizontal sample observed *in situ* allowed limiting the effect of both of those effects. It was thus chosen for further analysis. Three main regimes were found during the latter.

T_1 corresponds to the very beginning when tongues are emerging and rapidly growing (N_1, images 1 to 3 in Fig. 5.1) in the iron matrix until they occupy the whole initial surface (P_1, images 3 to 5 in Fig. 5.1).

T_2 corresponds to the transition regime recognisable in the intermetallic thickness measurement by a variation in growth constant. It corresponds to the period when thickening is the most active and comes into competition with the main growth direction (images 5 to 9 in Fig. 5.1).

T_3 corresponds to a more regular growth, recognisable by the convergence of the dense part and the tongue tip position in Fig. 5.12 that should meet after 52 h leading to a steady state growth. Fig. 5.1 9 to 12 correspond to this regime.

Now that the different regimes are explained by the effect of the tongues, one question subsists, which is the reason of the destabilisation and the emergence of the tongues. This subject is discussed in chapter 6, which focuses on the very beginning of the reaction (T_1), when tongues are rapidly forming.

6 Interface destabilisation

This chapter tries to explain the tongues development at the beginning of the growth. As it was found in the previous chapter, there are two different growth regimes, each one with its own apparent diffusion coefficients. This implies a difference in aluminium flux between the first regime at the beginning of the process (T_1) and the second regime, called the regular regime (T_3).

The following development assumes that at the beginning of the reaction (T_1) aluminium supply of the interface J_η is much larger than the one in iron J_α. With this assumption the planar front growth in the steady state regime of η is described in section 6.2. Then an artificial destabilisation is added thanks to the analysis based on the Mullins – Sekerka approach presented in section 2.4. Section 6.4 presents the application of the criterion. Growth of the stable front description uses results from the one-dimension numerical model presented in section 3.6.

6.1 System description

As already presented, η-Fe_2Al_5 is the main intermetallics growing in the system and is the one that destabilises. For simplification it is assumed that only this phase is growing in the solid iron. Free energy curves calculation presented in section 2.5.1 allows to build the simplified Fe – Al phase diagram with the two initial phases α and L and the intermetallic phase η. One representation is given in Fig. 6.1. As free energy curve of Al was calculated only for the liquid state, the lower temperature limit of the simplified Fe – Al phase diagram is the Al melting point. For a given temperature, the following parameters are defined:

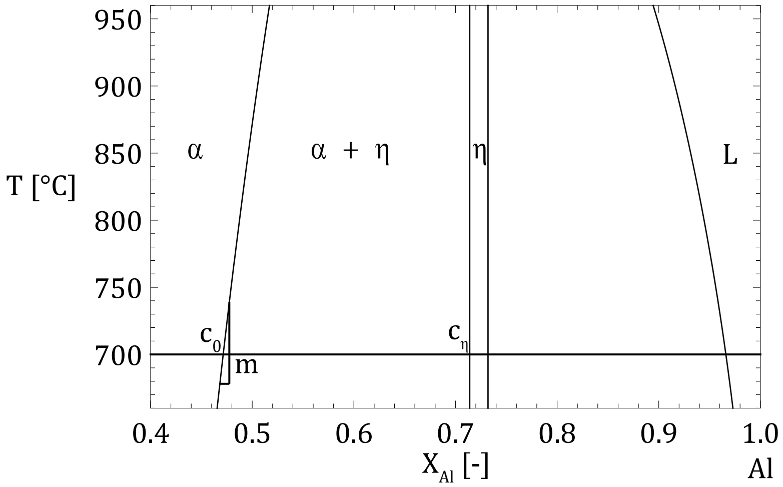

Figure 6.1: Simplified Fe-Al phase diagram deduced from free energy curves of the pure elements and the Fe_2Al_5 intermetallic phases

- $m = \frac{\partial T}{\partial c}$, the slope of the equilibrium line between α and $\alpha + \eta$ domains.
- c_0, the concentration at the interface between α and η phases in the α phase.
- c_η, the concentration of the η phase, considered as stoichiometric.

The analysis considers the growth of η in α without taking into account the initialisation and thus the nucleation stage.

6.2 Steady state regime

6.2.1 Concentration profile in Fe

The interface between α and η is schematically presented in Fig. 6.2. The steady state concentration profile of Al in α is described as a solution of Fick's second law, given in one dimension

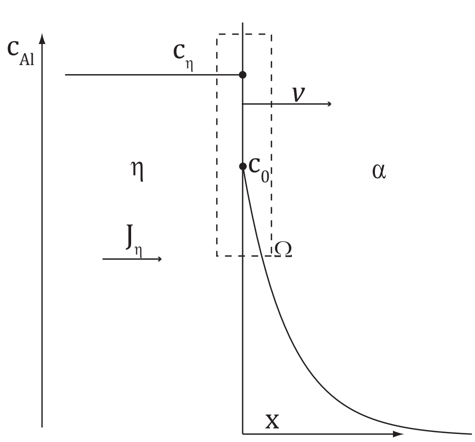

Figure 6.2: Al concentration profile during the growth of a η planar front in α (right), with v the interface velocity, J_η the flux of Al through η and Ω a small volume element across the interface.

by:

$$v\frac{\partial c}{\partial x} = -D\frac{\partial^2 c}{\partial x^2} \tag{6.1}$$

Note that for simplification, indices are suppressed and thus D is the diffusion coefficient of Al in Fe (α) and v the interface velocity. Considering that the referential follows the interface ($x = 0$ at the interface) and that far away from this one Al concentration is null, the steady state concentration $c_\alpha(x)$ can be described as follow:

$$c_\alpha(x) = c_0 \exp\left(\frac{-vx}{D}\right) \tag{6.2}$$

This profile description considers thus a well defined steady state regime. Note that this is obviously not the case in the present system as discussed in chapter 5. The impact of that assumption will be discussed at the end of the present chapter.

6.2.2 Solute balance at the interface

The solute balance at the interface is obtained from the general equation of solute balance on a unitary volume Ω placed in the interface (see Fig.6.2) and described in Equ.6.3. This formulation takes into account the variation with time of the concentration (first integral), the transport term (second integral), the flux term (third integral) and a source term $\dot{Q}$.

$$\frac{d}{\mathrm{d}t}\int_\Omega c_\nu \mathrm{d}V + \int_\Omega \mathrm{div}\left(c_\nu\left(\vec{v}_\nu - \vec{v}\right)\right)\mathrm{d}V + \int_\Omega \mathrm{div}\left(\vec{J}_\nu\right)\mathrm{d}V = \int_\Omega \dot{Q}\mathrm{d}V \tag{6.3}$$

with $\nu = \alpha, \eta$ the phase indexes and $\vec{v}_\nu$ phases velocities. When the thickness of Ω tends to zero, only the transport and the flux terms remain. Using the divergence theorem, the solute balance becomes:

$$\int_{\partial\Omega} c_v \left(\vec{v}_v - \vec{v}\right) \vec{n} \mathrm{d}S + \int_{\partial\Omega} \vec{J}_v \vec{n} \mathrm{d}S = 0 \tag{6.4}$$

with $\vec{n}$ the unit normal to the surface $\partial\Omega$. One can integrate Equ. 6.4. Taking into account that phases velocities are null,neglecting the difference in densities, and that $J_\eta >> J_\alpha$, one obtains:

$$v\left(c_\eta - c_0\right) = -J_\alpha + J_\eta \tag{6.5}$$

Taking into account the definition of the flux in α:

$$J_\alpha = -D \left.\frac{\partial c}{\partial x}\right|_{x=0} = -D \frac{-c_0 v}{D} \tag{6.6}$$

one finally obtains the flux in η

$$J_\eta = v c_\eta \tag{6.7}$$

In other words, the solute balance at this interface is given by:

$$-v c(x) = -D \left.\frac{\partial c(x)}{\partial x}\right|_{x=0} \tag{6.8}$$

At the beginning of the reaction, the interface velocity v is proportional to $\frac{1}{\sqrt{t}}$ and is thus theoretically infinite. In other words, the flux J_η is infinite and can provide any amount of Al to the interface as seen in Equ.6.8.

Therefore, at the beginning, the growth of the interface is limited by diffusion of Al in the iron phase. Thus, any perturbation of the interface will tend to be amplified as it is easier to diffuse Al in iron with a tongue compared to a planar front. In other words, a given volume of iron in front of the interface only accepts a small amount of aluminium, which limits the growth. Increasing the surface allows the system, with the same volumes, to increase the amount of aluminium that goes in iron as the exchange surface is larger.

On the opposite, for long reaction times, the thickness of the intermetallics is large and the velocity of the interface tends towards zero and thus J_η becomes small. Therefore, the intermetallic growth tends to be controlled by J_η and thus the interface tends to be stable. In other words, as diffusion in η becomes more difficult and as the tongues have a larger extension compared to the valleys, their growth is lower than the one of the valleys.

In the next section a stability analysis is performed, assuming that $J_\eta >> J_\alpha$ and thus that growth and thus stability is controlled by diffusion of aluminium in iron.

6.3 Destabilisation

6.3.1 Concentration profile in Fe

The following calculation follows closely the derivation of Mullins. The interface presented in Fig. 6.2 is destabilised in y dimension. As an approximation, the destabilisation is a sinusoidal of amplitude ϵ and wavelength λ, as presented in Fig.6.3 (b). The concentration at the interface

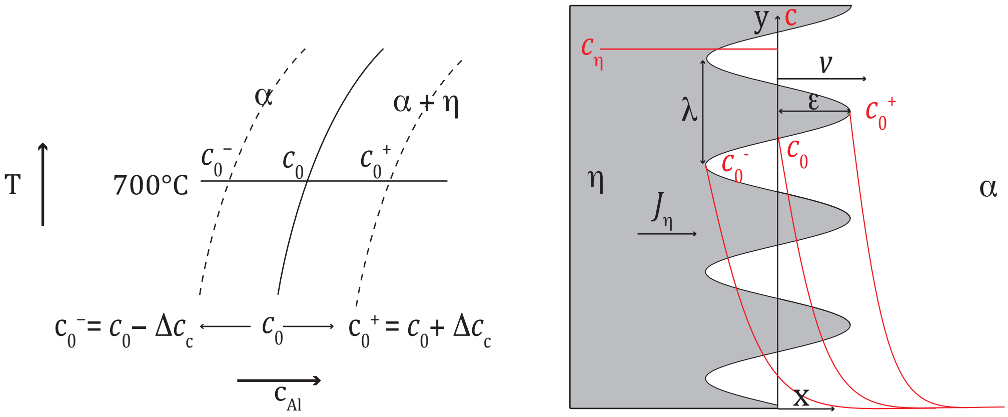

(a) (b)

Figure 6.3: Destabilised interface. (a) Shift of the equilibrium line between α and $\alpha+\eta$ due to the curvature of the interface: c_0^- effective interface concentration in a valley, c_0^+ effective interface concentration at a tip. (b) Schema of Al concentration profiles (red) in α for a destabilised interface.

c_0 is modified by the curvature effect that locally shifts the equilibrium line between α and $\alpha+\eta$ (Fig. 6.3 (a)) to c_0+ on tips and to c_0- on valleys. Δc_c is the concentration shift and will be defined in section 6.3.2. Taking into account this oscillation, the concentration profile in front of the interface is defined as follow:

$$\tilde{c}(x,y) = c_\alpha(x) + a\epsilon\sin(\omega y)\exp(-bx) \tag{6.9}$$

with $\omega = \frac{2\pi}{\lambda}$ the pulsation of the oscillation and a and b parameters to determine. Furthermore, the position of the destabilised interface x^* can be described as a parametric function $S(y)$

$$x^* = S(y) = \epsilon\sin(\omega y) \tag{6.10}$$

Using Fick's second law in two dimensions (Equ.6.11), with the profile in α (Equ.6.9), and considering that D is independent of the concentration, one obtains after simplifying Equ.6.12.

$$D\left(\frac{\partial^2 c}{\partial x^2}+\frac{\partial^2 c}{\partial y^2}\right)+v\frac{\partial c}{\partial x}=0 \tag{6.11}$$

$$a\,S(y)\exp(-bx)\underbrace{\left(Db^2-D\omega^2-bv\right)}=0 \tag{6.12}$$

$$b=\frac{v}{2D}+\sqrt{\left(\frac{v}{2D}\right)^2+\omega^2} \tag{6.13}$$

The second term of Equ. 6.12 (brace) gives Equ.6.13 as solution for b.

6.3.2 Curvature calculation

The curvature of a parametric curve $S(y)$ is mathematically defined by the first equality of Equ.6.14. Assuming that oscillations are small ($\frac{\partial S}{\partial y} << 1$), the curvature of the interface can be approximated as the second derivative of $S(y)$:

$$\kappa=\frac{\frac{\partial^2 S}{\partial y^2}}{\sqrt{\left(1+\left(\frac{\partial S}{\partial y}\right)^2\right)^3}}\approx\frac{\partial^2 S}{\partial y^2}=-\omega^2\epsilon\sin(\omega y)=-\omega^2 S(y) \tag{6.14}$$

With this definition, the curvature κ of the η phase is positive for a tongue tip and negative for a valley. Therefore, concentration at the destabilised interface $\tilde{c}(x^*,y)$ must be equal to the concentration of the planar interface plus the curvature term.

$$\tilde{c}(x^*,y)=c_0+\Delta c_c=c_0+\frac{\Gamma_{\alpha\eta}\kappa}{m} \tag{6.15}$$

with m the slope of the equilibrium curve and $\Gamma_{\alpha\eta}$ the Gibbs-Thomson coefficient, that takes into account the excess in free energy due to the surface between the two phases [89] and is defined as follow:

$$\Gamma_{\alpha\eta}=\frac{\gamma_{\alpha\eta}}{\rho\Delta S^{vol}} \tag{6.16}$$

with $\gamma_{\alpha\eta}$ the interfacial energy between α and η, ρ the density of η and ΔS^{vol} the volumetric entropy of η. As not many data exist for the phase transformation $\alpha + Al(l) \rightarrow \eta$, the Gibbs-Thomson coefficient was estimated as $10^{-7}\,\mathrm{K\cdot m}$.

6.3.3 Parameter a

Taking into account Equ.6.9, replacing x^* by its parametric description S and κ by its approximation of Equ.6.14, one obtains the following equation:

$$c_0\, exp\left(-\frac{vS}{D}\right) + a\, exp(-bS)S + \frac{\Gamma_{\alpha\eta}\omega^2 S}{m} = c_0 \tag{6.17}$$

Considering small oscillations, an approximation of the exponential factor can be done as follow: if $|x| << 1$ then $\exp(-x) \approx 1 - x$. Ignoring second order terms of S, the parameter a can be evaluated. One also recognizes that the first term corresponds to G_c, the chemical gradient in α, Equ. 6.17 can be rewritten as:

$$a = \frac{c_0 v}{D} - \frac{\Gamma_{\alpha\eta}\omega^2}{m} = -G_c - \frac{\Gamma_{\alpha\eta}\omega^2}{m} \tag{6.18}$$

6.3.4 Stability criterion

The local interface velocity v^* is defined in Equ.6.19 and takes into account the global velocity v plus the local variation with time as follows:

$$v^* = v + \frac{dx^*(y)}{dt} \tag{6.19}$$

With this velocity and as the concentration profile for the destabilised interface is fully defined by Equ. 6.9, and the parameters a (6.18), and b 6.13, the solute balance found in Equ. 6.8 at the interface can be written as follows:

$$-v^*\tilde{c}(x^*, y) = D\left.\frac{\partial \tilde{c}}{\partial x}\right|_{x^*} = 0 \tag{6.20}$$

Replacing x^* by its parametric description S in Equ.6.19 one obtains:

$$v^* = v + \frac{\dot{\epsilon}}{\epsilon}S \tag{6.21}$$

that can be inserted in Equ. 6.20, as well of the expression of $\tilde{c}$ and $\left.\frac{\partial \tilde{c}}{\partial x}\right|_{x^*}$ with the parametric description S and gives:

$$-(v + \frac{\dot{\epsilon}}{\epsilon}S)\left(c_0 - \frac{c_0 vS}{D} + aS(1-bS)\right) = D\left(-\frac{c_0 v}{D} + \frac{c_0 v^2 S}{D} - abS(1-bS)\right) \tag{6.22}$$

Simplifying Equ.6.22 and neglecting second order terms of S, zero order terms cancel each other and one obtains the following equation:

$$S\left(a(bD - v) - \frac{\dot{\epsilon}}{\epsilon}c_0\right) = 0 \tag{6.23}$$

from which one can express $\frac{\dot{\epsilon}}{\epsilon}$, dividing by S and replacing a by Equ: 6.18:

$$\underline{\underline{\frac{\dot{\epsilon}}{\epsilon} = \frac{1}{c_0}(bD - v)\left(\frac{c_0 v}{D} - \frac{\Gamma_{\alpha\eta}\omega^2}{m}\right)}} \tag{6.24}$$

This equation represents the stability criterion of the present system with its control parameter $\frac{\dot{\epsilon}}{\epsilon}$. Indeed, a positive ratio means that the amplitude velocity has the same sign as the amplitude, thus the same orientation, which tends to increase the amplitude itself. In summary, if $\frac{\dot{\epsilon}}{\epsilon} > 0$, the interface is unstable. The tongue will grow further in the matrix when both have positive signs while the valley will go back in direction of η when both have negative signs.

6.4 Criterion application

The evaluation of the front stability is performed considering the values at 700 °C presented in table 6.1 (Case 1). In addition, three cases (2 to 4) are also evaluated. Case 2 corresponds to the same system but with a diffusion coefficient of aluminium in iron artificially increased to a value ten times higher than the one from the literature of $1.9 \times 10^{-17}\,\mathrm{m}^2 \cdot \mathrm{s}^{-1}$. Case 3 corresponds to the system with diffusion coefficient hundred times higher than Case 1 and Case 4 corresponds to the system at 800 °C.

Table 6.1: Parameters used to evaluate the destabilisation criterion in four different cases: (1) studied system, (2) system with diffusion coefficient of Al in Fe ten times higher, (3) system with diffusion coefficient of Al in Fe hundred times higher, (4) system at 800 °C.

	Case 1	**Case 2**	**Case 3**	**Case 4**	**Unit**	**Ref**
Feature	700 °C	$10 \times D$	$100 \times D$	800 °C		
c_0	0.471	0.471	0.471	0.487	-	Fig.6.1
c_η	0.72	0.72	0.72	0.72	-	Fig.6.1
m	6552.8	6552.8	6552.8	5945.1	K	Fig.6.1
v	5.47×10^{-7}	5.48×10^{-7}	5.52×10^{-7}	2.58×10^{-6}	$\mathrm{m \cdot s^{-1}}$	model (5 s)
D	1.9×10^{-17}	1.9×10^{-16}	1.9×10^{-15}	1.5×10^{-15}	$\mathrm{m^2 \cdot s^{-1}}$	[6]
$\Gamma_{\alpha\eta}$	10^{-7}	10^{-7}	10^{-7}	10^{-7}	K·m	approx.

Interface concentrations and slopes are obtained from the modified phase diagram presented in Fig. 6.1.

Interface velocity in the steady state regime is estimated from the one-dimensional model, with the apparent interdiffusion coefficient for the dense intermetallic layer given in Fig. 5.8. At 800 °C, the interdiffusion coefficient in Fe_2Al_5 is estimated from Kajihara's fit (table 5.2 and Fig. 5.8) [40]. Although Kajihara's measurements were performed at temperatures below the melting point, the fit describes well the growth of the dense layer at 700 °C in Fig. 5.8 and thus it is assumed this is also the case at 800 °C.

One remarks in table 6.1 that the steady state regime from which velocities are extracted is only hardly affected by the diffusion in iron as v only slightly varies between cases 1, 2 and 3. On the contrary, at 800 °C interface velocity is larger due to the kinetics increase.

Fig. 6.4 (a) presents the stability criterion of the interface in the present system (Case 1, red), in a system with a diffusion coefficient ten times larger (Case 2, gray) and with a diffusion coefficient hundred times larger (Case 3, black). One can first remark that the marginal stability $\lambda_{i/1}$ ($\frac{\dot{\epsilon}}{\epsilon} = 0$) for the studied system (Case 1) is of about 2×10^{-10} m. In order to verify the consistency of the model, an evaluation of this value can be done by comparison with the dendritic growth in solidification (for the liquid state). In the latter, λ_i is of the order of the micrometre. Equ. 2.39 shows that for equivalent systems, λ_i is proportional to the square root of the ratio between the diffusion coefficient and the interface velocity. Thus, knowing that dendrite velocity in liquid is in the order of magnitude of 100 µm · s^{-1} with a diffusion coefficient of about 10^{-9} m^2 · s^{-1} [22], one can estimate the ratio between the two marginal

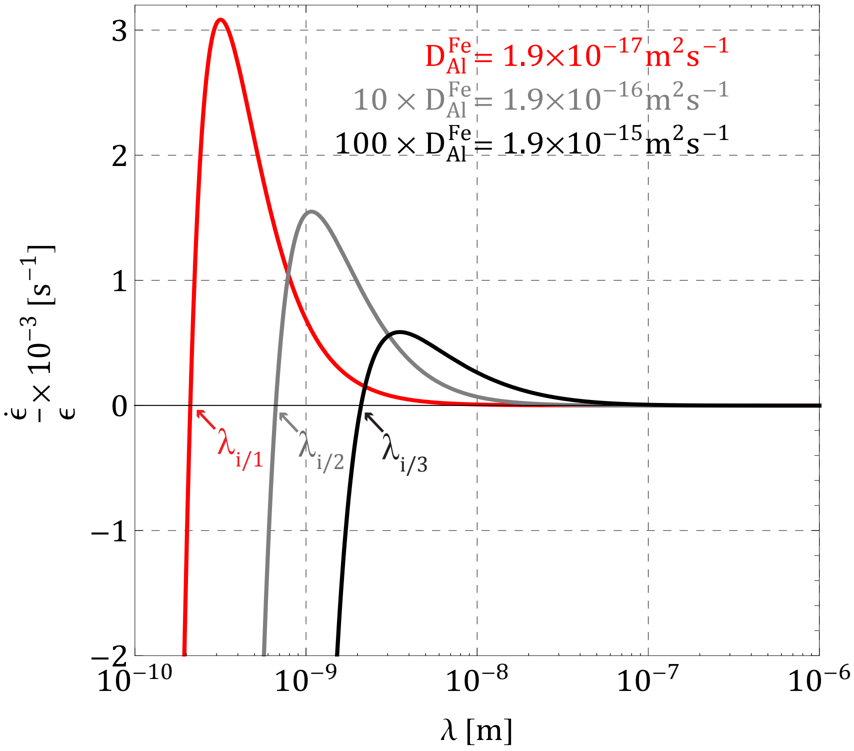

Figure 6.4: Stability criterion as function of the mean distance between tongues or (wavelength) λ : growth of η-Fe$_2$Al$_5$ in pure iron in contact with Al at 700 °C (Case 1, red) and in phases with an artificially increased Al diffusion in Fe: ten times higher than the real value (Case 2, gray) and hundred times higher (Case 3, black).

stabilities, with d index referring to dendrite and η to the present case:

$$\frac{\lambda_{i,\eta}}{\lambda_{i,d}} \approx \sqrt{\frac{D_\eta \times v_d}{D_d \times v_\eta}} \approx \sqrt{\frac{10^{-17} \times 10^{-4}}{10^{-9} \times 10^{-7}}} \approx 10^{-3} \tag{6.25}$$

This ratio is approximately 10^{-3}, which means that instabilities that develop in the present system are thousand times smaller than the ones leading to dendrite formation. Thus this rough approximation shows that indeed instabilities length period is between the Ångtroem and the nanometre, which corresponds to the calculated one $\lambda_{i/1}$.

It has to be noted here that this instability is calculated at the very beginning of the reaction and thus the interface will evolve with time, as it was shown by Somboonsuk *et al.* who worked on dendritic solidification pattern by observing succinonitrile alloys [90]. In particular, they presented the evolution of a destabilised interface with time, see Fig. 6.5. In this figure one can see that indeed for longer times the dendritic structure is not related anymore to the initial interface destabilisation described by the linear stability analysis. Thus, the calculated λ_i is not directly linked with the effective tongue density experimentally measured, see chapter 5. As tongue thickening is actually operating, it is not possible to describe the tongue structure at a time t with the present modelling of its initial destabilisation.

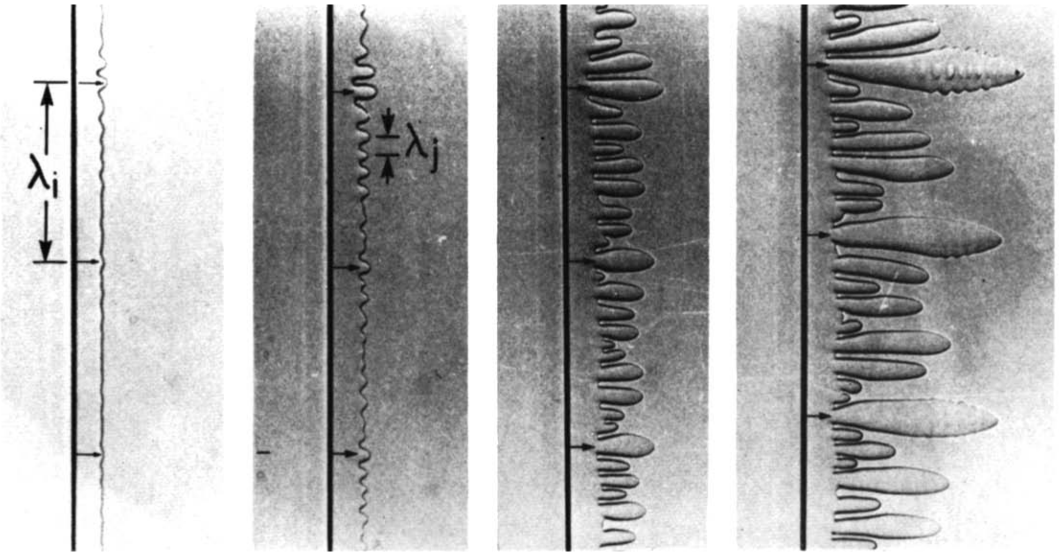

(a) (b) (c) (d)

Figure 6.5: From [90]: Development of solid-liquid interface shapes with time when the applied velocity is changed from 0 to 3.4 ms^{-1} in a directionally solidified succinonitrile-4.0 wt % acetone solution at G =6.7 Kmm^{-1}. The time after the change in velocity are (a) 50 s, (b) 55 s, (c) 60 s, (d) 85 s.

However, the effect of the aluminium diffusion coefficient in iron is clearly observed in Fig. 6.4, for example by the comparison of maximum value of $\frac{\dot{\epsilon}}{\epsilon}$. This value is about 3083 s^{-1} for the

Case 1 while it is about the halved with a coefficient one order of magnitude higher (Case 2) with 1548 s^{-1} and about five times less with a coefficient two orders of magnitude higher (Case 2) with 586 s^{-1} . Furthermore, the marginal stability of the two systems with artificially increased diffusion coefficient are also larger with about 5.5×10^{-8} m and 2.13×10^{-7} m showing that the initial destabilisation is larger and thus that tongue density is lower. Diffusion of aluminium in iron plays thus an important role in the destabilisation of the growth front at the beginning of the reaction.

To complete this analysis, a horizontal test at 800 °C was performed during 30 min. Fig. 6.6 presents micrographies of the interface at 700 °C (a) and at 800 °C (b) and the stability criterion for both temperatures (c). As previously mentioned, the present approach cannot be used

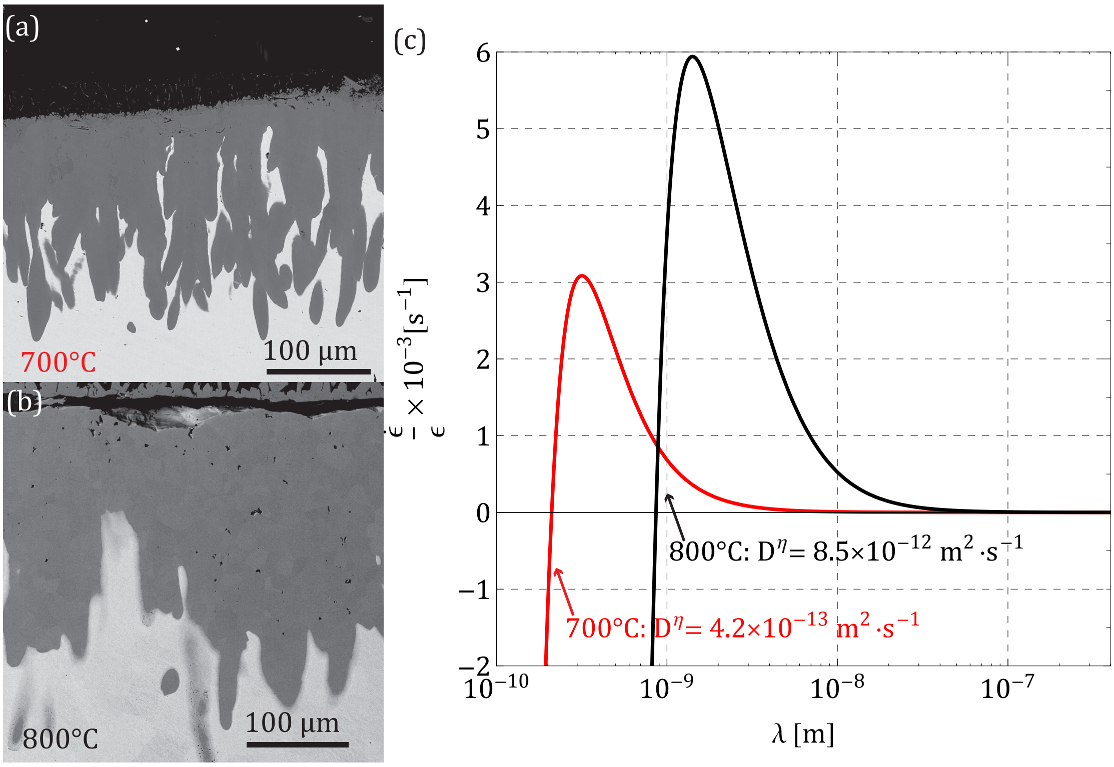

Figure 6.6: SEM (BSE) micrographies of the interface between iron aluminium after a contact of 30 min at (a) 700 °C and (b) at 800 °C.(c) Stability criteria at 700 °C and 800 °C. For 800 °C.

to quantitatively predict the interface shape at time t. However, a simple observation shows that the number of tongues at 800 °C is lower than the one at 700 °C. This is confirmed by the shift to the right of the stability curves. The amplitude is difficult to analyse because the kinetics effects such as tongue thickening are unknown. However, the system does not seem to stabilise with temperature, which is in opposition to Tanaka *et al.* [44].

The micrography of the layer after 40 min of contact at 800 °C from which they conclude that the interface becomes flat above this temperature is presented in Fig. 6.7.

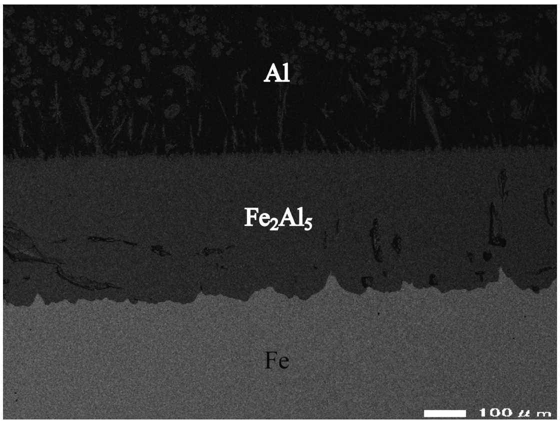

Figure 6.7: From [44]: SEM (BSE) of a cross-section for the Fe/Al diffusion couple annealed at T = 1073 K for t. 2.4×10^3 s

As kinetics is increased at this temperature compared to 700 °C, and as Tanaka's observation is made on a sample that already reaches the regime T_3, one cannot say if the destabilisation occurred at the beginning but was more rapidly stabilised or if no destabilisation at all occurred during this test. The interface shape between Fe_2Al_5 and iron shown in Fig. 6.7 tends to confirm that destabilisation indeed occurred at the beginning but thickening is more efficient in Tanaka's experiments than in the present ones.

However, as in the present situation, destabilisation also occurs at 800 °C with thicker tongues, the destabilisation criterion seems to be in agreement with observations. It has also to be noticed that the rough evaluation of the interdiffusion coefficient in Fe_2Al_5 is an important source of uncertainty.

6.5 Summary

The application of the Mullins-Sekerka approach to the studied system allows to show that the early beginning of the growth is strongly destabilised due to the high aluminium flux difference at the iron interface. Considering the regimes found in chapter 5, the growth can be described as follows:

During regime N_1, the growth is controlled by the diffusion of aluminium in the iron matrix and results in the destabilisation of the interface and thus the rapid emergence of the tongues.

Thicknening starts during regime P_1 and is in competition with the tips growth during regime T_2 until tongues are sufficiently developed or tips sufficiently far from the interface to make the growth being controlled by aluminium diffusion in the layer. This transition corresponds to the limit between regimes T_2 and T_3.

During regime T_3, tongues progressively disappear and interface flattens. This would finally lead to a planar front growth for a longer time that is out of the observation range and estimated in chapter 5 at 52 h.

However, this model has some limitations, especially the one coming from the description of the flat interface by a steady state regimes, which is obviously not the case at the beginning of the reaction. A more detailed analysis of the stability is proposed in the perspectives in chapter 8.

7 Technological Results

Dipping tests and *post mortem* observations were performed on materials for shot sleeve systems of direct interest for the industry, and compared to the pure Fe-Al system studied here.

For the shot sleeve material, two different ferrous materials were considered, namely a ferritic steel 1.2343 and grey cast iron C-31, whose compositions are given in section 3.1. The ferritic steel is the most used material for the shot sleeve while the cast iron is a possible candidate for replacing steel.

For aluminium bath, one alloy was considered, the Silafont-36,commonly used in this industry. Furthermore, this allows to observe the specific effect of Si addition in the system, as other elements present in the Silafont-36 can be neglected.

In addition, different coatings were tested in terms of resistance to liquid aluminium. It was decided to perform those tests in pure aluminium bath as it is the most aggressive liquid [91]. Coatings were all deposited by electroless plating by ATELA in Neuchâtel, Switzerland.

After a brief review of the effect of species addition in the system, section 7.2 presents the results of the microstructural investigation. Section 7.3 presents the results obtained in terms of the quality coefficient defined in section 3.5.6.

7.1 Species addition in Fe – Al system

7.1.1 Melt composition

Kajoch *et al* studied the influence of the aluminium bath composition in contact with Fe on the growth of the Fe-Al intermetallic compounds. He classified them from the greatest to the least tendency of soldering, meaning that intermetallic formation occurs with iron, as follows [91]:

Primary Al > Al-Mg alloys > Hypo eutectic Al-Si alloys > Al-Si-Cu alloys > Eutectic Al-Si alloy

In an eutectic Al-Si alloy, addition of Cr increases the growth rate of the intermetallic compounds, which reaches a maximum at 2.9 wt% Cr. Kwon *et al* [51] also showed that Si addition flattens the interface between Fe_2Al_5 and Fe, thus decreases the tongue-like structure.

7.1.2 Alloying elements

Without modifying directly the microstructure of the steel, some of the elements in solid solution in steel also disturb the intermetallic growth by taking part into their composition. Kwon *et al* remarked that addition of silicon or carbon in the steel flattens the tongue-like structure [51]. Danzo *et al*, working on aluminium coating of electrical steel from different Si grades, reached the same conclusion [63], while Calvillo *et al* observed that adding 3 wt% of Si to an ultra low carbon steel raises the activation energy of the intermetallic phase growth from 71 to $159\,\mathrm{kJ \cdot mol^{-1}}$, showing that the growth was retarded by Si addition [62]. Barbier *et al* comparing the corrosion of a martensitic steel to an austenitic one, concluded that Cr and Ni addition decreases the thickness of the intermetallic phase, Ni being more efficient [54]. Moreover, Ni addition also modifies the morphology, flattening the interface. Balloy *et al* made a review concerning the influence of additions on the Fe-Al interaction [61]. He remarked that Cr or Mo addition do not provide corrosion resistance,contrary to Barbier.

7.1.3 Microstructure

Barbier *et al* studied the corrosion behaviour of two stainless steel, namely a fully martensitic and an austenitic steel [54]. He observed in the martensitic steel a parabolic growth of the Fe-Al intermetallic phases. Balloy *et al* went a bit further in showing that a pearlitic structure has better resistance than a ferritic one. He also showed that graphite lamellae constitute barriers to the diffusion of elements in the matrix and that the more numerous and compact the lamellae, the more resistant the matrix [61]. Addition of aluminium, as it is a graphite promoter when under 5 wt%, provides an improvement to the wear resistance. Furthermore, this addition decreases the chemical potential difference between steel and aluminium, thus decreasing the driving force for intermetallics formation. However, Al also decreases the weight fraction of pearlite, with the lowest pearlitic fraction at 3 wt% Al.

The present investigation focuses on the Si and Cr additions as Si is part of the two technological ferrous material with a composition between 1 and 2 wt % and in the melt with 10 wt %. Cr is part of 1.2343 with 5.3 wt % and only 0.3 wt % in C-31. Note that C-31 contains 3 wt % of C while 1.2343 has 0.4 wt % of it.

7.2 SEM observations

Fig. 7.1 presents results of dipping tests in pure aluminium at 700 °C during 15, 60 and 90 min of the different substrates, namely, pure Fe Armco, ferritic steel 1.2343 and gray cast iron C-31 appearing in medium gray at the interface between Al and the ferritic materials.

7.2.1 Ferrous alloys

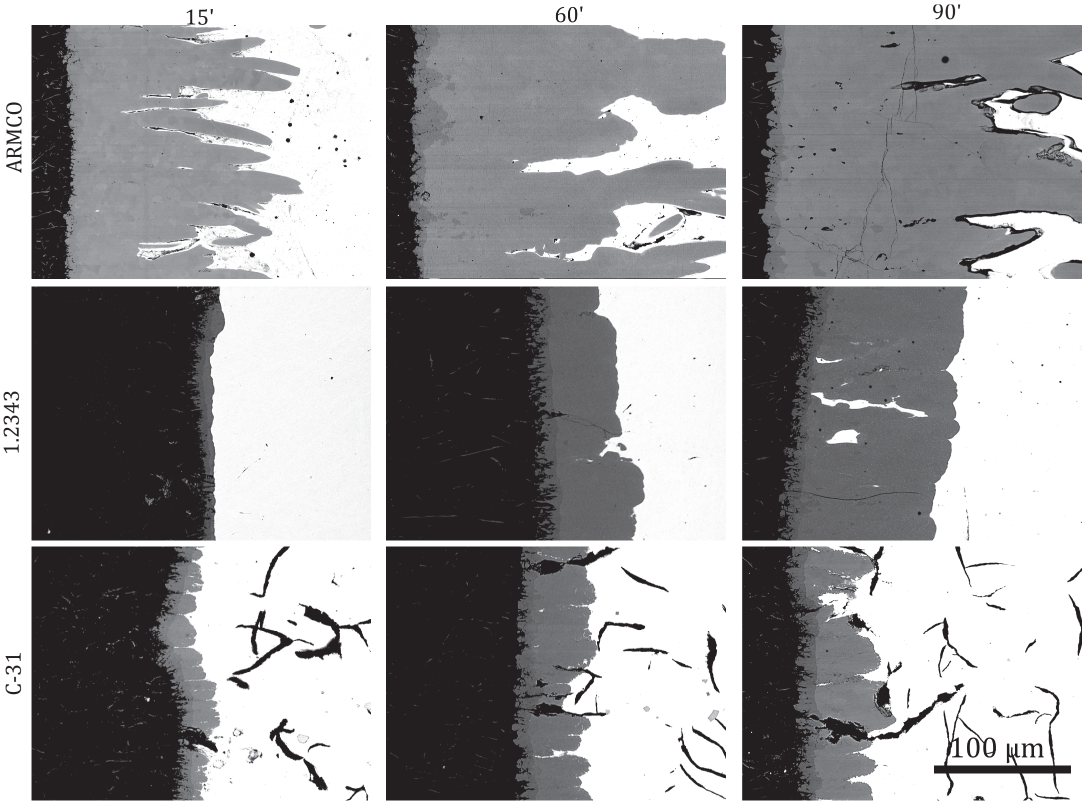

Figure 7.1: SEM (BSE) micrographies of the interface between the three different ferrous substrates in the right and aluminium in the left after dipping tests of 15, 60 and 90 min at 700 °C .

X-ray EDS measurements were performed in the main phase. Results are presented in table 7.1.

There are obvious differences in the morphology of the intermetallic phases and in the way they form. More in detail, both technological present a lower and different reaction to liquid

Table 7.1: Composition of the main intermetallic phase appearing in the three ferrous matrices obtained by W-ray EDS in SEM.

at. %	Al	Si	Cr	Fe
ARMCO	70.9	-	-	29.1
1.2343	72.0	1.9	2.2	23.9
C-31	71.8	1.6	-	26.6

Al than the one of pure Fe. One observes in Fig. 7.1 that intermetallic formation is much faster in pure iron than in the two ferrous metals. Furthermore, the tongue-like feature is less pronounced in them than in pure iron. X-ray EDS results in table 7.1 show that the phase present in the three substrates have a composition close to the one of Fe_2Al_5, with some additions of Si in the cast-iron and some of Si and Cr in the ferritic steel.

In 1.2343 the flattening of the interface is interpreted as the combined effect of Si and Cr additions, as mentioned by Kwon [51] and Barbier [54], respectively.

In C-31 the tongue-like is more pronounced than in 1.2343, which can be due to the absence of chromium. As mentioned in the previous chapters, destabilisation leads to a more rapid growth. Thus the intermetallic layer formed in the C-31 should normally lead to a thicker layer than the one formed in the 1.2343. This is due to the presence of graphite lamellae, which are the black elongated features in the C-31 images in Fig. 7.1 that act as a barrier to Al diffusion and thus slow down intermetallic growth, as mentioned by Balloy *et al* [60].

7.2.2 Aluminium alloy

The result of the interaction between pure iron and Silafont-36 during 60 min at 700 °C is presented in Fig. 7.2 (a). X-ray EDS measurements performed on the different phases labelled as 1, 2 and 3 in the micrography of Fig. 7.2 (a) are reported in the ternary phase diagram calculated by Du *et al* [24] and presented in Fig. 7.2 (b).

Faceted blocks forming on the liquid side (1) have a composition close to the one of $\tau 5$ that corresponds to the composition of the Fe_4Al_{13} phases enriched with Si.

The intermediate compact layer (2) composition is situated close to the Si-enriched Fe_2Al_5 quoted as $\tau 1$, while the third phase (3) exhibiting a slight destabilisation is situated on a conode in the existence domain of $FeAl_2$. These three phases are thus situated in the Al-rich part of the ternary diagram. An additional phase seems to be present in the phase (3) but it was not possible to determine it precisely. Its lighter contrast makes us suppose it corresponds to a phase richer in Fe than the main ones observed in the ternary system.

On the one hand, the phase in contact with iron (3) corresponds to the Si-enriched $FeAl_2$ when the system is enriched with Si. This phase is usually not growing but in rare situations as in

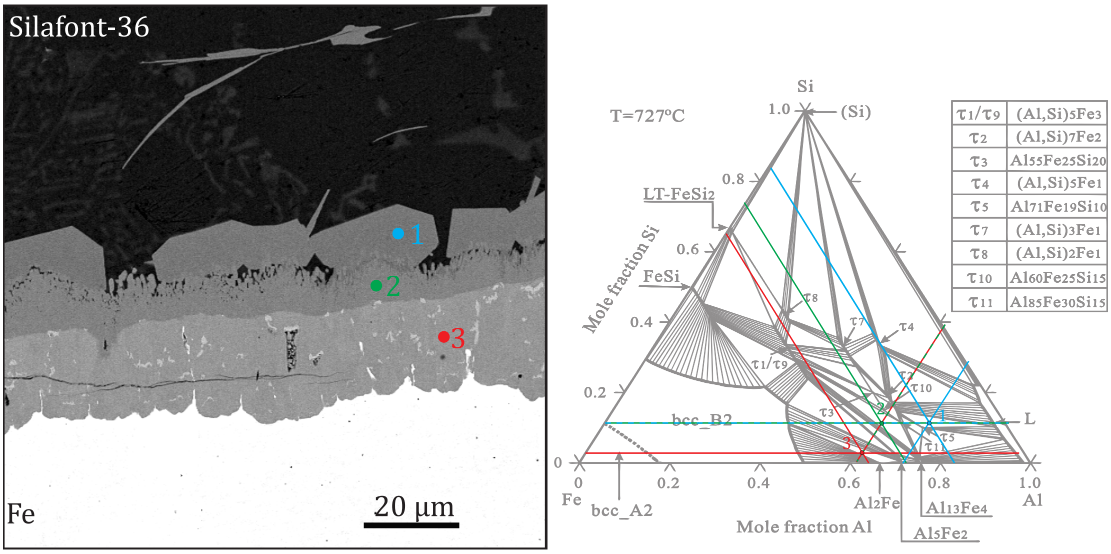
Silafont-36
1
2
3
Fe
20 µm
T=727°C
Si
1.0
(Si)
0.8
LT-FeSi2
0.6
FeSi
Mole fraction Si
0.4
0.2
0
τ8
τ7
τ4
τ1/τ9
τ2
τ10
τ3
τ5
τ11
bcc_B2
L
0
Fe
bcc_A2
0.2
0.4
0.6
Al2Fe
0.8
Al13Fe4
Al5Fe2
1.0
Al
Mole fraction Al
τ1/τ9 (Al,Si)5Fe3
τ2 (Al,Si)7Fe2
τ3 Al55Fe25Si20
τ4 (Al,Si)5Fe1
τ5 Al71Fe19Si10
τ7 (Al,Si)3Fe1
τ8 (Al,Si)2Fe1
τ10 Al60Fe25Si15
τ11 Al85Fe30Si15

(a) (b)

Figure 7.2: (a) SEM (BSE) micrography showing dipping test of pure iron in Silafont-36 during 60 min at 700 °C Resulting in three ternary phases. (b) Ternary Al-Fe-Si diagram at 727 °C [24] with reported X-ray EDS measurements of the locations 1, 2 and 3 marked in (a)

the case of low Al supply, as seen in section4.2.2. One also notices in Fig. 7.2 (a) that this phase is slightly destabilised.On the other hand, $\tau 1$ is compact here although it should present a morphology with tongues, as we have seen in the results for pure Fe and pure Al. Thus, this confirms the assumption that the destabilisation comes from the low diffusion in iron. Indeed, the phase in direct contact with iron, here the Si-enriched $FeAl_2$, is destabilised while the one that usually destabilises, being "protected" by $FeAl_2$ from iron, is rather compact.

7.2.3 Protective coatings

Tests on coated samples were performed in pure aluminium at 700 °C. The objective was to start with usual technology from ATELA using Ni-based materials and test different variants of such coatings. Fig. 7.3 (a) presents the cross-section reconstruction by stitching of SEM (BSE) micrographies of a 1.2343 sample coated with the best variant, a Co-based material, and dipped during 60 min in pure Al at 700 °C. One observes three different regions on the surface

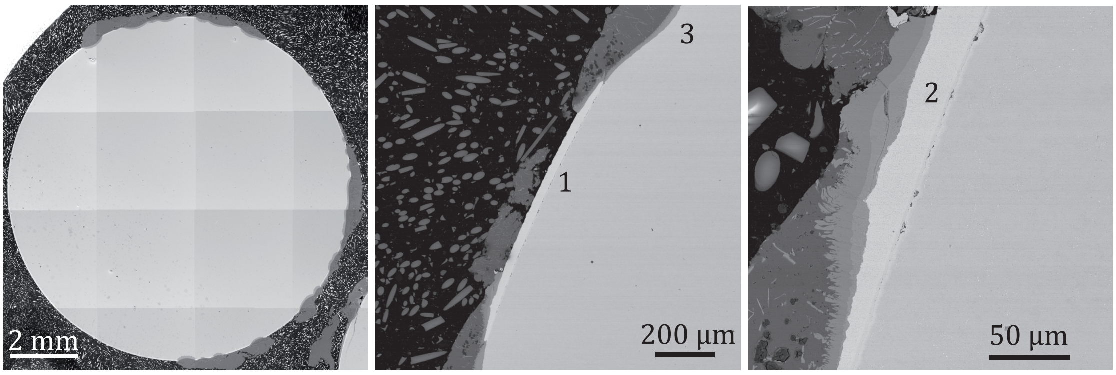

(a) (b) (c)

Figure 7.3: SEM(BSE) micrographies showing the cross section of of a 1.2343 sample coated with a Co-based material and dipped during 60 min into pure Al at 700 °C. (a) General view obtained by image stitching. (b) Micrography at higher magnification showing pristine coating upon which Al did not wet (c) Micrography at higher magnification showing the intermediate compounds resulting from the reaction between coating and liquid Al. The slight contrast below the coating in the iron is the result of coating adhesion during heat treatment.

that was in contact with liquid Al:

1. Non reacted surface, as presented in Fig. 7.3 (b1), where the coating is still observable and some aluminium is sticking on its surface.
2. Surface with partial reaction, as presented in Fig. 7.3 (c2), where the coating is partially removed and replaced by the formation of two intermediate compounds.
3. Reacted surface as presented in Fig. 7.3 (b3), where the coating was totally removed and the intermediate compound grew in the steel matrix.

In general, regions with partial reaction correspond to the transition between the non reacted and the reacted ones. Furthermore, on remarks in 7.3 (a) that reacted regions in the present case look like local pitting.

For the case of the 1.2343 coated with Co, the major part of the coating resisted to the Al contact. Thus, one can conclude that this kind of coating blocks Al diffusion in direction of the steel and does not react with Al. The pitting is interpreted as a defect in the coating that locally weakens the protection and thus allows Al to come into contact with iron, forming intermediate compounds.

As the objective of this chapter is to find the best coating in terms of resistance to aluminium, the formed compounds were not further investigated but focus was made on resistance quantification.

7.3 Quantification

As mentioned in the previous section, a coating needs two properties to protect the ferrous material from iron. It should not react with Al and it should be tight and homogeneous, without defects that could allow Al to diffuse in the ferrous matrix to form compounds. Thus, to quality both properties, the qualify coefficient defined in section 3.5.6 that takes into account the thickness of the formed compound weighted by the ratio between the reacted and the total one was considered. It has to be reminded here that the lower the value of the quality coefficient, the better the resistance.

The coating tests deposited on 1.2343 were performed on three different batches:

Ni-based The first batch of samples was coated with the usual Ni-based material and was considered as the starting point for this investigation.Three different grades of the Ni alloy were tested.

Ni- based + charges The second batch consists in Ni-based materials that were charged with powders of different types of inert materials. Charges were made of aluminium nitride (AlN), alumina (Al_2O_3) and Mo. A sample with a standard Ni-based coating charged in boron with the Bore-Fuse™ paste is added to this batch.

Co-based The third batch consisted in changing the base of the coating, replacing the nickel by cobalt. As this material was for the first time used by ATELA, a first deposition was performed to verify the possibility of using cobalt (Co-1). As the result was promising, two more samples were coated with optimized deposition parameters and tested again in liquid aluminium (Co-2).

Fig. 7.4 presents the quality coefficient as a function of the square root of time for the two different substrates, 1.2343 in black and C-31 in gray, and for the three batches, respectively in red, orange and green. Measurement errors are given by coloured surfaces that also give result domains for each batch. For the substrates without coatings, as the wear is homogeneous, the quality coefficient corresponds to the measured thickness.

For each type of coating, between two and three samples were produced. One was used for qualitative observations of the initial coating and is not reported in the present plot. The second ones was dipped during 90 min into liquid Al at 700 °C. The remaining samples were tested for shorter times, generally 15 or 60 min, to estimate the evolution.

One can remark that the evolution of the intermetallic thickness is more irregular in the cast-iron than in the ferritic steel. This is explained by the presence of graphite lamella in the cast-iron that blocks the intermetallics front growth.

The results obtained with the first batch in red in Fig. 7.4 are all similar and the concentration seems not to play a significant role. Addition of Ni in the system seems to increase the reaction.

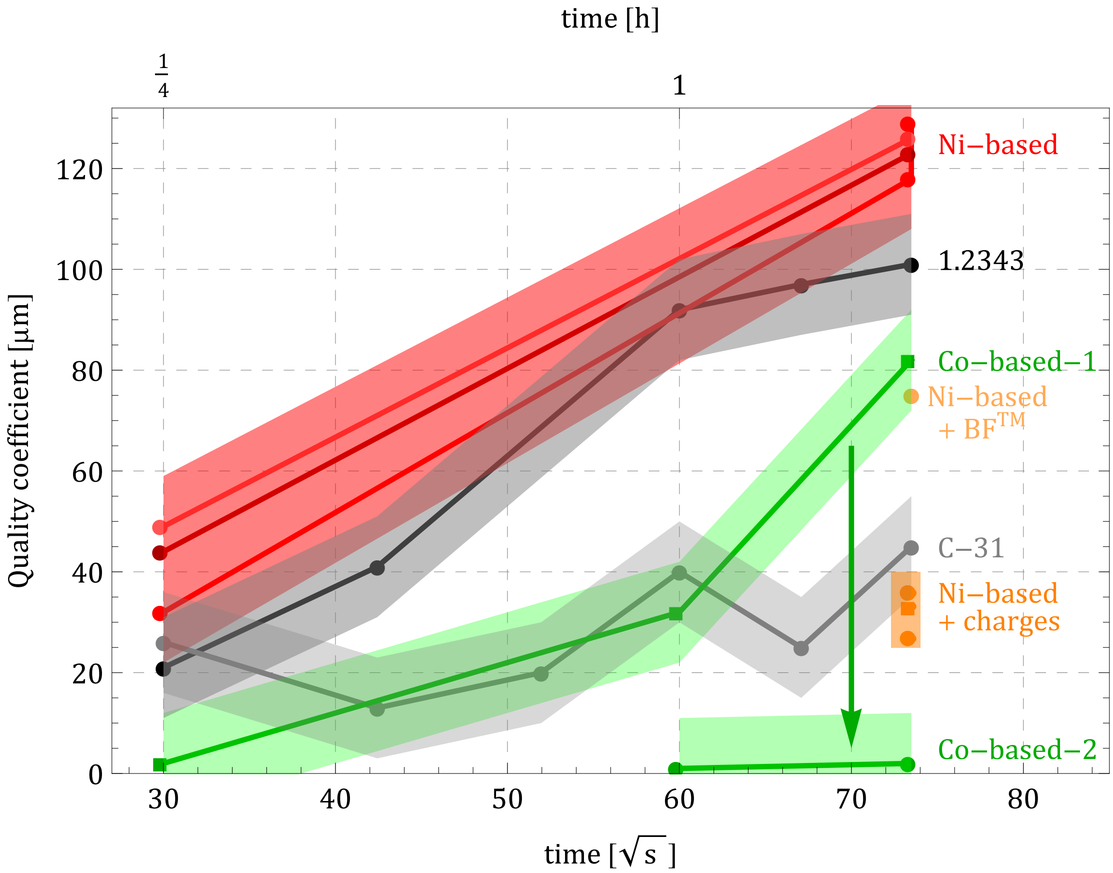

Figure 7.4: Quality coefficient as a function of the square root of time for ferritic steel 1.2343 (black), grey cast-iron C-31 (grey), Ni-based coatings (red), Ni-based coating with charges (orange) and Co-based coatings (green).

For all of these samples, nearly all of the coating disappeared after contact with liquid Al. Thus, the quality coefficient corresponds to the formed compound thickness. The result shows that the measured thickness for such coatings is larger than the one of the steel substrate and thus this type of coating is not a good candidate to protect steel from aluminium corrosion.

The second batch gives more promising results with an important decrease in the quality coefficient. Addition of charges seem to slow down the progression of the intermediate compound, similarly to the graphite in the cast-iron. Nonetheless, deposition is more complicated for such coatings implying inhomogeneities in the coating that are difficult to precisely control , such as the particle size and its distribution in the final coating. The effect of the boron gives a result in between the standard coatings, in red and the charged ones, in orange.

The third batch, with Co-based coatings is the most promising result obtained so far. As already mentioned, the first tested samples, presented in Fig. 7.4 by green squares, were not coated with optimised parameters. However, after observing the good behaviour after 15 min, it was decided to produce new samples with optimised parameters. Two contact times, 60 and 90 min, were tested and results are presented by green circles in Fig. 7.4. These samples present only few pitting and the remaining coating is about 96 % of the surface. This type of coating was chosen to perform in a shot sleeve a test in industrial condition. The coating was deposited on the inner surface of an insert (see section 1.1). This insert was recently placed in a production line of a customer of Castool. At the time the present document is printed, the insert is still operated in the production line.

8 Conclusions

The Fe(s) – Al (l) system investigated at 700 °C leads to the formation of a complex microstructure with intermetallic phases of sizes going from nanometre to hundreds of micrometres. The present work proposed to go through these five orders of magnitude by means of electron microscopy and X-ray tomography investigations. Microstructure and kinetics were investigated and the main points that came out are summarized in section 8.1.1. The focus made on the main phase Fe_2Al_5, with the modelling of its growth and its particular tongue-like structure. The latter is interpreted as a destabilisation of its interface with iron. It is explained by the low diffusion of aluminium in iron, which controls the growth rate at the beginning of the reaction. In addition, a technological solution for reducing the shot sleeve wear is summarized in section 8.1.2. Finally, section 8.2 presents different ways to go further in the understanding of the system.

8.1 Synthesis

8.1.1 Fundametal investigation

Fig. 8.1 presents schematics of the identified regimes during the growth of the intermetallic layer. N_1 and P_1 correspond to the very beginning of the growth and the colonisation of the iron surface by the layer. The Fe_2Al_5 layer is mainly destabilised at during these regimes. T_2 corresponds to the competition between the thickening and the tip growth. T_3 corresponds to a more regular growth with destabilisation that is less effective than thickening. A supplementary regime should appear after T_3 that would correspond to a stationary planar front growth. It is nonetheless out of the observation time range of the present study. The following sections proposes to summarize one after the other each regime. Information about the microstructure and the phenomena observed in chapter 4 complete the description of the regime.

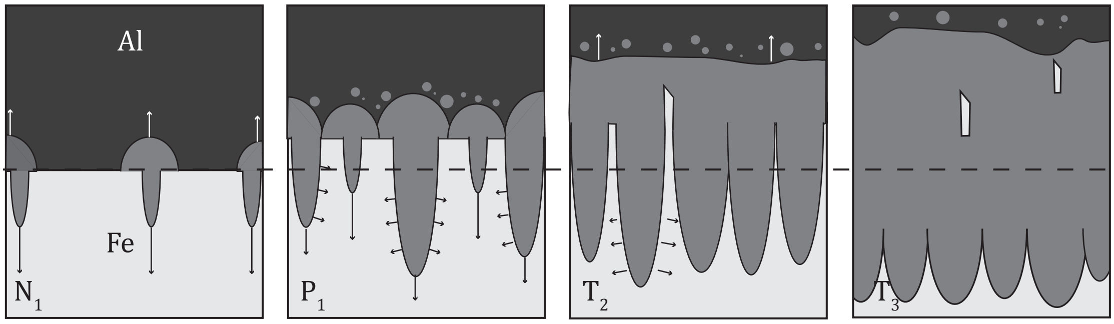

Figure 8.1: Schematics of the main growth regimes of the intermetallic layer: N_1 rapid emergence of the tongues, P_1 tongue colonisation, T_2 thickening and T_3 regular regime.

Beginning of growth (N_1)

After an incubation explained by the presence of an oxide layer on the iron surface and by the native oxide that confines the liquid, the reaction starts with formation of blocks on the liquid side of the interface. Blocks develop in both liquid and solid directions. On the liquid side, the layer grows regularly with time. Its progression at the beginning is slowed down by the effect of the melt saturation. On the solid side, tongues emerge from the blocks and grow rapidly toward the iron matrix with an apparent growth constant of $6.3 \times 10^{-6}\,\mathrm{m \cdot s^{-1/2}}$. It is shown that this particular growth behaviour comes from the destabilisation of the front induced by the low diffusion of aluminium in iron. Aluminium flux in iron controls the growth of the intermetallic layer at the very beginning of the reaction. This is verified by the derivation of Mullins-Sekerka model for the present system. The close observation shows that tip is nearly a single crystal. The apparent random growth of the tongues presents a texture. Tongues grow along one preferential orientation that corresponds to the c-axis of the Fe_2Al_5 crystalline

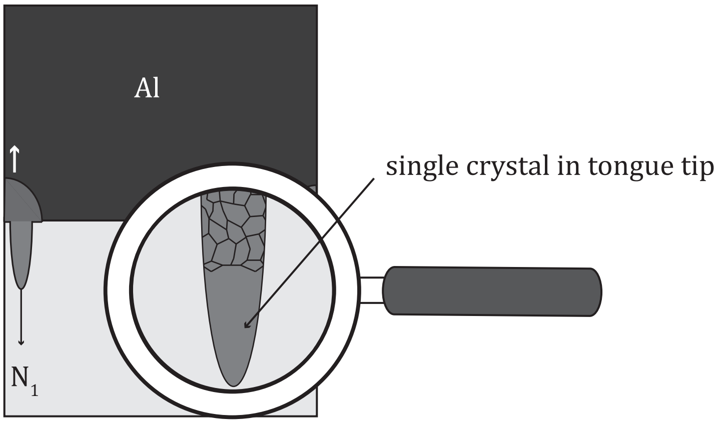

Figure 8.2: N_1, Rapid emergence of the Fe_2Al_5 tongues after an incubation time due to oxide layer. Tongue tips are near from single crystals growing along their c-axis direction.

structure. Tongues are slightly misoriented compared to the main growth direction z that is perpendicular to the initial interface.

Tongue colonisation (P_1)

The reaction continues by the emergence of the tongues at the interface. In parallel tongue tips start to slow down while thickening of their trunk starts. The measured growth constant of the dense layer is 3 times smaller than the one of the tongues with $2.05 \times 10^{-6}\,\mathrm{m \cdot s^{-1/2}}$. The interface between the tongues and the iron matrix was investigated by SEM and TEM methods. It is shown that the internal structure of the tongues is formed by nano–domains with slight and periodic chemical variation, forming nano-squares contrast within the tongue. It is interpreted as a periodic variation between the two limits of the Fe_2Al_5 existence domain. A transition layer of FeAl 100 nm thick between the tongues and the iron matrix is observed. It is shown by FIB reconstruction that this layer surrounds the tongues. The rapid tongue growth at the beginning generates a complex strain field under which iron matrix deforms. Deformation is shown by the strong upward movement of the system in X-ray tomography and is shown by the presence of iron above dashed line in Fig. 8.1. It is also observed by SEM on etched samples that exhibit a recrystallisation of the matrix in the direct tongue surrounding.

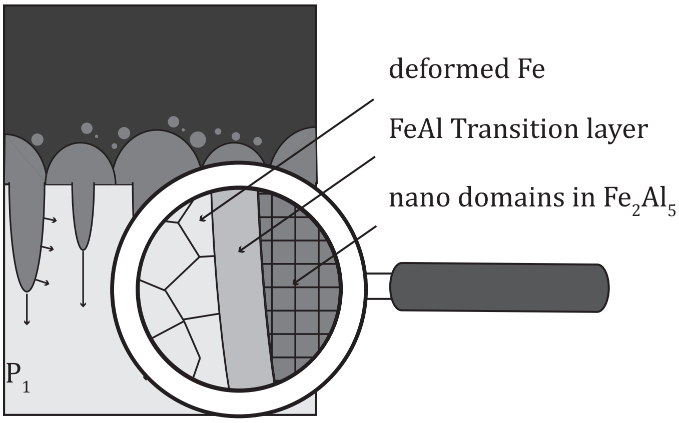

Figure 8.3: P_1, First plateau: Colonisation of the tongues and beginning of the thickening. The tongue-iron interface observation shows the nano squares structure of the tongue, the FeAl layer and the iron matrix deformation with a certain degree of recrystallisation.

Thickening (T_2)

This regime corresponds to the period when the thickening is the most active. A competition between both tongues thickening and tongue tips growth toward the iron occurs, slowing down the latter. This competition leads to an apparent growth constant that varies with time. As the tongue density decreases with the square root of time, the competition is mainly observable at the beginning of this regime. While this competition occurs, on the other side of the layer, growth is more regular. A close observation of the interface with the liquid highlights the presence of a regular Fe_4Al_{13} layer that is about 10 µm thick. It is also observed that blocks detach from the layer and lay in the liquid close to the solid surface. Dissolution mainly occurs when the melt is not yet saturated. The complex nature of the dissolution process is not addressed in the present study. Nonetheless a rapid estimation shows that for the less influenced test, the sample with horizontal interface for *in situ* observation, the dissolved layer represents almost 60 % of the measured layer.

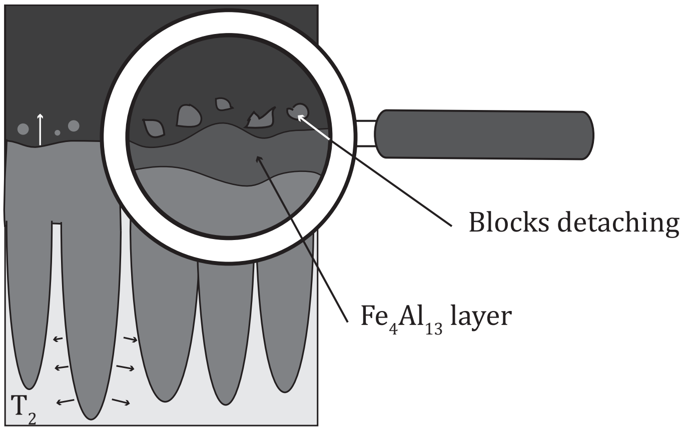

Figure 8.4: T_2, not constant growth rate: The thickening is strongly acting while tongue tips progressively slows down. In the liquid side of the interface, one can observe a regular Fe_4Al_{13} layer that is 10 µm thick and, which dissolved by blocks detaching, in particular when the melt is unsaturated in Fe.

Regular growth (T_3)

Finally, the growth is no more controlled by diffusion in iron but by the one in the intermetallic layer. The tongue tips growth is now less active than the thickening and the layer tends progressively to stabilise. Simulation allows to estimate the achievement of the stationary planar front growth after 52 h if the system doe not reach any limit in the interval, such as full aluminium consumption. It is also shown that the strain field induced by the tongue growth leads to the nucleation of porosity at the interface between the tongues and the iron matrix. They evolve until the surrounding iron is fully consumed and then are trapped at the interface between the tongues. This was seen by EBSD observation revealing the tongue interfaces. One also observes the presence of iron islands that seem to be isolated from the rest of the matrix. This also shows the effect of the strain field on the iron matrix.

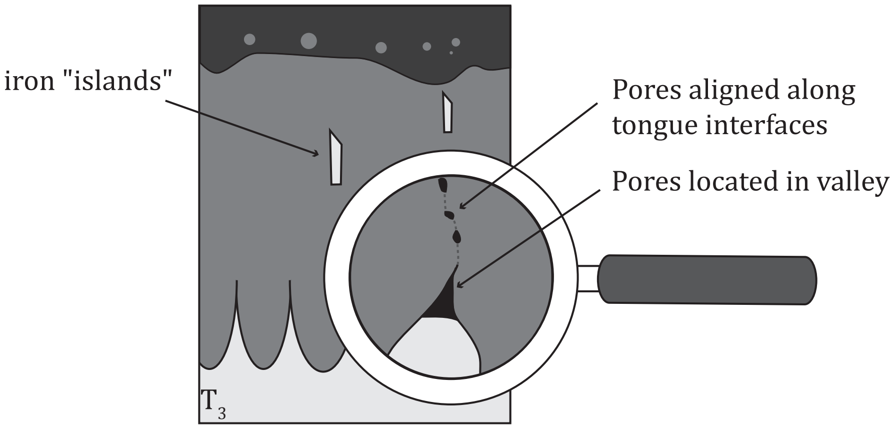

Figure 8.5: Regular growth: Thickening is still operating while general growth is now controlled by diffusion in the intermetallic layer. The latter progressively flattens. Remaining porosity observed in the dense layer is related to the strain field, which appears with tongue growth at the beginning of the reaction.

8.1.2 Technological investigation

The technological investigation was performed as a two-step investigation. The first one consisted in comparing the dipping test results of a ferritic steel and a cast-iron with the one of pure iron. It is shown that species additions lead to a decrease in growth rate and in destabilisation. Furthermore, graphite lamellae in the cast-iron block the progression as they do not allow aluminium to diffuse. Si-addition in the melt lead to a complex ternary Al-rich microstructure that is similar to the one in the binary Al–Fe system but favouring the $FeAl_2$ ternary equivalent phase that destabilises instead of the Fe_2Al_5 . Coating testing shows that Ni-based ones are more reactive than the substrate, that additional charges slow down the compound formation, similarly to the graphite in the cast-iron and that Co-based coating is the most promising tested coating. The latter was chosen for a test on a production line and is currently operating.

8.2 Perspectives

Further development and deeper investigation could be done by improving each of the three main investigation tools, namely sample production, observation techniques and numerical modeling. This would allow to complete the analysis on different aspects listed hereafter.

Sampling at a higher temperature than 700 °C would exhibit a tongue – iron interface with a different shape. In this way, a complementary investigation by X-ray tomography at different temperatures would give information on the tongue-like structure with temperature, confirming or not that the layer tends to flatten above 800 °C. Samples with pre-saturated bath are also of interest, as it would allow to limit dissolution and thus to precisely determine growth rate constants in this regime.

Numerical simulation would also be very helpful concerning the complementary understanding of the destabilisation. This implies a deep rewriting of the code in order to take into account the saturation at the beginning of the reaction and the addition of other intermetallic phases. Furthermore, to fully study the destabilisation, a more complex calculation, in two or three dimensions would be of interest. For that, phase field modeling is a very promising tool, that would allow to describe the interface evolution considering the transitory diffusive regime of the reaction instead of the stationary one used in the present study.

Interesting observation could be performed with a FIB – EBSD mapping of the tongues. This would give the grain orientation in three dimensions and the final proof that pores are out of Fe_2Al_5 phase, at the interface between tongues. In the same way, an optimisation of the X-ray EDS chemical measurements using standards would also confirm the only presence of Fe_2Al_5 in the tongues at the nanometric scale.

Bibliography

[1] I.N. Fridlyander, V.G. Sister, O.E. Grushko, V.V. Berstenev, L.M. Sheveleva, and L.A. Ivanova. Aluminum alloys: A promising material in automotive industry. *Metallovedenie i Termicheskaya Obrabotka Metallov*, 44(9-10):365–370, 2002.

[2] D.A. Porter and K.E. Easterling. *Phase transformations in metals and alloys, 2nd edition*. Taylor & Francis Group, London, Chapman and Hall edition, 1981.

[3] C.J. Smithells. *Metals Reference Book*. Elsevier Science Ltd, Exeter, United Kingdom, 1976.

[4] L.G. Harrison. Influence of dislocations on diffusion kinetics in solids with particular reference to the alkali halides. *Transactions of the Faraday Society*, 57:1191–1199, 1961.

[5] M. Eggersmann and H. Mehrer. Diffusion in intermetallic phases of the fe-al system. *Philosophical Magazine A: Physics of Condensed Matter, Structure, Defects and Mechanical Properties*, 80(5):1219–1244, 2000.

[6] H. Amara, C.C. Fu, F. Soisson, and P. Maugis. Aluminum and vacancies in alpha-iron: Dissolution, diffusion, and clustering. *Physical Review B - Condensed Matter and Materials Physics*, 81(17), 2010.

[7] W Jost. *Diffusion in solids, liquids, gases*. Academic Press, 3rd edition, 1960.

[8] C. Wagner. The evaluation of data obtained with diffusion couples of binary single-phase and multiphase systems. *Acta Metallurgica*, 17(2):99–107, 1969.

[9] P. Maugis. *Formation de composes intermetalliques Ti-Al en couches minces par interdiffusion reactive*. PhD thesis, Universite de Paris-sud, Centre d'Orsay, March 1994.

[10] V.N. Yeremenko, Ya.V. Natanzon, and V.I. Dybkov. The effect of dissolution on the growth of the Fe_2Al_5 interlayer in the solid iron – liquid aluminium system. *Journal of Materials Science*, 16(7):1748–1756, 1981.

[11] Y. Tanaka and M. Kajihara. Kinetics of isothermal reactive diffusion between solid Fe and liquid Al. *Journal of Materials Science*, pages 1–9, 2010.

[12] M. Kajihara. Analysis of kinetics of reactive diffusion in a hypothetical binary system. *Acta Materialia*, 52(5):1193 – 1200, 2004.

[13] J. Svoboda, E. Gamsjäger, F.D. Fischer, and E. Kozeschnik. Modeling of kinetics of diffusive phase transformation in binary systems with multiple stoichiometric phases. *Journal of Phase Equilibria and Diffusion*, 27(6):622–628, 2006.

[14] J. Svoboda, F.D. Fischer, and R. Abart. Modeling of diffusional phase transformation in multi-component systems with stoichiometric phases. *Acta Materialia*, 58(8):2905–2911, 2010.

[15] L. Onsager. Theories and problems of liquid diffusion. *Ann. N.Y. Acad. Sci.*, 46:241–265, 1945.

[16] L. Deillon. *Soudure par interdiffusion dans les systèmes Au-In et In-Ni : Application à des composants microélectroniques.* PhD thesis, Ecole Polytechnique Fédérale de Lausanne, 2012.

[17] D.W. Fan and B.C. De Cooman. Formation of an aluminide coating on hot stamped steel. *ISIJ International*, 50(11):1713–1718, 2010. cited By (since 1996)3.

[18] S. Gedevanishvili and S.C. Deevi. Processing of iron aluminides by pressureless sintering through fe + al elemental route. *Materials Science and Engineering A*, 325(1-2):163–176, 2002. cited By (since 1996)51.

[19] H.-Z. Kang, S. Lee, and C.-T. Hu. The role of pre-formed fe2al5 in p/m processing of fe3al. *Materials Science and Engineering A*, 398(1-2):360–366, 2005. cited By (since 1996)4.

[20] P.G. Saffman. Exact solutions for the growth of fingers from a flat interface between two fluids in a porous medium or hele-shaw cell. *Quarterly Journal of Mechanics and Applied Mathematics*, 12(2):146–150, 1959.

[21] R. Maes. *Etude experimentale de la digitation visqueuse de fluides miscibles en cellule de Hele-Shaw.* PhD thesis, Université libre de Bruxelles, 2009.

[22] J.A. Dantzig and M. Rappaz. *Solidification.* Presses polytechniques et universitaires romandes, 2009.

[23] T.B. Massalski and U.R. Kattner. *Binary alloy phase diagrams.* ASM International, Materials Park, OH, 1990.

[24] Y. Du, J.C. Schuster, Z.-K. Liu, R. Hu, P. Nash, W. Sun, W. Zhang, J. Wang, L. Zhang, C. Tang, Z. Zhu, S. Liu, Y. Ouyang, W. Zhang, and N. Krendelsberger. A thermodynamic description of the Al-Fe-Si system over the whole composition and temperature ranges via a hybrid approach of CALPHAD and key experiments. *Intermetallics*, 16(4):554–570, 2008.

[25] C. Guo, Z. Du, C. Li, B. Zhang, and M. Tao. Thermodynamic description of the Al-Fe-Zr system. *Calphad: Computer Coupling of Phase Diagrams and Thermochemistry*, 32(4):637–649, 2008.

[26] V. Raghavan. Al-Fe-Ni (Aluminum-Iron-Nickel). *Journal of Phase Equilibria and Diffusion*, 30(4):375–377, 2009.

[27] L. Zhang, J. Wang, Y. Du, R. Hu, P. Nash, X.-G. Lu, and C. Jiang. Thermodynamic properties of the Al-Fe-Ni system acquired via a hybrid approach combining calorimetry, first-principles and CALPHAD. *Acta Materialia*, 57(18):5324–5341, 2009.

[28] Z.-K. Liu. First-principles calculations and CALPHAD modeling of thermodynamics. *Journal of Phase Equilibria and Diffusion*, 30(5):517–534, 2009.

[29] M. Seierstein. *COST507 Thermochemical Database for Light Metal Alloys.* I Ansara, A.T. Dinsdale, M.H. Rand (Eds.), 1994.

[30] H.E. Swanson and E. Tatge. Standard x-ray diffraction powder patterns. *National Bureau of Standards (U.S.)*, 539:p1–p75, 1955.

[31] A.N. Bashkatov, F.A. Sidorenko, L.P. Zelenin, T.N. Gal'perina, P.V. Gel'd, and T.D. Zotov. Magnetic properties of the beta-phase of the iron- aluminium system. *Physics of Metals and Metallography*, 32:118–123, 1971.

[32] A. S. Cooper. Precise lattice constants of germanium, aluminum, gallium arsenide, uranium, sulphur, quartz and sapphire. *Acta Crystallographica*, 15(6):578–582, Jun 1962.

[33] U. Burkhardt, Yu. Grin, M. Ellner, and K. Peters. Structure refinement of the iron–aluminium phase with the approximate composition Fe_2Al_5. *Acta Crystallographica Section B*, 50(3):313–316, 1994.

[34] U. Burkhardt, Yu. Grin, M. Ellner, and K. Peters. Refinement of the Fe_4Al_{13} structure and its relationship to the quasihomological homeotypical structures. *Zeitschrift für Kristallographie*, 209, 479-487 1993.

[35] R. N. Corby and P. J. Black. The structure of $FeAl_2$ by anomalous dispersion methods. *Acta Crystallographica Section B*, 29(12):2669–2677, Dec 1973.

[36] J. Hirvonen and J. Räisänen. Diffusion of aluminum in ion-implanted alpha iron. *Journal of Applied Physics*, 53(4):3314–3316, 1982.

[37] A. Heesemann, E. Schmidtke, F. Faupel, A. Kolb-Telieps, and J. Klöwer. Aluminum and silicon diffusion in fe-cr-al alloys. *Scripta Materialia*, 40(5):517–522, 1999.

[38] S. Kobayashi and T. Yakou. Control of intermetallic compound layers at interface between steel and aluminum by diffusion-treatment. *Materials Science and Engineering A*, 338(1-2):44–53, 2002.

[39] S. Shankar and D. Apelian. Die soldering: Mechanism of the interface reaction between molten aluminum alloy and tool steel. *Metallurgical and Materials Transactions B: Process Metallurgy and Materials Processing Science*, 33(3):465–476, 2002.

[40] M. Kajihara. Quantitative evaluation of interdiffusion in Fe_2Al_5 during reactive diffusion in the binary Fe-Al system. *Materials Transactions*, 47(6):1480–1484, 2006.

[41] D. Naoi and M. Kajihara. Growth behaviour of $\mathrm{Fe_2Al_5}$ during reactive diffusion between Fe and Al at solid-state temperatures. *Materials Science and Engineering: A*, 459(1-2):375 – 382, 2007.

[42] T. Sasaki and Yakou T. Effects of heat treatment conditions on formation of fe-al alloy layer during high temperature aluminizing. *ISIJ International*, 47(7):1016–1022, 2007.

[43] W.-J. Cheng, Y.-Y. Chang, and C.-J. Wang. Observation of high-temperature phase transformation in the aluminide cr-mo steel using ebsd. *Surface and Coatings Technology*, 203(5-7):401 – 406, 2008.

[44] Y. Tanaka and M. Kajihara. Morphology of compounds formed by isothermal reactive diffusion between solid Fe and liquid Al. *Materials Transactions*, 50(9):2212–2220, 2009.

[45] W.-J. Cheng and C.-J. Wang. Growth of intermetallic layer in the aluminide mild steel during hot-dipping. *Surface and Coatings Technology*, 204(6-7):824–828, 2009.

[46] R. Torres, V.H. López, J.P. Arredondo, R. García, J.A. Verduzco, and M.L. Mondragón. The effect of temperature and time on the formation of a reaction interlayer during aluminizing of a carbon steel. *Materials Research Society Symposium Proceedings*, 1242:125–130, 2010.

[47] Wang C.-J. Cheng, W.-J. Study of microstructure and phase evolution of hot-dipped aluminide mild steel during high-temperature diffusion using electron backscatter diffraction. *Applied Surface Science*, 257(10):4663–4668, 2011.

[48] H. Springer, A. Kostka, E.J. Payton, D. Raabe, A. Kaysser-Pyzalla, and G. Eggeler. On the formation and growth of intermetallic phases during interdiffusion between low-carbon steel and aluminum alloys. *Acta Materialia*, 59(4):1586–1600, 2011.

[49] T. Heumann and S. Dittrich. Structure character of the fe<inf>2</inf>al<inf>5</inf> intermetallics compound in hot dip aluminizing process. *Z. Metallkd.*, 50(10), 1959.

[50] S.G. Denner and R.D. Jones. Kinetic interactions between aluminium//l//i//q//u//i//d and iron/steel//s//o//l//i//d for conditions applicable to hot-dip aluminizing. *Met Technol*, 4(pt 3):167–174, 1977.

[51] S.C. Kwon and J.Y. Lee. Interface morphology between the aluminide layer and iron substrate in the hot-dip aluminizing process. *Canadian Metallurgical Quarterly*, 20(3):351–357, 1981.

[52] G. Eggeler, W. Auer, and Kaesche H. On the influence of silicon on the growth of the alloy layer during hot dip aluminizing. *Journal of Materials Science*, 21(9):3348–3350, 1986.

[53] M. Sundqvist and S. Hogmark. Effects of liquid aluminium on hot-work tool steel. *Tribology International*, 26(2):129 – 134, 1993.

[54] F. Barbier, D. Manuelli, and K. Bouché. Characterization of aluminide coatings formed on 1.4914 and 316l steels by hot-dipping in molten aluminium. *Scripta Materialia*, 36(4):425–431, 1997.

[55] K. Bouché, F. Barbier, and A. Coulet. Phase formation during dissolution of nickel in liquid aluminium. *Zeitschrift für Metallkunde/Materials Research and Advanced Technique*, 88(6):446–451, 1997.

[56] K. Bouché, F. Barbier, and A. Coulet. Intermetallic compound layer growth between solid iron and molten aluminium. *Materials Science and Engineering A*, 249(1-2):167–175, 1998.

[57] H.R. Shahverdi, M.R. Ghomashchi, S. Shabestari, and J. Hejazi. Microstructural analysis of interfacial reaction between molten aluminium and solid iron. *Journal of Materials Processing Technology*, 124(3):345–352, 2002.

[58] A. Bouayad, Ch. Gerometta, Belkebir A., and A. Ambari. Kinetic interactions between solid iron and molten aluminium. *Materials Science and Engineering A*, 363(1-2):53 – 61, 2003.

[59] Q. Han and S. Viswanathan. Analysis of the mechanism of die soldering in aluminum die casting. *Metallurgical and Materials Transactions A: Physical Metallurgy and Materials Science*, 34(1):139–146, 2003.

[60] D. Balloy and J.-C. Tissier. Corrosion de matériaux industriels par l'aluminium liquide. In *Matériaux 2006, Dijon (conference)*, 2006.

[61] D. Balloy, J.-C. Tissier, M.-L. Giorgi, and M. Briant. Corrosion mechanisms of steel and cast iron by molten aluminum. *Metallurgical and Materials Transactions A: Physical Metallurgy and Materials Science*, pages 1–11, 2010.

[62] P.R. Calvillo, L. Suarez, and Y. Houbaert. Al-Si-Fe intermetallics on Fe-substrates during hot-dipping. *Defect and Diffusion Forum*, 297-301:1042–1047, 2010.

[63] I. Danzo, K. Verbeken, and Y. Houbaert. Characterization of the intermetallic compounds formed during hot dipping of electrical steel in a hypo-eutectic AlSi bath. *Defect and Diffusion Forum*, 297-301:370–375, 2010.

[64] A. Hibino. Estimation of kinetic parameters for combustion synthesis of feal intermetallic compound by dipping experiment of fe wire into al melt. *Materials Transactions*, 51(3):516–524, 2010.

[65] M.-B. Lin and Wang C.-J. Microstructure and high temperature oxidation behavior of hot-dip aluminized coating on high silicon ductile iron. *Surface and Coatings Technology*, 2010. cited By (since 1996) 0; Article in Press.

[66] N. Zhang, J. Wosik, W. Fragner, R. Sonnleitner, and G. E. Nauer. Three-dimensional analysis of the growth of intermetallics phases between solid steel and molten aluminium. *Intermetallics*, 18(2):221 – 225, 2010.

[67] S. Jiang and L. Shichun. Microstructure evolution of Al/Fe liquid/solid interface. *Applied Mechanics and Materials*, 268(PART 1):417–421, 2013.

[68] G. Eggeler, Th. Theuerkauf, and W. Auer. Studies of pack aluminizing of low-alloy steel (13 crmo 44). Untersuchung zum pulveraluminieren von niedriglegiertem stshl (13 CrMo 44). *Zeitschrift für Werkstofftechnik/Materials Technology and Testing*, 16(10):359–365, 1985.

[69] J. Lapin, D. Tiberghien, and F. Delannay. On the parameters affecting the formation of iron aluminides during pressure-assisted infiltration of aluminum into a preform of steel fibres. *Intermetallics*, 8(12):1429–1438, 2000.

[70] S. Hirose, T. Itoh, M. Makita, S. Fujii, S. Arai, K. Sasaki, and H. Saka. Defect structure of deformed Fe_2Al_5 intermetallic compound. *Intermetallics*, 11(7):633–642, 2003.

[71] W. Deqing, S. Ziyuan, and Z. Longjiang. A liquid aluminum corrosion resistance surface on steel substrate. *Applied Surface Science*, 214(1-4):304–311, 2003.

[72] F. Kargl, H. Weis, T. Unruh, and A. Meyer. Self diffusion in liquid aluminium. *Journal of Physics: Conference Series*, 340, 2012.

[73] M. Gemmaz, M. Afyouni, and A. Mosser. Determination of the diffusion coefficient of al in an fe-al alloy by auger spectrometry. *Surface Science*, 227(1-2):L109–L111, 1990.

[74] D. Bergner and Y. Khaddour. Impurity and chemical diffusion of al in bcc and fcc iron. *Defect and Diffusion Forum*, 95-98:709–714, 1993.

[75] F.S. Buffington, K. Hirano, and M. Cohen. Self diffusion in iron. *Acta Metallurgica*, 9(5):434 – 439, 1961.

[76] M. Yu, R. Shivpuri, and R.A. Rapp. Effects of molten aluminum on H13 dies and coatings. *Journal of Materials Engineering and Performance*, 4(2):175–181, 1995.

[77] M.-L. Giorgi, J.-B. Guillot, and R. Nicolle. Theoretical model of the interfacial reactions between solid iron and liquid zinc-aluminium alloy. *Journal of Materials Science*, 40(9-10):2263–2268, 2005.

[78] Schlesinger M. *Modern electroplating.* 2010.

[79] M.D. Abramoff, P.J. Magalhaes, and S.J. Ram. Image processing with imageJ. *Biophoton Int*, 11:36–41, 2004.

[80] J. Goldstein, D.E. Newbury, D.C. Joy, C.E. Lyman, P. Echlin, E. Lifshin, L. Sawyer, and J.R. Michael. *Scanning Electron Microscopy and X-ray Microanalysis.* Springer, third ed. edition, 2003.

[81] B.D. Williams and C.B. Carter. *Transmission Electron Microscopy*. Springer, second edition, 1996.

[82] Kak, A.C. and Slaney, M. *Principles of computerized tomographic imaging*. IEEE Press, 1987.

[83] M. Di Michiel, J.M Merino, D. Fernandez-Carreiras, T. Buslaps, V. Honkimäki, P. Falus, T. Martins, and O. Svensson. Fast microtomography using high energy synchrotron radiation. *Sci. Instrum.*, 76, 2005.

[84] G. Pasche, M. Scheel, R. Schäublin, C. Hébert, M. Rappaz, and A. Hessler-Wyser. Time-resolved x-ray microtomography observation of intermetallic formation between solid fe and liquid al. *Metallurgical and Materials Transactions A: Physical Metallurgy and Materials Science*, 44(9):4119–4123, 2013.

[85] C. Sommer, C. Staehler, U. Köhte, and Hamprecht F.A. "ilastik: Interactive Learning and Segmentation Toolkit". In *8th IEEE International Symposium on Biomedical Imaging (ISBI 2011)*, 2011.

[86] J. Lapin. Microstructure and mechanical properties of iron aluminides processed by reactive squeeze infiltration. *Materials Letters*, 58(24):3007–3011, 2004.

[87] D Favez. *Soudage laser or-acier: métallurgie et procédé*. PhD thesis, Ecole Polytechnique Fédérale de Lausanne, 2009.

[88] M. Rettenmayr, O. Warkentin, M. Rappaz, and H. E. Exner. Simulation of solutal remelting. *Acta Materialia*, 49(13):2499 – 2510, 2001.

[89] M. Perez. Gibbs-Thomson effects in phase transformations. *Scripta Materialia*, 52(8):709–712, 2005.

[90] R. Trivedi and K. Somboonsuk. Pattern formation during the directional solidification of binary systems. *Acta Metallurgica*, 33(6):1061–1068, 1985. cited By (since 1996)58.

[91] W. Kajoch and A. Fajkiel. Testing the soldering tendencies of aluminium die casting alloys. *Transactions of the 16th International Die Casting Congress and Exposition, Detroit*, 1991.

Table of symbols

Symbol	Name	Unit
Roman letters		
a	Atomic activity	$-$
A	Species name, generally forming α phase	$-$
A_z	Intermetallics area fraction at position z	m^2
a, b, c	Crystallographic cell parameters	m
B	Species name, generally forming β phase	$-$
c	Volume concentration	$mol \cdot m^{-3}$
$\bar{c}$	Mean atomic concentration (in liquid)	$mol \cdot m^{-3}$
$\tilde{c}$	Concentration at the destabilised interface	$mol \cdot m^{-3}$
c_η	Concentration in Fe_2Al_5 pahse	$-$
c_l^*	Concentration at dendrite tip	$mol \cdot m^{-3}$
c_o	Concentration at the interface between α and η on iron side	$-$
c_s	Saturation concentration	$mol \cdot m^{-3}$
D	Diffusion coefficient	$m^2 \cdot s^{-1}$
D_0	Pre exponential factor for diffusion	$m^2 \cdot s^{-1}$
D_A^ν	Diffusion coeffi of species A in phase ν	$m^2 \cdot s^{-1}$
D^*	Tracer diffusion coefficient	$m^2 \cdot s^{-1}$
G	Free energy	$J \cdot mol^{-1}$
g	Gravity	ms^{-2}
H	Molar enthalpy	$J \cdot mol^{-1}$
h	Melt height	m
J	Atomic flux	$mol \cdot m^{-2} \cdot s^{-1}$
J_α	Flux in iron at the η interface	$mol \cdot m^{-2} \cdot s^{-1}$
J_η	Flux in the η phase at the iron interface	$mol \cdot m^{-2} \cdot s^{-1}$
k	Dissolution rate	$m \cdot s^{-1}$
k	Partition coefficient (ratio between c_0 and c_l^*)	$-$
k	node index of the Fe - η interface(modelling)	$-$
K	Growth constant coefficient	$m \cdot s^{-1/2}$

Symbols

Symbol	Name	Unit
K_0	Pre exponential factor for growth constant	$m \cdot s^{-1/2}$
l	node index of the η phase - Al interface (modelling)	–
L	Optimised interaction parameter	$J \cdot mol^{-1}$
L	Sample length (dipping test)	m
L_m	Melt length from the sample interface	m
m	Slope of the equilibrium line in the phase diagram	K
$\mathscr{M}$	Molar mass	$kg \cdot mol^{-1}$
M_B	Atomic mobility	$mol \cdot s \cdot kg^{-1}$
n	mole	–
N	number of atoms	–
N_1	First regime of the tongues growth	–
N_a	Avogadro number	mol^{-1}
P_1	First plateau observed in the tongue thickening	–
P_2	Second plateau observed in tongue thickening	–
Q	Activation energy	$J \cdot mol^{-1}$
QC	Quality coefficient	m
R	Gas constant	$J \cdot K^{-1} \cdot mol^{-1}$
R	Mean atomic movement	m
r_1	Sample radius	m
r_2	Melt raidus (vertical configuration)	m
r_i	atomic position of atom i	m
S	unitary surface	–
S	Exchange surface between iron and aluminium	m^2
t	time	s
T	Temperature	$°C$
T_1	First growth regime	–
T_2	Second growth regime	–
T_3	Third growth regime	–
u	velocity	$m \cdot s^{-1}$
v	velocity	$m \cdot s^{-1}$
V	Melt volume	m^3
V_ζ	Volume of the domain ζ	m^3
V_m	Molar volume	$m^3 \cdot mol^{-1}$
W	Intermetallic equivalent thickness	W
X	Atomic fraction	–
x_i^*	Position of the interface i (modelling)	m
x, y, z	Cartesian coordinates	m
x^*	cartesian position of destabilized interface	m
Greek Letters		
α	Primary phase, generally iron	–
α_2	FeAl phase, BCC ordered	–
β	Primary phase	–
ΔH_{mix}	Mixing enthalpy	$J \cdot mol^{-1}$

Symbol	Name	Unit
δ_v	Boundary layer in dipping test	m
$\dot{\epsilon}$	Amplitude velocity of the destabilisation	$m \cdot s^{-1}$
ϵ	Destabilisation amplitude	m
η	Intermetallic compound Fe_2Al_5	–
Γ	Gibbs-Thomson coefficient	$K \cdot m$
γ	Activity coefficient	–
$\gamma_{\alpha\eta}$	Interfacial energy beween α and γ	Jm^{-2}
κ	Interface curvature	m^{-1}
λ	Destabilization wavelength	m
μ	Chemical potential	$J \cdot mol^{-1}$
ν	Phase index	–
ν	Kinematic viscosity	$m^2 \cdot s^{-1}$
Ω	Molar entropic parameter	$J \cdot mol^{-1}$
ω	Destabilisation pulsation	m^{-1}
Φ	cristallographic structure index	–
ρ	Density	$kg \cdot m^3$
Θ	Logarithmic ratio of the dynamic viscosities	–
θ	Intermetallic compound Fe_4Al_{13}	–
$\tilde{c}$	Concentration of the destabilized interface	–
$\tilde{D}$	Interdiffusion coefficient	$m^2 \cdot s^{-1}$
ξ	dynamic viscosity	$m^2 \cdot s^{-1}$
ζ	Intermetallic compound $FeAl_2$	–
ζ	domain index in the intermetallics	–
Dimensionless Numbers		
Fo	Fourier number	–
Pe	Peclet number	–
Sc	Schmidt number	–

Calphad coefficients

Free energy as a function of the temperature for pure elements are given by Equ.1 and depends on the crystallographic structure.

$$G_i^{\Phi} = a + bT + cT\ln T + dT^2 + eT^3 + fT^{-1} + gT^7 + hT^{-9} \tag{1}$$

Table 1: Determined coefficients for free energy calculation of pure aluminium phases

Range[K]	a	b	c	d	e	f	g
Free energy $G_{\mathrm{Al}}^{\mathrm{fcc}}$ of pure Al^{fcc}							
298-700	-7976.15	137.09	-24.36	-1.88×10^{-3}	-8.77×10^{-7}	74092	
700-933	-11276.24	223.04	-38.85	18.53×10^{-3}	-5.76×10^{-7}	74092	
933-2900	- 11278.37	188.68	-31.74				h=12.3×10^{27}
Free energy $G_{\mathrm{Al}}^{\mathrm{bcc}}$ of pure Al^{bcc}							
298-700	2106.85	132.28	-24.36	-1.88×10^{-3}	-8.77×10^{-7}	74092	
700-933	-1193.24	218.23	-38.85	18.53×10^{-3}	-5.76×10^{-7}	74092	
933-2900	- 1195.38	183.87	-31.74			h=12.3×10^{27}	
Free energy $G_{\mathrm{Al}}^{\mathrm{liq}}$ of pure liquid Al^{liq}							
$G_{\mathrm{Al}}^{\mathrm{fcc}}$ +							
298-933	11005.29	-11.84					7.93×10^{-20}
933-2900	10482.38	-11.25					1.23×10^{28}

Table 2: Determined coefficients for free energy calculation of pure iron phases and FeAl.

Magnetic contribution $G_{\mathrm{Fe}}^{\mathrm{mag}}$ of pure Fe							
$G_{\mathrm{Fe}}^{\mathrm{mag}}$	A= 1.558	B= 2.22	p=0.4	T$_{\mathrm{curie}}$= 1043 K			
Range[K]	a	b	c	d	e	f	g
Free energy $G_{\mathrm{Fe}}^{\mathrm{bcc}}$ in pure Fe^{bcc}							
$G_{\mathrm{Fe}}^{\mathrm{mag}}$+							
298-1811	1225.7	124.13	-23.51	-4.39×10^{-3}	-5.89×10^{-8}	77359	
Free energy $G_{\mathrm{Fe}}^{\mathrm{liq}}$ of pure liquid Fe^{liq}							
$G_{\mathrm{Fe}}^{\mathrm{bcc}}$+							
298-1811	12040.17	-6.55					-3.67×10^{-21}
Free energy G_{FeAl} of FeAl							
$\frac{1}{2}G_{\mathrm{Al}}^{\mathrm{bcc}} + \frac{1}{2}G_{\mathrm{Fe}}^{\mathrm{bcc}}$+							
	-37890.5	7.99					

Guillaume **Pasche**

- *PhD in material science at EPFL*
- *Academic & industrial background*
- *Scanning Electron Microscopy specialist*

Education

Current ***PhD in Material Science***, *EPFL*

2007 ***Master in Material Science and Engineering***, *EPFL*

2001 ***Swiss federal maturity***, *Gymnase Auguste-Piccard, Lausanne*

Experience

2009 **Scientific Assistant**, *EPFL*, in partnership with Flexcell S.A.

Development of a routine method for roughness measurement of flexible solar cells by Scanning Electron Microscopy (SEM). This method allows to improve the quality control of the solar cells during production

2008 **Project Manager**, *Rolex S.A.*

Installation of a new casting furnace for precious metals. Development of a numerical model based on heat flux and then used to design moulds limiting shrinkage. The furnace is now in the production line

2006 **Placement**, *PX Holding*, 2 months

Completing properties database of products through mechanical testing

Miscellaneous

2005 **Ski Instructor with Swiss Federal Patent**

Member of the Swiss Ski School of Château d'Oex since 2006

Technical Skills

Computer	Adobe Illustrator, C++, Fiji-ImageJ, LaTeX, Mathematica, Microsoft Windows, OSX
SEM	Energy-Dispersive X-ray spectroscopy (EDX), Electron Back Scattered Diffraction (EBSD)
Laboratory	Image treatment, material characterization, mechanical testing, solidification, sample preparation

Rue des Fontaines 14 – 1352 Agiez, Switzerland
📱 *+41 79 675 73 24* • ☎ *+41 24 565 51 79*
✉ *pasche.guillaume@gmail.com*

Academic Projects

PhD Thesis (*CIME, EPFL*)

Title	***Interaction between liquid aluminium and solid iron, Al-rich intermetallics formation***
Supervision	One master thesis and five semester projects, practicals on SEM and image treatment
Presentations	**EMRS** Strasbourg/F, **SSOM** Les Diablerets/CH, **Titech-EPFL** workshop Hakone/JP, **EMC** Manchester/UK (presented by A. Hessler-Wyser), **NADCA** Minneapolis/USA (presented by P. Robins, Castool), **Euromat** Montpellier/F
Posters	**EMC** Manchester/UK, **MES** Darmstadt/D, **EDMX**, Lausanne/CH, **MES** Darmstadt/D
Publications	
2013	*Time-resolved X-Ray microtomography observation of intermetallics formation between solid Fe and liquid Al*, Metallurgical and Materials Transaction, Sep. 2013, vol. 44, pp 4119 – 4123
2012	*Degradation mechanisms of high pressure aluminium die casting tools: a testing facility*, proceeding for the NADCA Congress, Minneapolis/USA

Master Thesis (*LSMX, EPFL*)

Title	***Ingot solidification of a model Pb-Ag alloy***
Description	Development of an experimental set up and an inverse method code to determine the heat transfer coefficients of different surfaces and design of moulds with optimized heat flux, allowing optimized solidification

Languages

French	Mother tongue
English	Good speaking and writing skills
German	Intermediate speaking and writing skills

Activities

Ski	Swiss Academic Champion Downhill (2002), 3rd place at Junior Swiss Super G Championship (1997)
Association	Committee member of the Material Student Association, EPFL (2005–2007), Alpine head of the Swiss Academic Ski Club (2002–2005)

Complementary Informations

Birth	July 8th, 1982
Nationality	Swiss
Details	in a relationship, One child